REAL-TIME ESTIMATION OF GAS CONCENTRATION RELEASED FROM A MOVING SOURCE USING AN UNMANNED AERIAL VEHICLE

by

Tatiana Egorova

A Dissertation

Submitted to the Faculty of

WORCESTER POLYTECHNIC INSTITUTE

in partial fulfillment of the requirements for the degree of
Doctor of Philosophy
in
Aerospace Engineering

August 2015

APPROVED:

Dr. Nikolaos A. Gatsonis, Co-Advisor
Professor, Aerospace Engineering Program

Dr. Michael A. Demetriou, Co-Advisor
Professor, Aerospace Engineering Program

Dr. John Burns, Committee Member
Professor, Department of Mathematics, VPI

Dr. Raghvendra V. Cowlagi, Graduate Committee Representative
Assistant Professor, Aerospace Engineering Program

Abstract

This work presents an approach which provides the real-time estimation of the gas concentration in a plume using an unmanned aerial vehicle (UAV) equipped with concentration sensors. The plume is assumed to be generated by a moving aerial or ground source with unknown strength and location, and is modeled by the unsteady advection-diffusion equation with ambient winds and eddy diffusivities. The UAV dynamics is described using the point-mass model of a fixed-wing aircraft resulting in a sixth-order nonlinear dynamical system. The state (gas concentration) estimator takes the form of a Luenberger observer based on the advection-diffusion equation. The UAV in the approach is guided towards the region with the larger state-estimation error via an appropriate choice of a Lyapunov function thus coupling the UAV guidance with the performance of the gas concentration estimator. This coupled controls-CFD guidance scheme provides the desired Cartesian velocities for the UAV and based on these velocities a lower-level controller processes the control signals that are transmitted to the UAV. The finite-volume discretization of the estimator incorporates a second-order total variation diminishing (TVD) scheme for the advection term. For computational efficiency needed in real-time applications, a dynamic grid adaptation for the estimator with local grid-refinement centered at the UAV location is proposed. The approach is tested numerically for several source trajectories using existing specifications for the UAV considered. The estimated plumes are compared with simulated concentration data. The estimator performance is analyzed by the behavior of the RMS error of the concentration and the distance between the sensor and the source.

Acknowledgments

I would like to express my special appreciation and thanks to my advisors Professor Nikolaos Gatsonis and Professor Michael Demetriou for their guidance and support during my academic studies at WPI. I would also like to thank Professor John Burns and Professor Raghvendra Cowlagi for serving as my committee members.

I am very thankful to my family for encouraging me to pursue my PhD. I especially would like to express gratitude to my husband for being with me and supporting in achieving this goal, and to my father for his guidance and academic advice while working on the CFD part of my work.

I would also like to acknowledge Dr. Raffaele Potami for his assistance in coding at the beginning of my program, and Professor Cowlagi for his essential help with the visualization of the UAV dynamics.

I would like to thank my friends, officemates and classmates for making every day interesting and enjoyable experience.

I am grateful for the financial support provided by the Mechanical Engineering Department at WPI through Teaching Assistant positions as well as the AFOSR, grant FA9550-12-1-0114, through Research Assistant position.

Finally, I would like to thank Randy, Sia, Donna, Barbara E., Barbara F. for being helpful when problems or questions arise.

Contents

List of Figures

List of Tables

Chapter 1. Introduction

Estimation of the concentration from a gas release in the atmosphere and the detection of the gaseous source location constitute significant research tasks with diverse applications. For example, the accidental or deliberate release of gases from a moving surface or aerial vehicle results in a plume which can be utilized for a prompt detection of the vehicle's position. A plume detection scheme that can provide information about the vehicle's proximity allows one to develop countermeasures that neutralize the source of adversarial gas release and to reduce possible adverse effects. Another important application concerns rescue missions. The release of gases and odors from biological systems (e.g. humans) can help in the detection of their location. In both examples, it is essential to localize the gas source, i.e. perform input identification, and estimate the concentration distribution of the plume, i.e. perform state reconstruction.

This dissertation continues research on this topic at WPI [18], [19], [20], [21], [22], [23], [24], [25] and has been presented in [39], [40], [41], [42]. The overview of the problem is shown in Figure 1. In this scenario, an intruder is moving along an unknown trajectory, releasing hazardous gaseous materials in the atmosphere. The primary goal of this dissertation is to further develop a coupled Controls-Computational Fluid Dynamics (CFD) approach that provides the real-time estimation of the gaseous plume in the atmosphere presented by [24],

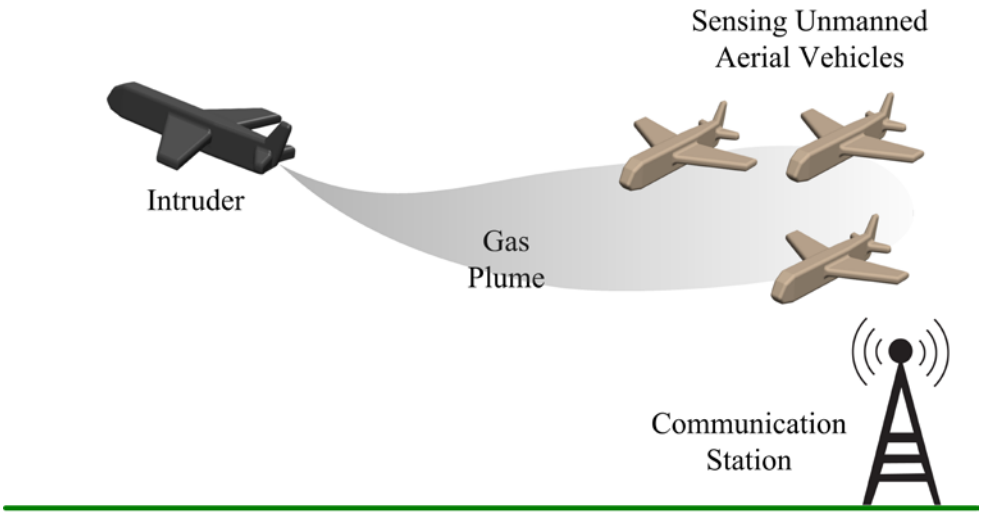

Figure 1. Schematic of the considered problem with an aerial source and a group of UAVs.

[25] using an unmanned aerial vehicle. The second goal is to apply this approach using a current unmanned aerial vehicle (UAV) equipped with a concentration sensor.

1.1 Literature Review

Plume estimation has received considerable attention and has been addressed by employing stationary, surface sensors in the plume area [1], [2], [3], [4]. In these previous works, algorithms were used to assimilate the sensor readings and embed them into gas transport models, mostly based on the advection-diffusion equation and its analytical solutions. In [1] multiple LIDARs (i.e. *Light Detection* and *Ranging*, a remote sensing method that uses light in the form of a pulsed laser to measure ranges) located at fixed positions downstream the release were used in conjunction with a numerical solution of the 3D advection-diffusion equation to estimate wind speeds, diffusivities, source location and source strength to match the measurements. In [2] multiple, fixed, ground concentration sensors are employed in order to estimate the location, height and amount of a released biological agent to fit a Gaussian plume model. In [3] the authors proposed the use of a Bayesian method and multiple concentration sensors in various configurations to obtain source localization. The source is instantaneous, stationary and is modelled as a Gaussian puff. In [4] an array of multiple fixed sensors is used for source localization through a sequential Bayesian estimation algorithm. The source is assumed to be stationary, continuous and modeled as a Gaussian plume.

The advances in autonomous surface and aerial vehicles equipped with sensors initiated applications in plume estimation and source localization. In [5] source localization is accomplished using a single moving concentration sensor in absence of vehicle dynamics. The source is assumed to be continuous and stationary and is modelled as a Gaussian plume. The estimation is based on a maximum-likelihood approach and the sensor is moving in a direction opposite to the gradient of the Cramér-Rao bound. In [6] a single moving sensor is employed for localization of a continuous, stationary area source modeled as a Gaussian plume. The estimation is based on the maximum-likelihood approach and the sensor is guided in the direction opposite to the gradient of the trace of the modified Fisher Information Matrix. The experiments in [7] performed localization of a stationary, instantaneous source of ethanol using a surface vehicle carrying a gas sensor and an anemometer. The procedure constructs a map with the possible source location using measured concentrations at specified locations and an

initial assumption of the source location. In the experiments of [8] the plume from a stationary ethanol source is estimated with a ground mobile robot that follows a predefined sweeping trajectory covering the area of interest. The estimation is based on a gas distribution modeling algorithm without the use of Gaussian models. In [9] the method is extended to compound ethanol-acetone-propanol sources. In [10] the algorithm for the UAV path planning for the plume localization is proposed. The plume is produced by a simplified Gaussian plume model for a point source. The UAV guidance uses a time recursive weighted least squares method. The approach is tested numerically in a two-dimensional domain. In [11] the localization of instantaneous and continuous point sources is considered using UAVs. Source localization is accomplished with a genetic algorithm that provides the source parameters to Gaussian and puff models from measurements taken by two UAVs flying along predefined 2D trajectories. In [12] another attempt is implemented to track the plume source using a UAV with a gradient descent controller that tracks the shortest route from the UAV to the estimated plume source provided by the Unscented Kalman Filter technique with Gaussian dispersion model. In [13] an autonomous helicopter is proposed for the localization of one or more stationary radioactive sources. The helicopter follows a predefined trajectory and measurements are used in a recursive Bayesian estimator and a contour-analysis for source localization and plume estimation. In [14], [15] the authors proposed the use of a UAV for source localization. The UAV is guided either by the plume gradient or a predefined trajectory. The source localization is based on a particle-filter algorithm. The method was applied to CO_2 and methane plumes using a quadrocopter. In [16] a swarm of fixed-wing UAVs was used for the plume detection. In this work, the UAVs were modeled as particles with a constant speed. They were initially placed randomly upwind from the plume; afterwards they began to maneuver downwind along streamlines gathering concentration information. In [17] a method is proposed for concentration estimation of a gaseous source with known location using UAVs. The guidance of the UAVs is obtained through an optimization method that uses the measurements and a Gaussian puff model.

Research on real-time plume estimation at WPI involved several aspects of the problem which are summarized below. In [18] two problems are considered: the first one proposes a method for the scheduling of static sensors in a network where it is assumed that an array of sensing devices is available to provide measurements on the state of a process governed by a

partial differential equation; the second problem considers the guidance of a mobile sensor network used in a process governed by a partial differential equation. These problems address two tasks: the improved estimation of the process state and the detection of an intruder, which is modeled as a moving source. In [19] the dispersion of a plume from a moving source is considered and a model-based estimation scheme that provides the proximity of the source location by means of a guided mobile agent that carries a sensor is proposed. The method couples grid refinement with estimation and includes a kinematic model for the mobile agent. Using Lyapunov-based method, a stable guidance scheme is provided for the spatial relocation of the moving sensor. In [20] the real time detection and state estimation of an aerial release due to a stationary or moving source in a 2D domain is investigated. A mobile sensing agent is used to provide state measurements at desired locations using a Lyapunov based guidance scheme. This problem is extended to 3D domain in [21]. In [22] the authors address the problem of spatial concentration gradient which must be computed from sensor measurements in order to implement the approach that predicts the state of the contaminant using a mobile robot. In [23] a model-based estimation scheme is implemented in order to primarily estimate the effects of the moving source with a secondary goal of estimating the proximity of the moving source using multiple sensing aerial vehicles. The vehicles do not have an ability of communication with each other. The proposed guidance scheme provides the spatial relocation of the vehicles based solely on the performance of the estimation scheme.

In [25] the authors introduced a novel approach. Unlike previous related works, this approach provides the *real-time* estimation of the gas concentration in a plume caused by a *moving* surface or aerial source using a UAV equipped with concentration sensors. The plume in this approach is assumed to be generated by a moving aerial source with unknown strength and location, and is modeled by the unsteady advection-diffusion equation with winds and eddy diffusivities. The UAV guidance is coupled with the performance of the estimator through Lyapunov redesign methods. The approach is tested numerically in a 2D domain where the UAV is gathering measurements of the concentration gradient. The process-state estimator is discretized with a finite-volume method and a first-order upwind scheme for the advection term. Several adapted computational grids are predefined a priori and switched according to the UAV repositioning in order to achieve computational efficiency. This means

that the state matrix used in the finite dimensional representation of the state observer needs to be evaluated at each of the pre-selected grids resulting in a switched dynamical system.

The theoretical aspects on the use of mobile actuators for the control of spatially varying processes has been examined primarily by A.G. Butkovskii in the 1970's, [26], [27], [28], [29], [30]. The dual problem of using mobile or scanning sensors for state estimation of distributed parameter systems has been considered by [31], and [32], [33], [34], [35]. The basic idea for scheduling sensors was based on the D-optimum experimental design that improved the lower bound of the associated Fisher Information matrix. Using a performance-based guidance, wherein the sensor moves to spatial locations that minimize the state estimation error appeared in its earlier form in [63] and [36]. This Lyapunov-based guidance assumed an *a priori* defined structure of the observer gain and using an appropriate choice of the Lyapunov function, the (Cartesian) velocities of the sensor were extracted as the desired sensor velocities. On a different approach utilizing an optimal filter (Kalman filter) for spatially varying processes, an abstract framework was proposed in [37] and subsequently developed in [38]. Both approaches, namely Lyapunov-based sensor guidance of Luenberger observer and Kalman filter with optimal sensor guidance have certain advantages. The Kalman-based filter and sensor guidance provides the optimality of the filter and the sensor motion but it is essentially an open-loop technique and requires the solution to a large dimensional differential Riccati equation (covariance) forward in time, with the sensor guidance integrated backwards in time. The Lyapunov-based sensor guidance of the non-optimal Luenberger observer is essentially closed-loop and the sensor guidance is given forward in time. This makes its real-time implementation appealing.

1.2 Objectives and Approach

The primary goal of this dissertation is to further develop a coupled CFD-control approach that provides the real-time estimate of a gaseous plume in the atmosphere presented by [18], [19], [20], [21], [22], [23], [24], [25]. The objectives and approaches used to accomplish the goal are listed below.

1. Develop aspects of the mathematical model:
    a. Expand the process model to 3D advection-diffusion equation used to describe the plume in 3D.

b. Expansion on the Lagrangian representation of the point-sensor measurements.
c. Expand in 3D the estimator model using the Luenberger observer .
d. Develop a 3D dynamical model for the UAV.
e. Modify and expand in 3D the guidance law for the UAV using Lyapunov stability analysis.
f. Extend the estimator model to include readings from multiple concentration sensors.

2. Develop aspects of the numerical model:
    a. Outline the implementation procedure.
    b. Extend the numerical implementation of the process model into 3D using finite volume method and implement a total variation diminishing (TVD) scheme for the advection term.
    c. Develop and implement a continuous grid-adaptation scheme with the areas of higher resolution near the sensor location.
    d. Implement the UAV dynamical model
    e. Implement the revised 3D guidance scheme
3. Applications
    a. Implement the proposed approach for different source trajectories and atmospheric conditions using a single sensor measurement for the estimator.
    b. Apply the proposed approach for the case of the ground intruder.
    c. Implement multiple sensor measurements into the estimator and compare the results with the data for the single sensor.

The results of this dissertation have been presented in [39], [40], [41], [42]. In [40] a continuous grid adaptation approach was developed and implemented in a 2D domain. Later this approach was extended to a 3D domain and supplemented by a point-mass dynamical model for the UAV. The numerical discretization of the estimator model was implemented in a 3D domain using a finite volume method with a total variation diminishing (TVD) scheme. The UAV motion was constrained to account for the realistic aerodynamic characteristics of the existing UAVs. The improved approach was tested for the case of the ground intruder in [41], and aerial source [42].

The dissertation is organized as follows: Chapter 2 addresses the mathematical modeling aspects of the problem under consideration, namely the physical process, the sensor and the estimator modeling, the UAV dynamics and guidance scheme. Chapter 3 describes the numerical approach and implementation. Finally, simulation results are presented in Chapter 4 for several source trajectories. Conclusions follow in Chapter 5.

Chapter 2 Mathematical Model

This chapter presents a mathematical model for the process of gas release by a moving point source, a mathematical model for the sensor measurement and estimator, and it describes the UAV dynamical model and guidance law.

2.1 Process Model

The plumes of interest in this dissertation are released in the lower layers of the atmosphere, at altitudes below 10 km. Atmospheric turbulence is responsible for the transfer of the trace (plume) gases in the lowest layers of the atmosphere [48], [49], [50]. Following [24], [25], we will derive below the "process model" which is represented by the 3D advection-diffusion equation. Consider a source of gas release, which is moving along an unknown trajectory inside a spatial domain $\Omega = \left[0, L_X\right] \times \left[0, L_Y\right] \times [0, L_Z] \in \mathbb{R}^3$. The spatial distribution of the gas source is given by the 3D Dirac measure concentrated at the point of the source's spatial centroid

$$b\left(X, Y, Z\right) = \delta\left(X - X_c(t)\right)\delta\left(Y - Y_c(t)\right)\delta\left(Z - Z_c(t)\right), \tag{2.1}$$

where $t \in \mathbb{R}^+$ is time, *X, Y,* and *Z* are the spatial variables, $\left(X_c(t), Y_c(t), Z_c(t)\right) \in \Omega$. For brevity, hereinafter the time varying centroid of the source is denoted by $\Theta_c(t) = \left(X_c(t), Y_c(t), Z_c(t)\right) \in \Omega$. The gas source is characterized by a known release rate $u(t)$ and using Eq. (2.1), it can be represented as

$$\mathcal{S}\left(t, \Theta_c\right) = b\left(X, Y, Z\right)u\left(t\right). \tag{2.2}$$

Since the flows of interest are turbulent, the fluid velocities U, V, and W in X, Y, and Z directions accordingly are random functions of space and time. They can be represented as the sum of deterministic and stochastic component as follows

$$\begin{aligned} \bar{U} &= U + U' \\ \bar{V} &= V + V' \\ \bar{W} &= W + W' \end{aligned} \tag{2.3}$$

Consider the conservation of mass of gas within an elementary volume $\Omega_c = \left(\Delta X, \Delta Y, \Delta Z\right)$ with the center at $\left(X, Y, Z\right)$, such that $\Theta_c(t) \in \Omega_c$, shown in Figure 2.

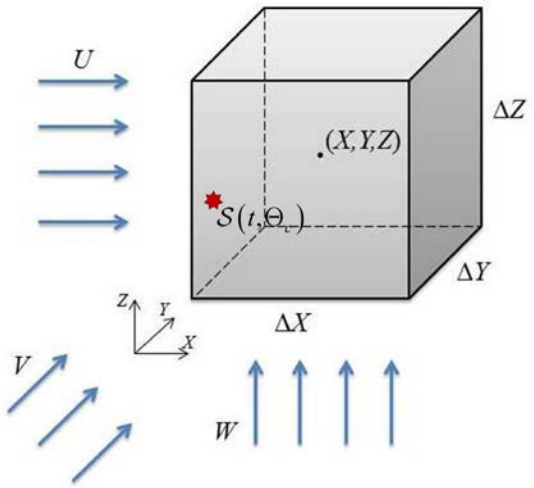

Figure 2. Schematic of an elementary volume.

Assume the case of chemically inert species, i.e. the net amount of material convected out of the volume element must be balanced only by an equivalent amount of material that is emitted by the sources and that enters by molecular diffusion. The conservation of mass $c\,\mathrm{d}\Omega_c$ or concentration c through this elementary volume is written in integral form as

$$\frac{\partial}{\partial t}\iiint\limits_{\Omega_c} c\,\mathrm{d}\Omega_c = -\oiint\limits_{A}\left(\mathbf{F}\cdot\mathbf{n}\right)\mathrm{d}A + \iiint\limits_{\Omega_c}\mathcal{S}\,\mathrm{d}\Omega_c, \tag{2.4}$$

where A is the volume surface area, $\mathbf{n}$ is the normal vector to the surface, and $\mathbf{F}$ is the total flux through the surface. Applying the Ostrogradsky-Gauss theorem yields

$$\oiint\limits_{A}\left(\mathbf{F}\cdot\mathbf{n}\right)\mathrm{d}A = \iiint\limits_{\Omega_c}\left(\nabla\cdot\mathbf{F}\right)\mathrm{d}\Omega_c \tag{2.5}$$

The gradient operator in Cartesian reference frame is $\nabla\cdot\mathbf{F} = \frac{\partial F_X}{\partial X} + \frac{\partial F_Y}{\partial Y} + \frac{\partial F_Z}{\partial Z}$. The flux through each face F_X, F_Y, and F_Z of the elementary volume is represented as a sum of advective and diffusive fluxes. According to the Fick`s law [49], the diffusive flux is proportional to the concentration gradient. Therefore, the total flux through each face is written as follows

$$
\begin{aligned}
F_X &= \left(c\bar{U}\Big|_{X-\frac{\Delta X}{2}} - D\frac{\partial c}{\partial X}\Big|_{X-\frac{\Delta X}{2}} \right) - \left(c\bar{U}\Big|_{X+\frac{\Delta X}{2}} - D\frac{\partial c}{\partial X}\Big|_{X+\frac{\Delta X}{2}} \right) \\
F_Y &= \left(c\bar{V}\Big|_{Y-\frac{\Delta Y}{2}} - D\frac{\partial c}{\partial Y}\Big|_{Y-\frac{\Delta Y}{2}} \right) - \left(c\bar{V}\Big|_{Y+\frac{\Delta Y}{2}} - D\frac{\partial c}{\partial Y}\Big|_{Y+\frac{\Delta Y}{2}} \right) \\
F_Z &= \left(c\bar{W}\Big|_{Z-\frac{\Delta Z}{2}} - D\frac{\partial c}{\partial Z}\Big|_{Z-\frac{\Delta Z}{2}} \right) - \left(c\bar{W}\Big|_{Z+\frac{\Delta Z}{2}} - D\frac{\partial c}{\partial Z}\Big|_{Z+\frac{\Delta Z}{2}} \right)
\end{aligned}
\tag{2.6}
$$

where D is molecular diffusivity. In order to express the fluxes through the faces $X+\frac{\Delta X}{2}$, $Y+\frac{\Delta Y}{2}$, and $Z+\frac{\Delta Z}{2}$ in terms of the fluxes through $X-\frac{\Delta X}{2}$, $Y-\frac{\Delta Y}{2}$, and $Z-\frac{\Delta Z}{2}$ we apply the Taylor series expansion

$$
\begin{aligned}
c\bar{U}\Big|_{X+\frac{\Delta X}{2}} &= c\bar{U}\Big|_{X-\frac{\Delta X}{2}} + \frac{\partial(c\bar{U})}{\partial X}\Big|_{X-\frac{\Delta X}{2}} \Delta X \\
c\bar{V}\Big|_{Y+\frac{\Delta Y}{2}} &= c\bar{V}\Big|_{Y-\frac{\Delta Y}{2}} + \frac{\partial(c\bar{V})}{\partial Y}\Big|_{Y-\frac{\Delta Y}{2}} \Delta Y \\
c\bar{W}\Big|_{Z+\frac{\Delta Z}{2}} &= c\bar{W}\Big|_{Z-\frac{\Delta Z}{2}} + \frac{\partial(c\bar{W})}{\partial Z}\Big|_{Z-\frac{\Delta Z}{2}} \Delta Z \\
D\frac{\partial c}{\partial X}\Big|_{X+\frac{\Delta X}{2}} &= D\frac{\partial c}{\partial X}\Big|_{X-\frac{\Delta X}{2}} + \frac{\partial}{\partial X}\left(D\frac{\partial c}{\partial X}\right)\Big|_{X-\frac{\Delta X}{2}} \Delta X \\
D\frac{\partial c}{\partial Y}\Big|_{Y+\frac{\Delta Y}{2}} &= D\frac{\partial c}{\partial Y}\Big|_{Y-\frac{\Delta Y}{2}} + \frac{\partial}{\partial Y}\left(D\frac{\partial c}{\partial Y}\right)\Big|_{Y-\frac{\Delta Y}{2}} \Delta Y \\
D\frac{\partial c}{\partial Z}\Big|_{Z+\frac{\Delta Z}{2}} &= D\frac{\partial c}{\partial Z}\Big|_{Z-\frac{\Delta Z}{2}} + \frac{\partial}{\partial Z}\left(D\frac{\partial c}{\partial Z}\right)\Big|_{Z-\frac{\Delta Z}{2}} \Delta Z
\end{aligned}
\tag{2.7}
$$

Eq. (2.7) implies that the gradient of the total flux is

$$
\nabla\cdot\mathbf{F} = -\frac{\partial(c\bar{U})}{\partial X} - \frac{\partial(c\bar{V})}{\partial Y} - \frac{\partial(c\bar{W})}{\partial Z} + \frac{\partial}{\partial X}\left(D\frac{\partial c}{\partial X}\right) + \frac{\partial}{\partial Y}\left(D\frac{\partial c}{\partial Y}\right) + \frac{\partial}{\partial Z}\left(D\frac{\partial c}{\partial Z}\right) \tag{2.8}
$$

Substituting this result into Eq. (2.4) supplemented with Eq. (2.5) and Eq. (2.3), integrating and dividing by the elementary volume Ω_c yields

$$\frac{\partial c}{\partial t}+\frac{\partial\left(c\left(U+U'\right)\right)}{\partial X}+\frac{\partial\left(c\left(V+V'\right)\right)}{\partial Y}+\frac{\partial\left(c\left(W+W'\right)\right)}{\partial Z}= \frac{\partial}{\partial X}\left(D\frac{\partial c}{\partial X}\right)+\frac{\partial}{\partial Y}\left(D\frac{\partial c}{\partial Y}\right)+\frac{\partial}{\partial Z}\left(D\frac{\partial c}{\partial Z}\right)+\mathcal{S}\left(t,\Theta_c\right) \tag{2.9}$$

Since U', V', and W' are random variables, concentrations obtained from solution of Eq. (2.9) are also random variables. Thus, the determination of a concentration c in the sense of a specified function of space and time is not possible. Instead, the mean concentration $\langle c\rangle$ should be specified, such that $c=\langle c\rangle+c'$, with $\langle c'\rangle=0$. Averaging Eq. (2.9) over an infinite ensemble of realizations of the turbulence yields

$$\frac{\partial\langle c\rangle}{\partial t}+\frac{\partial}{\partial X}\left(U\langle c\rangle+\langle U'c'\rangle\right)+\frac{\partial}{\partial Y}\left(V\langle c\rangle+\langle V'c'\rangle\right)+\frac{\partial}{\partial Z}\left(W\langle c\rangle+\langle W'c'\rangle\right)= \frac{\partial}{\partial X}\left(D\frac{\partial\langle c\rangle}{\partial X}\right)+\frac{\partial}{\partial Y}\left(D\frac{\partial\langle c\rangle}{\partial Y}\right)+\frac{\partial}{\partial Z}\left(D\frac{\partial\langle c\rangle}{\partial Z}\right)+\mathcal{S}\left(t,\Theta_c\right) \tag{2.10}$$

In order to relate the turbulent fluxes $\langle U'c'\rangle$, $\langle V'c'\rangle$, and $\langle W'c'\rangle$ to $\langle c\rangle$ we apply the mixing-length model [48]. The mixing length is a measure of the maximum distance in the fluid over which the velocity fluctuations are correlated (i.e. a measure of the eddy size). According to the mixing-length model,

$$\begin{aligned}\langle U'c'\rangle&=-K_{XX}\frac{\partial\langle c\rangle}{\partial X}\\ \langle V'c'\rangle&=-K_{YY}\frac{\partial\langle c\rangle}{\partial Y}\\ \langle W'c'\rangle&=-K_{ZZ}\frac{\partial\langle c\rangle}{\partial Z}\end{aligned} \tag{2.11}$$

where $\left\{K_{ij}\right\}$, $i,j=1,2,3$ is the eddy diffusivity tensor. In the case considered here the coordinate axes coincide with the principal axes of the tensor, therefore it has only three nonzero diagonal elements K_{XX}, K_{YY}, K_{ZZ}. Assume, in addition that molecular diffusion is negligible compared with the turbulent diffusion

$$\begin{aligned}
&\frac{\partial}{\partial X}\left(D\frac{\partial\langle c\rangle}{\partial X}\right) \ll \frac{\partial}{\partial X}\langle U'c'\rangle \\
&\frac{\partial}{\partial Y}\left(D\frac{\partial\langle c\rangle}{\partial Y}\right) \ll \frac{\partial}{\partial Y}\langle V'c'\rangle \\
&\frac{\partial}{\partial Z}\left(D\frac{\partial\langle c\rangle}{\partial Z}\right) \ll \frac{\partial}{\partial X}\langle W'c'\rangle
\end{aligned} \tag{2.12}$$

Substituting Eq. (2.11) into Eq. (2.10) with assumption (2.12) yields the advection-diffusion equation written in the so called conservative form,

$$\begin{aligned}
&\frac{\partial\langle c\rangle}{\partial t}+\frac{\partial\left(U\langle c\rangle\right)}{\partial X}+\frac{\partial\left(V\langle c\rangle\right)}{\partial Y}+\frac{\partial\left(W\langle c\rangle\right)}{\partial Z}= \\
&\frac{\partial}{\partial X}\left(K_{XX}\frac{\partial\langle c\rangle}{\partial X}\right)+\frac{\partial}{\partial Y}\left(K_{YY}\frac{\partial\langle c\rangle}{\partial Y}\right)+\frac{\partial}{\partial Z}\left(K_{ZZ}\frac{\partial\langle c\rangle}{\partial Z}\right)+\mathcal{S}\left(t,\Theta_c\right)
\end{aligned} \tag{2.13}$$

which describes the dispersion of the plume created by the point gas source in the ambient atmosphere.

Equation (2.13) is supplemented with Neumann boundary conditions $\left.\frac{\partial\langle c\rangle(t)}{\partial n}\right|_{\partial\Omega}=0$ at the boundaries of the domain Ω and an initial condition $\langle c\rangle(t=0)\big|_{\Omega}=0$.

In case of constant wind speeds U, V, W and eddy diffusivities K_{XX}, K_{YY}, K_{ZZ} the advection-diffusion equation (2.13) is written in a strong conservative form as

$$\begin{aligned}
&\frac{\partial\langle c\rangle}{\partial t}+U\frac{\partial\langle c\rangle}{\partial X}+V\frac{\partial\langle c\rangle}{\partial Y}+W\frac{\partial\langle c\rangle}{\partial Z}= \\
&K_{XX}\frac{\partial^2\langle c\rangle}{\partial X^2}+K_{YY}\frac{\partial^2\langle c\rangle}{\partial Y^2}+K_{ZZ}\frac{\partial^2\langle c\rangle}{\partial Z^2}+\mathcal{S}\left(t,\Theta_c\right)
\end{aligned} \tag{2.14}$$

In this work, the atmospheric wind speeds and eddy diffusivities are assumed to be known functions of the spatial variables. As was mentioned above, the process of gas release is considered in the lowest layer of the atmosphere, called the planetary boundary layer (PBL). The thickness of the PBL is a variable in both time and space and varies from 20-500m during nighttime hours to 0.2-5 km in the late afternoon. Since the time scale and space scale of the process under consideration is small (up to 10-15 min and up to 4 km), the thickness of the PBL in this case is considered to be constant and equal to 0.5-1 km. The mean wind speed in the PBL generally increases with height. An empirical representation of the mean wind

distribution, which is frequently used in air pollution dispersion applications is the power-law profile

$$\frac{U}{U_r} = \left(\frac{Z}{Z_r}\right)^m, \quad m \leq 1 \tag{2.15}$$

where U_r is the wind speed at the reference height Z_r and m is an exponent less or equal to unity. The parameter m depends on the surface roughness and stability. Observations have shown that surface roughness and stability increase when m increases. Under near-neutral conditions m ranges from 0.15 for smooth water, snow and ice surfaces to 0.4 for urban areas. Eddy diffusivities K_{XX}, K_{YY}, and K_{ZZ} are usually either assumed to be constants or specified as functions of height through power-law relations of the type

$$\frac{K}{K_r} = \left(\frac{Z}{Z_r}\right)^n, \quad n \leq 1 \tag{2.16}$$

where parameter n depends on the surface roughness and stability.

2.2 Sensor Model

Various sensing techniques exist to measure concentration of trace gases. These principles are based on the physical and chemical properties of the gases. Basic sensor characteristics are sensitivity, range, precision, accuracy, resolution, response time, offset, and hysteresis. Among sensing technologies, the most commonly used are electrochemical, solidelectrolite, catalytic, spectroscopic and photoionization sensors [51], [52].

In the present work, the detection and quantification of pollutants and natural trace environmental chemicals are of interest. This requires sensors with high level of sensitivity. Furthermore, the required sensor should have very small response time (within a couple of seconds) to provide measurements for the estimation process. This is due to the fact that the guidance scheme is coupled to the estimator performance and the resulting control inputs for the UAV should be processed in real time. Therefore, spectroscopic sensing technology seems to be the most acceptable for this work.

The principle of operation of a spectroscopic sensor is based on a unique absorption spectrum exhibited by each molecule. The spectrum is described in terms of absorption strength versus frequency, temperature and pressure in spectroscopic databases. The molecular

structure determines at which frequencies the incident light will be absorbed by the molecule. Among optical sensing techniques the infrared (IR)-source gas sensors are widely used.

An IR-source gas sensor contains three major parts, shown in Figure 3: the IR source, a volume of the gas sample and the IR detector. When the IR source emits broadband radiation including the wavelength absorbed by the target gas, the sample gas in the gas cell will absorb the radiation in its particular way. The optical filter is used to screen out all radiation except for the wavelength that is absorbed by the target gas. Therefore, the presence of interested gas could be detected and measured by an IR detector. This system is also known as Non-Dispersive Infrared (NDIR) gas sensor [52]. The smallest NDIR sensor modules weight approximately 5-10 grams and have size less than 40 mmx40 mmx15 mm.

The estimation process is based on in situ sensing, i.e. a sensing technique where a device is in direct contact with the environmental phenomena (here, concentration). In situ sensing in fluid environments is classified into Eulerian and Lagrangian based on the different reference frames [53]. In the present work, the Lagrangian technique is used, according to which sensors move freely in the fluid itself, and gather measurements as they moves through the environment [54], [55].

Mathematically, the gas sensor location $\Theta_s\left(t\right)=\left(X_s(t),Y_s(t),Z_s(t)\right)\in\Omega$ is described similar to the gas source location (see Eq. (2.1)) with the 3D Dirac delta function. Therefore, the sensor readings is provided via

$$y\left(t,\Theta_s\left(t\right)\right)=\int_0^{L_X}\int_0^{L_Y}\int_0^{L_Z}\langle c\rangle\left(t,X,Y,Z\right)\delta\left(X-X_s(t)\right)\delta\left(Y-Y_s(t)\right)\delta\left(Z-Z_s(t)\right)\mathrm{d}Z\mathrm{d}Y\mathrm{d}X \quad (2.17)$$

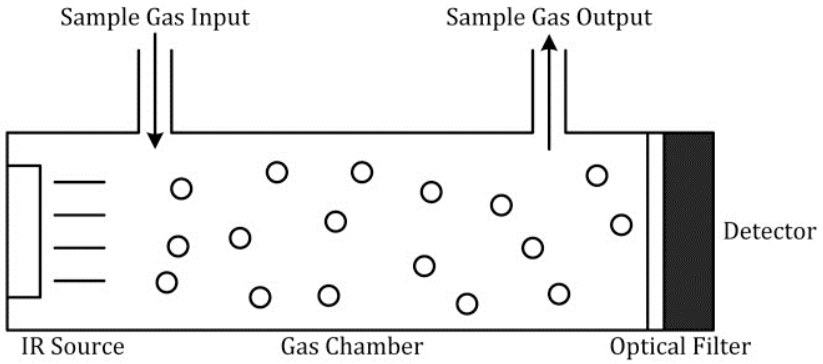

Figure 3. IR-source gas sensor based on the basic absorption spectrometry [52]. Copyright 2012 by the authors; licensee MDPI, Basel, Switzerland

2.3 Estimator Model

The estimator model is based on the advection-diffusion equation (2.13). It takes the form of a Luenberger observer supplemented with an output injection term $\mathcal{R}(t,\Theta_s)$ that is dependent on the sensor location $\Theta_s\left(t\right)$:

$$\begin{aligned}\frac{\partial\langle\hat{c}\rangle}{\partial t}+\frac{\partial\left(\langle\hat{c}\rangle U\right)}{\partial X}+\frac{\partial\left(\langle\hat{c}\rangle V\right)}{\partial Y}+\frac{\partial\left(\langle\hat{c}\rangle W\right)}{\partial Z}=\\ \frac{\partial}{\partial X}\left(K_{XX}\frac{\partial\langle\hat{c}\rangle}{\partial X}\right)+\frac{\partial}{\partial Y}\left(K_{YY}\frac{\partial\langle\hat{c}\rangle}{\partial Y}\right)+\frac{\partial}{\partial Z}\left(K_{ZZ}\frac{\partial\langle\hat{c}\rangle}{\partial Z}\right)+\mathcal{R}(t,\Theta_s)\end{aligned} \tag{2.18}$$

where $\langle\hat{c}\rangle$ is the estimated mean concentration. The boundary conditions for Eq. (2.18) are $\left.\frac{\partial\langle\hat{c}\rangle(t)}{\partial n}\right|_{\partial\Omega}=0$ and the initial conditions are $\langle\hat{c}\rangle(t=0)\big|_{\Omega}=\langle\hat{c}\rangle_0(t=0)\big|_{\Omega}$. The output injection term $\mathcal{R}(t,\Theta_s)$ is specified by the difference between a "true" concentration and a state estimate at the current UAV location, multiplied by the filter gain. The latter is taken to be a weighted multiple of the dual of the observation operator associated with the sensor`s spatial distribution given in Eq. (2.17)

$$\mathcal{R}\left(t,\Theta_s\left(t\right)\right)=\Gamma\delta\left(X-X_s(t)\right)\delta\left(Y-Y_s(t)\right)\delta\left(Z-Z_s(t)\right)\left[y\left(t,\Theta_s\right)-\langle\hat{c}\rangle\left(t,\Theta_s\right)\right] \tag{2.19}$$

where $\Gamma>0$ is a user-defined estimation gain.

2.4 UAV Dynamics and Guidance

2.4.1 Review of UAVs

Unmanned Aircraft Vehicles (UAVs) have evolved rapidly over the past decade driven primarily by military uses, and have begun finding application among civilian users for earth sensing reconnaissance and scientific data collection purposes [43]. Among advantages of the UAVs as compared to manned aircrafts is long flight duration, improved mission safety, flight repeatability due to improving autopilots, and reduced operational costs.

Classification of UAVs for civil scientific uses shown in Figure 4 is based on the characteristics such as size, flight endurance, and capabilities. The generally accepted class nomenclature is given in Table 1 [43], [44].

The LASE/LALE UAVs are most commonly used for atmospheric observations. They are relatively simple to operate, with flight controls similar to RC models and simplified ground-control stations that allow for small crews. Most of the remote sensing systems are small, simplified cameras or streaming video cameras in either daylight (color or B/W) or infrared (B/W) video provided of surface objects being imaged, although increased capabilities are enabling direct image georeferencing in some of these systems. Figure 5 shows an array of LASE/LALE UAVs.

Table 1. Classification of UAVs

UAV	Flight Duration	Altitude	Capabilities
MAV or NAV (Micro or Nano Air Vehicles)	5-30 min	<330 m	for military use: to be transported within individual soldiers' backpacks
VTOL (Vertical Take-Off and Landing)	according to the power requirements for the hovering mode	depends on the mission, usually low altitudes	require no takeoff or landing run, used in situations with terrain limitations
LASE (Low Altitude, Short-Endurance)	1-2 hours	<1500 m	light weight component and small wing span allow launching from miniature catapult systems or by hand
LALE (Low Altitude, Long Endurance)	~ 20 hours	<1500 m	may carry payloads of several kg at altitudes of a few thousand meters for extended periods

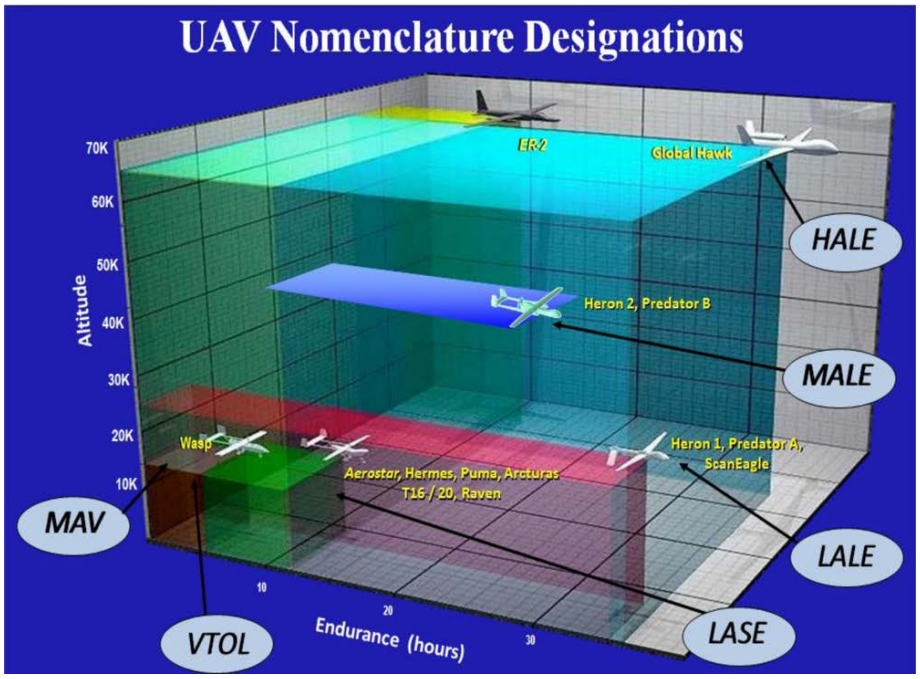

Figure 4. Image courtesy of US Department of Homeland Security [43]. Copyright 1996-2016 MDPI AG, Basel, Switzerland.

MALE (Medium Altitude, Long Endurance)	~ 20 hours	<9000 m	collect the data at regional scales and at altitudes common to manned aircrafts
HALE (High Altitude, Long Endurance)	>30 hours	>20000 m	collect information at regional and global scales to allow assessments of climate variable impacts across broad regions of the globe and to support satellite observations at spatial and temporal scales, not achievable with less capable manned or unmanned platforms

One more category of UAVs that are used for diverse civilian purposes is MUAV or Mini UAV [44]. This category relates to UAV of below a certain mass, but not as small as the MAV, capable of being hand-launched and operating at ranges of up to about 30 km.

Among the low-cost and low-risk UAVs for remote sensing expeditions, one should mention the Aerosonde® UAV. This UAV can be programmed to make very detailed flight patterns that can be flown automatically and in very extreme weather conditions. Specifications for the Aerosonde® UAV are provided below, as well as a discussion of its applications and advantages [45].

Figure 5. LASE and LALE UAS on display at 2005 Naval Unmanned Aerial Vehicle Air Demo [43]. Copyright 1996-2016 MDPI AG, Basel, Switzerland.

2.4.2 Coordinate frames

To derive the dynamic model for the UAV, the inertial and the body coordinate systems (or frames) are required [56], [57], [58]. The inertia frame is used in applying Newton's law and is the frame in which GPS provides position and speed. The body-fixed frame is often used for describing the aerodynamics forces as well as for on-board sensors, such as accelerometers and rate gyros. Therefore it is important to identify these coordinate frames and to describe the transformation between them.

For a short-range UAV (with the flight duration of up to 10 hours and maximum distance of several kilometers) the earth is assumed to be flat and non-rotating. The inertial coordinate frame is an earth-fixed coordinate system denoted by $\mathcal{F}^i$ and is depicted in Figure 6. The unit vectors $\hat{\mathbf{X}}$, $\hat{\mathbf{Y}}$, and $\hat{\mathbf{Z}}$ are directed north, east and towards the earth center respectively. The body coordinate frame, which is denoted by $\mathcal{F}^b$, has the origin at the center of mass of the vehicle. The axes are directed as follows: $\hat{\mathbf{x}}$ points out the nose of the airframe, $\hat{\mathbf{y}}$ points out the right wing, and $\hat{\mathbf{z}}$ points out the belly. The body frame $\mathcal{F}^b$ is obtained from the inertial frame $\mathcal{F}^i$ by the four consecutive transformations, depicted in Figure 6.

- Translation of the origin of the $\mathcal{F}^i$ reference frame to the center of mass of the vehicle to result in the vehicle frame $\mathcal{F}^v$
- Positive right-handed rotation about the $\hat{\mathbf{z}}^v$ axis by the heading (yaw) angle ψ to result in the vehicle-1 reference frame $\mathcal{F}^{v1}$
- Positive right-handed rotation about the $\hat{\mathbf{y}}^{v1}$ axis by the pitch angle θ to result in the vehicle-2 reference frame $\mathcal{F}^{v2}$
- Positive right-handed rotation about the $\hat{\mathbf{x}}^{v2}$ axis by the roll (bank) angle ϕ.

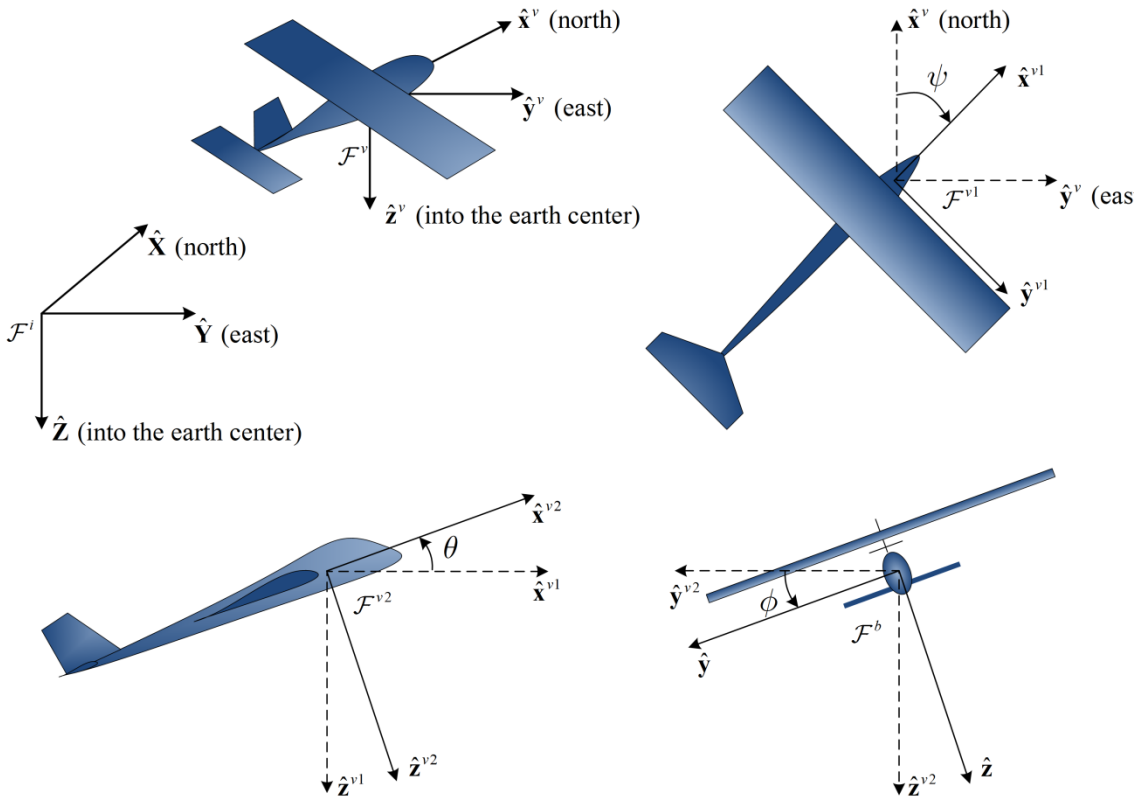

Figure 6. Transformation from the inertial frame to the body frame.

The transformation of an arbitrary vector $\mathbf{p}$ from the vehicle frame $\mathcal{F}^v$ to the body frame $\mathcal{F}^b$ is given by

$$\begin{aligned}\mathbf{p}^b &= \mathcal{R}_v^b\left(\phi,\theta,\psi\right)\mathbf{p}^v = \mathcal{R}_{v2}^b\left(\phi\right)\mathcal{R}_{v1}^{v2}\left(\theta\right)\mathcal{R}_v^{v1}\left(\psi\right)\mathbf{p}^v \\ &= \begin{pmatrix}1 & 0 & 0\\ 0 & \cos\phi & \sin\phi\\ 0 & -\sin\phi & \cos\phi\end{pmatrix}\begin{pmatrix}\cos\theta & 0 & -\sin\theta\\ 0 & 1 & 0\\ \sin\theta & 0 & \cos\theta\end{pmatrix}\begin{pmatrix}\cos\psi & \sin\psi & 0\\ -\sin\psi & \cos\psi & 0\\ 0 & 0 & 1\end{pmatrix}\mathbf{p}^v \\ &= \begin{pmatrix}C_\theta C_\psi & C_\theta S_\psi & -S_\theta\\ S_\phi S_\theta C_\psi - C_\phi S_\psi & S_\phi S_\theta S_\psi + C_\phi C_\psi & S_\phi C_\theta\\ C_\phi S_\theta C_\psi + S_\phi S_\psi & C_\phi S_\theta S_\psi - S_\phi C_\psi & C_\phi C_\theta\end{pmatrix}\mathbf{p}^v\end{aligned} \qquad (2.20)$$

where $\mathcal{R}_v^b\left(\phi,\theta,\psi\right)$ is the transformation matrix from the vehicle frame to the body frame, $\mathcal{R}_{v2}^b$ is the transformation matrix from the reference frame $\mathcal{F}^{v2}$ to the body reference frame, $\mathcal{R}_{v1}^{v2}$ is the transformation matrix from the reference frame $\mathcal{F}^{v1}$ to the reference frame $\mathcal{F}^{v2}$, $\mathcal{R}_v^{v1}$ is the transformation matrix from the vehicle reference frame to the reference frame $\mathcal{F}^{v1}$,

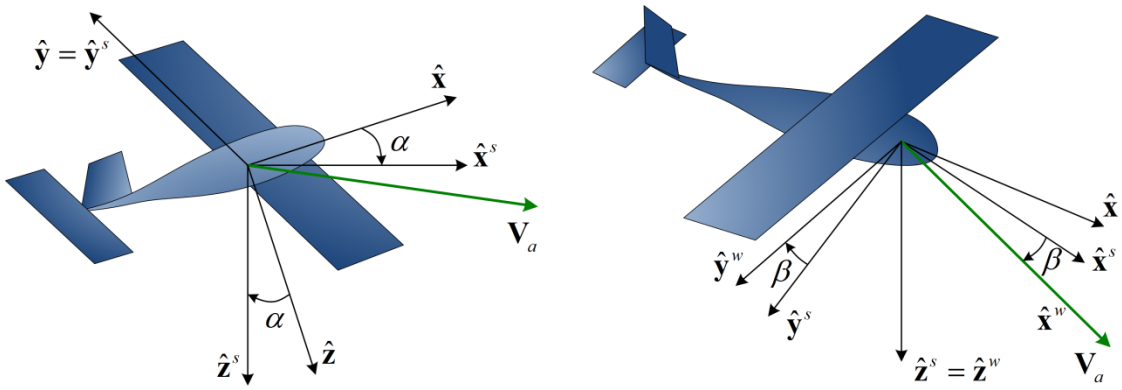

Figure 7. Transformation from the body frame to the wind frame.

$C_* \triangleq \cos*$ and $S_* \triangleq \sin*$. The matrix $\mathcal{R}_v^b$ in Eq. (2.20) represents Euler transformation matrix with Euler angles ϕ, θ, and ψ. The rotation sequence ϕ-θ-ψ is commonly used for representing aircraft orientation in three dimensions.

The wind direction relative to the body reference frame is specified using the angle of attack α and the sideslip angle β. The angle of attack α is defined as a left-handed rotation about the body $\hat{\mathbf{y}}$ axis to result in the stability reference frame $\mathcal{F}^s$ as shown in Figure 7 (left). The sideslip angle β then results from the right-handed rotation of the stability frame $\mathcal{F}^s$ about $\hat{\mathbf{z}}^s$ to yield the wind frame $\mathcal{F}^w$ as shown in Figure 7 (right). The unit vector $\hat{\mathbf{x}}$ of the wind frame $\mathcal{F}^w$ is aligned with the airspeed vector $\mathbf{V}_a$ which is the velocity of the airframe relative to the surrounding air. Therefore, the transformation of an arbitrary vector $\mathbf{p}$ from the body frame $\mathcal{F}^b$ to the wind frame $\mathcal{F}^w$ is given by

$$\begin{aligned}\mathbf{p}^s &= \mathcal{R}_b^w(\alpha,\beta)\mathbf{p}^b = \mathcal{R}_b^s(\alpha)\mathcal{R}_s^w(\beta)\mathbf{p}^b \\ &= \begin{pmatrix}\cos\alpha & 0 & \sin\alpha \\ 0 & 1 & 0 \\ -\sin\alpha & 0 & \cos\alpha\end{pmatrix}\begin{pmatrix}\cos\beta & \sin\beta & 0 \\ -\sin\beta & \cos\beta & 0 \\ 0 & 0 & 1\end{pmatrix}\mathbf{p}^b\end{aligned} \tag{2.21}$$

with

$$\mathcal{R}_b^w(\alpha,\beta) = \begin{pmatrix}\cos\beta\cos\alpha & \sin\beta & \cos\beta\sin\alpha \\ -\sin\beta\cos\alpha & \cos\beta & -\sin\beta\sin\alpha \\ -\sin\alpha & 0 & \cos\alpha\end{pmatrix} \tag{2.22}$$

2.4.3 Wind Triangle

For a small UAV, which speed ranges from 20 to 35 m/s, the wind speed ranges from 20 to 50 percent of the airspeed, therefore, it is important to account for the effect of wind on the UAV dynamics. The inertial forces acting on the UAV are dependent on the velocity relative to a fixed inertial reference frame $\mathcal{F}^i$ referred to as ground speed $\mathbf{V}_g$, whereas the aerodynamic forces depend on the airspeed $\mathbf{V}_a$. Denoting the wind velocity relative to the inertial frame by $\mathbf{V}_w$, these velocities are related by the expression

$$\mathbf{V}_a = \mathbf{V}_g - \mathbf{V}_w \tag{2.23}$$

The relationship (2.23) is called the wind triangle. Given the wind speed components U, V, and W with respect to the inertial reference frame, i.e. north, east, and down, and using Eq. (2.20), the wind speed can be expressed in the body frame $\mathcal{F}^b$ as

$$\mathbf{V}_w^b = \mathcal{R}_v^b\left(\phi,\theta,\psi\right)\begin{pmatrix} U \\ V \\ W \end{pmatrix} = \begin{pmatrix} u_w \\ v_w \\ w_w \end{pmatrix} \tag{2.24}$$

Defining u, v, and w as the body frame components of the ground speed $\mathbf{V}_g$, and u_r, v_r, and w_r as the body frame components of the airspeed $\mathbf{V}_a$, Eq. (2.23) is written as

$$\mathbf{V}_a^b = \begin{pmatrix} u_r \\ v_r \\ w_r \end{pmatrix} = \begin{pmatrix} u - u_w \\ v - v_w \\ w - w_w \end{pmatrix} \tag{2.25}$$

On the other hand, the airspeed vector in the reference frame related to the wind $\mathcal{F}^w$ has only one nonzero component

$$\mathbf{V}_a^w = \begin{pmatrix} V_a \\ 0 \\ 0 \end{pmatrix} \tag{2.26}$$

Therefore, combining Eq. (2.22) and Eq. (2.25) yields

$$\begin{aligned}\mathbf{V}_a^b &= \begin{pmatrix} u_r \\ v_r \\ w_r \end{pmatrix} = \left(\mathcal{R}_b^w\right)^{-1} \begin{pmatrix} V_a \\ 0 \\ 0 \end{pmatrix} \\ &= \begin{pmatrix} \cos\beta\cos\alpha & -\sin\beta\cos\alpha & -\sin\alpha \\ \sin\beta & \cos\beta & -\sin\beta\sin\alpha \\ \cos\beta\sin\alpha & 0 & \cos\alpha \end{pmatrix} \begin{pmatrix} V_a \\ 0 \\ 0 \end{pmatrix} = V_a \begin{pmatrix} \cos\alpha\cos\beta \\ \sin\beta \\ \sin\alpha\cos\beta \end{pmatrix}\end{aligned} \tag{2.27}$$

Inverting Eq. (2.27) gives

$$\begin{aligned} V_a &= \sqrt{u_r^2 + v_r^2 + w_r^2} \\ \alpha &= \tan^{-1}\left(\frac{w_r}{u_r}\right) \\ \beta &= \sin^{-1}\left(\frac{v_r}{\sqrt{u_r^2 + v_r^2 + w_r^2}}\right) \end{aligned} \tag{2.28}$$

The direction of the ground speed vector relative to the inertial frame $\mathcal{F}^i$ is specified using the course angle χ and the flight path angle γ (see Figure 8). The course angle χ is defined as the angle between the horizontal component of the ground speed vector $\mathbf{V}_g$ and the vector $\hat{\mathbf{X}}$ (true north); the flight path angle γ is defined as the angle between the ground speed $\mathbf{V}_g$

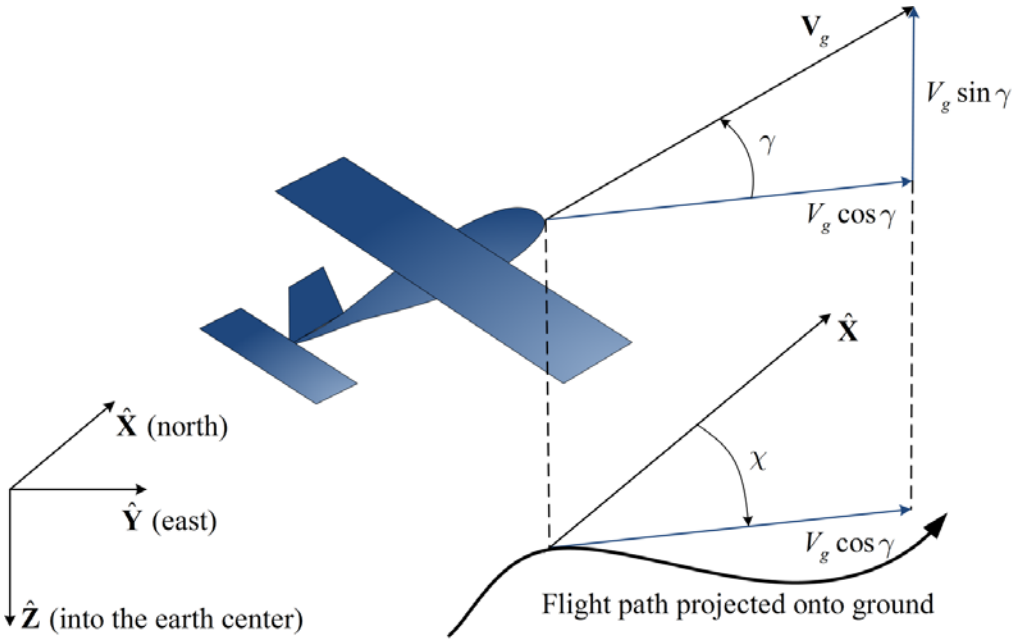

Figure 8. The flight path angle and the course angle.

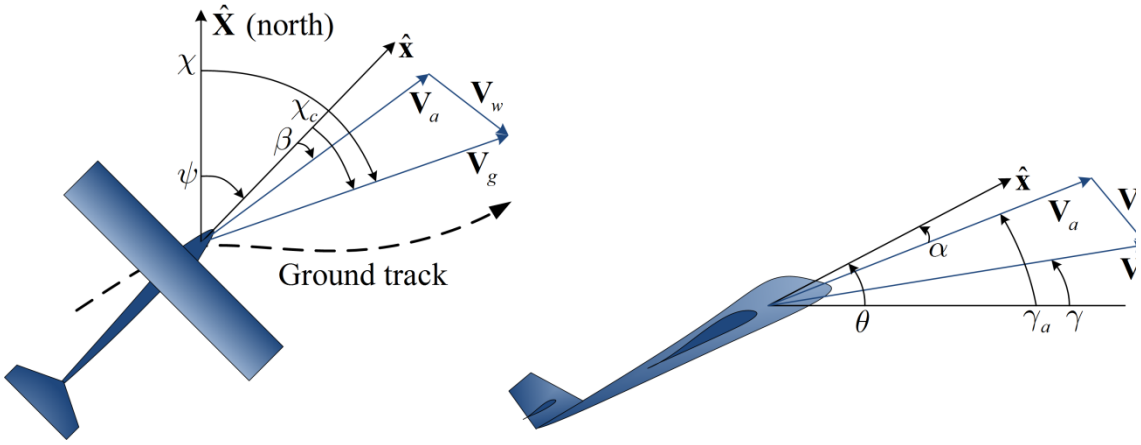

Figure 9. The wind triangle projected onto the horizontal plane (left) and vertical plane (right).

and its horizontal component. The ground speed vector in the inertial frame can be expressed in terms of χ and γ as

$$\mathbf{V}_g^i = V_g \begin{pmatrix} \cos\chi\cos\gamma \\ \sin\chi\cos\gamma \\ -\sin\gamma \end{pmatrix} \tag{2.29}$$

The geometrical representation of the concept of wind triangle is given in Figure 9. Here χ_c is referred to as crab angle and γ_a is the air-mass-referenced flight-path angle:

$$\begin{aligned} \chi_c &\triangleq \chi - \psi \\ \gamma_a &\triangleq \theta - \alpha \end{aligned} \tag{2.30}$$

Assuming sideslip angle β to be negligible so that the airspeed vector $\mathbf{V}_a$ is aligned with the $\hat{\mathbf{x}}$ axis (Figure 9), the airspeed can be expressed in the inertial frame as

$$\mathbf{V}_a^i = V_a \begin{pmatrix} \cos\psi\cos\gamma_a \\ \sin\psi\cos\gamma_a \\ -\sin\gamma_a \end{pmatrix} \tag{2.31}$$

Therefore, the wind triangle (2.23) can be rewritten as

$$V_g \begin{pmatrix} \cos\chi\cos\gamma \\ \sin\chi\cos\gamma \\ -\sin\gamma \end{pmatrix} - \begin{pmatrix} U \\ V \\ W \end{pmatrix} = V_a \begin{pmatrix} \cos\psi\cos\gamma_a \\ \sin\psi\cos\gamma_a \\ -\sin\gamma_a \end{pmatrix} \tag{2.32}$$

Taking squared norm of both sides of Eq. (2.32) yields

$$V_g^2 - 2V_g \begin{pmatrix} \cos\chi\cos\gamma \\ \sin\chi\cos\gamma \\ -\sin\gamma \end{pmatrix}^T \begin{pmatrix} U \\ V \\ W \end{pmatrix} + V_w^2 - V_a^2 = 0 \tag{2.33}$$

The third row of Eq. (2.32) is solved for the air-mass-referenced flight path angle γ_a

$$\gamma_a = \sin^{-1}\left(\frac{V_g \sin\gamma + W}{V_a}\right) \tag{2.34}$$

Multiplying both sides of Eq. (2.32) by $\left(-\sin\chi, \cos\chi, 0\right)$ and solving for the heading angle ψ yields

$$\psi = \chi - \sin^{-1}\left(\frac{1}{V_a \cos\gamma_a}\begin{pmatrix} U \\ V \end{pmatrix}^T \begin{pmatrix} -\sin\chi \\ \cos\chi \end{pmatrix}\right) \tag{2.35}$$

2.4.4 Dynamic Model

The UAV equations of motion are derived based on commonly encountered in the literature point-mass model of a fixed-wing aircraft [56], [60], [61], [62]. This model is drawn from free-body diagrams and includes lift, drag, and thrust forces.

Figure 10 provides free-body diagrams for a UAV in climbing coordinated turn: to the left the UAV is rolling at an angle of ϕ and forces are shown in $\hat{\mathbf{x}} - \hat{\mathbf{z}}$ plane, and to the right the diagram shows the view in the direction of $-\hat{\mathbf{x}}$ axis, forces are shown in $\hat{\mathbf{y}} - \hat{\mathbf{z}}$ plane. Thrust force is denoted by T, drag and lift forces are denoted by D and L respectively; M is the mass of the UAV. Applying Newton`s second law along the $\hat{\mathbf{x}}$ axis (Figure 10, left) and in the vertical direction (Figure 10, right) yields

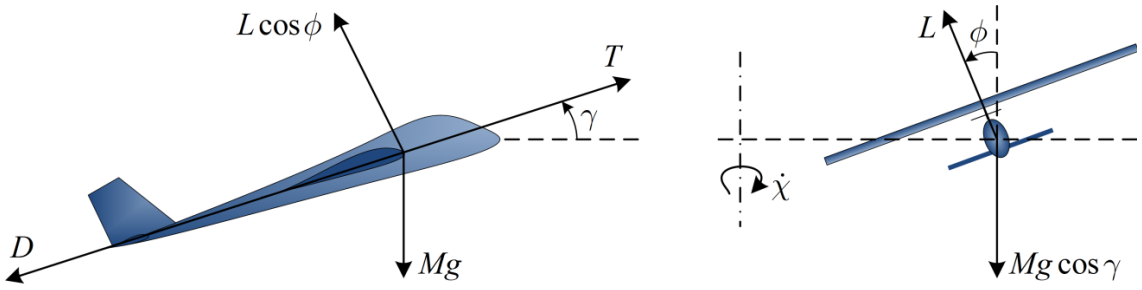

Figure 10. Free-body diagram of the forces acting on the UAV in the climbing coordinated turn.

$$M\dot{V}_g = T - D - Mg\sin\gamma \tag{2.36}$$

$$Mg\cos\gamma - L\cos\phi = 0 \tag{2.37}$$

During a coordinated turn, the bank angle ϕ is set so that there is no net side force on the UAV. In order to derive relationship for course angle χ in terms of lift L, consider the coordinated turn maneuver from the top view of horizontal plane, shown in Figure 11. The horizontal component of the lift force L is acting in the radial direction opposite to the centrifugal force, therefore the Newton`s second law results in

$$M\left(V_g\cos\gamma\right)\dot{\chi} - L\sin\phi\cos\left(\chi - \psi\right) = 0 \tag{2.38}$$

Solving Eq. (2.38) for $\dot{\chi}$ provides

$$\dot{\chi} = \frac{L\sin\phi\cos\left(\chi - \psi\right)}{MV_g\cos\gamma} \tag{2.39}$$

To derive the dynamics for the flight path angle γ, consider a pull-up maneuver in which the aircraft climbs along an arc as shown in Figure 11, so that the airframe is rolled at an angle ϕ. Newton`s second law in the radial direction gives

$$L\cos\phi - Mg\cos\gamma - MV_g\dot{\gamma} = 0 \tag{2.40}$$

Solving Eq. (2.40) for $\dot{\gamma}$ gives

$$\dot{\gamma} = \frac{L}{MV_g}\cos\phi - \frac{g}{V_g}\cos\gamma \tag{2.41}$$

Combining Eq. (2.36), Eq. (2.39), and Eq. (2.41) with the kinematic equations (2.29) yields the equations of motion that describe the point-mass model of the fixed-wing aircraft:

$$\begin{aligned}
\dot{X} &= V_g\cos\chi\cos\gamma \\
\dot{Y} &= V_g\sin\chi\cos\gamma \\
\dot{Z} &= -V_g\sin\gamma \\
\dot{V}_g &= \frac{T}{M} - \frac{D}{M} - g\sin\gamma \\
\dot{\gamma} &= \frac{L}{MV_g}\cos\phi - \frac{g}{V_g}\cos\gamma \\
\dot{\chi} &= \frac{L\sin\phi\cos\left(\chi - \psi\right)}{MV_g\cos\gamma}
\end{aligned} \tag{2.42}$$

with lift and drag being determined as

$$L = \frac{1}{2}\rho V_a^2 S C_L$$
$$D = \frac{1}{2}\rho V_a^2 S C_D \tag{2.43}$$

where C_L and C_D are lift and drag coefficients related as follows

$$C_D = C_{D_p} + \frac{C_L^2}{\pi e A R} \tag{2.44}$$

where C_{D_p} is the parasitic drag due to the shear stress of air moving over the wing; $AR \triangleq \frac{b^2}{S}$ is the wing aspect ratio; b is the wingspan, and e is the Oswald efficiency factor [56], [58]. The lift coefficient for the point-mass model (2.42) is given by the linear function of the angle of attack:

$$C_L(\alpha) = C_{L_0} + C_{L_\alpha}\alpha \tag{2.45}$$

where C_{L_0} is the lift coefficient at zero angle of attack and $C_{L_\alpha} \triangleq \frac{\partial C_L}{\partial \alpha}$ is the stability derivative. The magnitudes for C_{L_0} and C_{L_α} are found through wind tunnel tests or a detailed computational study and usually can be found in the aircraft specifications.

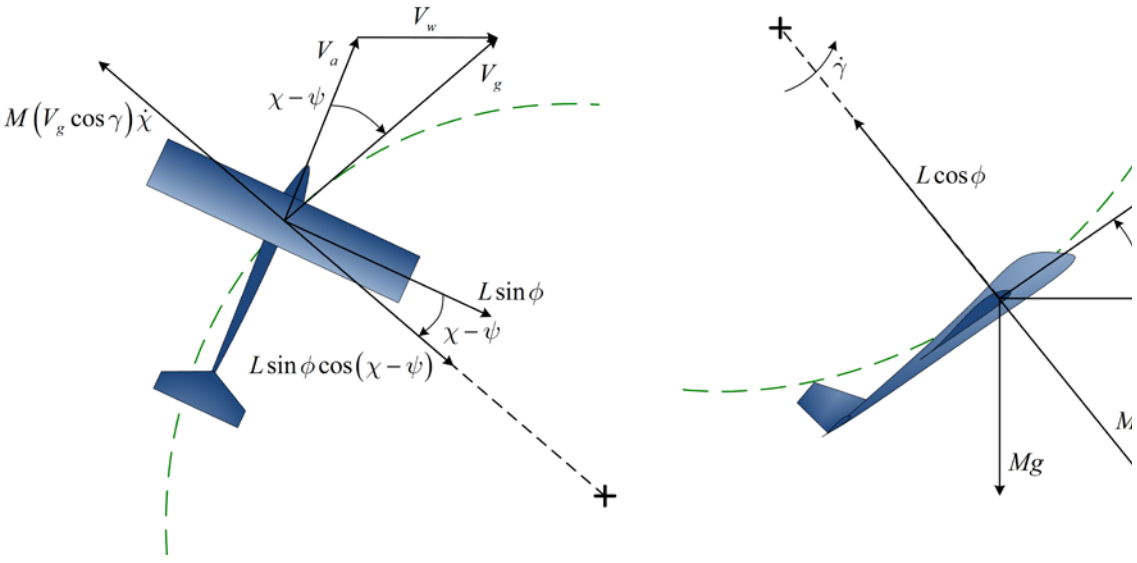

Figure 11 Free-body diagram of the forces acting on the UAV in the climbing coordinated turn: top view of the horizontal plane and side view of the vertical plane.

The engine thrust T, the bank angle ϕ, and the lift coefficient C_L are the control inputs to the dynamic model (2.42). The control inputs are assumed to stay within certain limits

$$0 \le T \le T_{\max} \qquad \left|\phi\right| \le \phi_{\max} \qquad 0 \le C_L \le C_{L\max}, \tag{2.46}$$

where $T_{\max}$, $\phi_{\max}$, and $C_{L\max}$ are pre-specified constants.

The model (2.42) is popular for simulation of the UAV motion [60], [61], [62] due to the fact that it models the aircraft response to inputs that a pilot commonly controls: engine thrust T, lift coefficient C_L, and bank angle ϕ. At the same time, it allows to avoid cumbersome relations in the 12-state model for the UAV kinematics and dynamics, which is usually used to implement autopilot for specific aircraft maneuvers.

2.4.5 UAV Guidance

In order to derive the UAV guidance scheme, it is convenient to rewrite the process model equation (2.13), and the estimator equation (2.18) in the abstract form as follows

$$\mathbf{x}_t = \mathcal{A}\mathbf{x} + \mathcal{S}\left(t, \Theta_c\right) \tag{2.47}$$

$$\hat{\mathbf{x}}_t = \mathcal{A}\hat{\mathbf{x}} + \mathcal{C}^*\Gamma\mathcal{C}\left(\mathbf{x} - \hat{\mathbf{x}}\right) \tag{2.48}$$

where $\mathbf{x}\left(t\right) = \langle c \rangle\left(t, \cdot, \cdot, \cdot\right)$ is the concentration state, $\hat{\mathbf{x}}\left(t\right)$ is the estimated concentration state, $\mathcal{A}$ is the advection diffusion operator, which is specified based on Eq. (2.13)

$$\begin{aligned}\mathcal{A}\varphi = &-\frac{\partial\left(\varphi U\right)}{\partial X} - \frac{\partial\left(\varphi V\right)}{\partial Y} - \frac{\partial\left(\varphi W\right)}{\partial Z} + \\ &\frac{\partial}{\partial X}\left(\frac{\left(\varphi K_{XX}\right)}{\partial X}\right) + \frac{\partial}{\partial Y}\left(\frac{\left(\varphi K_{YY}\right)}{\partial Y}\right) + \frac{\partial}{\partial Z}\left(\frac{\left(\varphi K_{ZZ}\right)}{\partial Z}\right)\end{aligned} \tag{2.49}$$

for $\varphi \in L_2\left(\Omega\right)$ and $\mathcal{C}$ is the output operator associated with the sensor`s spatial location

$$\mathcal{C}\varphi = \int_0^{L_X}\int_0^{L_Y}\int_0^{L_Z} \varphi\delta\left(X - X_s(t)\right)\delta\left(Y - Y_s(t)\right)\delta\left(Z - Z_s(t)\right)\mathrm{d}Z\mathrm{d}Y\mathrm{d}X \tag{2.50}$$

for all the test functions $\varphi \in H^1\left(\Omega\right)$. The UAV guidance scheme is based on the estimator performance through the state-estimation error

$e\left(t,X,Y,Z\right)=\langle c\rangle\left(t,X,Y,Z\right)-\langle\hat{c}\rangle\left(t,X,Y,Z\right)$. Combining Eq. (2.47) and Eq. (2.48) yields the governing equation for the evolution of the state estimation error

$$\mathbf{e}_t=\left(\mathcal{A}-\mathcal{C}^*\Gamma\mathcal{C}\right)\mathbf{e}+\mathcal{S}\left(t,\Theta_c\right)=\mathcal{A}_{cl}\mathbf{e}+\mathcal{S}\left(t,\Theta_c\right) \tag{2.51}$$

Equation (2.51) is supplemented with Neumann boundary conditions $\left.\frac{\partial\mathbf{e}(t)}{\partial n}\right|_{\partial\Omega}=0$, and the initial conditions are $\mathbf{e}(t=0)\big|_{\Omega}=\mathbf{e}_0(t=0)\big|_{\Omega}$.

The control inputs should be chosen so that the UAV is driven towards the spatial areas of higher estimation error. For this purpose, the Lyapunov redesign method is used with the following choice of the Lyapunov functional [63]

$$\mathcal{E}=-\left\langle\mathbf{e},\mathcal{A}_{cl}\mathbf{e}\right\rangle \tag{2.52}$$

where $\langle\cdot,\cdot\rangle$ denotes the $L_2\left(\Omega\right)$ inner product. The system is stable provided that the derivative of the Lyapunov functional in Eq. (2.52) is negative semidefinite, i.e. $\dot{\mathcal{E}}\le 0$. Taking time derivative of Eq. (2.52) yields

$$\dot{\mathcal{E}}=-2\left|\mathcal{A}_{cl}\mathbf{e}\right|^2-\left\langle\mathbf{e},\frac{\partial}{\partial t}\left(\mathcal{A}_{cl}\right)\mathbf{e}\right\rangle=-2\left|\mathcal{A}_{cl}\mathbf{e}\right|^2+\Gamma\left(\varepsilon\varepsilon_X\dot{X}+\varepsilon\varepsilon_Y\dot{Y}+\varepsilon\varepsilon_Z\dot{Z}\right) \tag{2.53}$$

where

$$\varepsilon\left(t\right)\triangleq e\left(t,\Theta_s\left(t\right)\right),\quad \varepsilon_*\left(t\right)\triangleq\frac{\partial\langle c\rangle\left(t,\Theta_s\right)}{\partial *}-\left(\frac{\partial\langle\hat{c}\rangle\left(t,\Theta_s\right)}{\partial *}\right),\quad *=X,Y,Z. \tag{2.54}$$

To ensure the derivative of the Lyapunov functional (2.53) is negative semidefinite, the UAV must have the following Cartesian velocities

$$\begin{aligned}\dot{X}^d&=-k_X\varepsilon\varepsilon_X\\ \dot{Y}^d&=-k_Y\varepsilon\varepsilon_Y\\ \dot{Z}^d&=-k_Z\varepsilon\varepsilon_Z\end{aligned} \tag{2.55}$$

where $k_X>0$, $k_Y>0$, and $k_Z>0$ are user-defined constant guidance gains.

The desired Cartesian components of the velocity vector in Eq. (2.55) yield the desired magnitude of the ground speed V_g, the course angle χ and the flight path angle γ are calculated using the second and the third equations of the dynamic model (2.42) accordingly

$$
\begin{aligned}
V_g^d &= \sqrt{\dot{X}^{d2} + \dot{Y}^{d2} + \dot{Z}^{d2}} \\
\gamma^d &= \arcsin\left(-\frac{\dot{Z}^d}{V_g^d}\right) \\
\chi^d &= \arctan 2\left(\frac{\dot{Y}^d}{\dot{X}^d}\right)
\end{aligned}
\tag{2.56}
$$

Given the values of desired ground speed and current ground speed, the desired acceleration is defined as a numerical approximation of the time derivative; the flight path rate and the course rate are represented by the first-order models [56]

$$
\begin{aligned}
\dot{V}_g^d &= \frac{V_g^d - V_g}{\Delta t} \\
\dot{\gamma}^d &= b_\gamma\left(\gamma^d - \gamma\right) \\
\dot{\chi}^d &= b_\chi\left(\chi^d - \chi\right)
\end{aligned}
\tag{2.57}
$$

where, $b_\gamma > 0$ and $b_\chi > 0$ are user-defined constants. Substituting Eq. (2.57) into the dynamic equations (2.42) supplemented with Eq. (2.43), yields the control inputs to the UAV

$$
\begin{cases}
\phi = \arctan 2\left(\dot{\chi}^d \cos\gamma^d, \left(\dot{\gamma}^d + \dfrac{g\cos\gamma^d}{V_g^d}\right)\cos\left(\chi^d - \psi\right)\right) \\
C_L = \dfrac{MV_g^d\left(\dot{\gamma}^d + \dfrac{g\cos\gamma^d}{V_g^d}\right)}{\dfrac{1}{2}\rho V_a^2 S\cos\phi} \\
T = M\dot{V}_g^d + \dfrac{1}{2}\rho V_a^2 S\left(C_{D_p} + KC_L^2\right) + Mg\sin\gamma^d
\end{cases}
\tag{2.58}
$$

The UAV is subject to realistic constraints and therefore, the control inputs (2.58) should stay within certain limits (2.46). The linear aerodynamic model is chosen for the lift and drag, therefore, $C_L^{\max}$ is set to be equal to the lift coefficient at stall i.e.,

$$
C_L^{\max} = C_L^{st} \tag{2.59}
$$

The maximum thrust, $T_{\max}$ is provided by the performance characteristics of the particular UAV used. In order to obtain the maximum bank angle, $\phi_{\max}$, the load factor defined as the ratio of the lift to the weight of the aircraft is used

$$n \triangleq \frac{L}{Mg} \tag{2.60}$$

For a small UAV in turning level flight, the maximum load factor $n_{\max}$ is usually equal to 1.5 [59]. Therefore, the condition for $\phi_{\max}$ results from the force balance equation (fifth equation in system (7)) with $\gamma = \dot{\gamma} = 0$

$$\frac{1}{\cos\phi_{\max}} = \frac{L}{Mg} \leq n_{\max} \tag{2.61}$$

2.4.6 Extension to Multiple Sensors

The desired Cartesian velocities in Eq. (2.55) are expressed in terms of the estimation error ε and the error gradients $\varepsilon_*\left(t\right)$ at the current sensor location $\Theta_s\left(t\right)$. Therefore, in order to implement the proposed guidance scheme, we should have at least seven point sensor measurements. These sensors can be either attached to a single UAV or to different UAVs that maintain a rigid flying formation. The gradient is then calculated using a central difference approximation of the spatial derivative based on the six additional measurements (two in each Cartesian direction X, Y, and Z).

It seems reasonable to include additional measurements into the estimator (2.18). For this purpose, the observation operator $\mathcal{C}$ in Eq. (2.48) is given by the 7-dimensional vector

$$\mathcal{C}\varphi = \begin{pmatrix} \int_0^{L_X}\int_0^{L_Y}\int_0^{L_Z} \varphi\delta\left(X - X_{s_1}(t)\right)\delta\left(Y - Y_{s_1}(t)\right)\delta\left(Z - Z_{s_1}(t)\right)\mathrm{d}Z\mathrm{d}Y\mathrm{d}X \\ \vdots \\ \int_0^{L_X}\int_0^{L_Y}\int_0^{L_Z} \varphi\delta\left(X - X_{s_7}(t)\right)\delta\left(Y - Y_{s_7}(t)\right)\delta\left(Z - Z_{s_7}(t)\right)\mathrm{d}Z\mathrm{d}Y\mathrm{d}X \end{pmatrix} \tag{2.62}$$

for all $\varphi \in H^1\left(\Omega\right)$. The filter gain matrix Γ is a 7×7 positive definite matrix

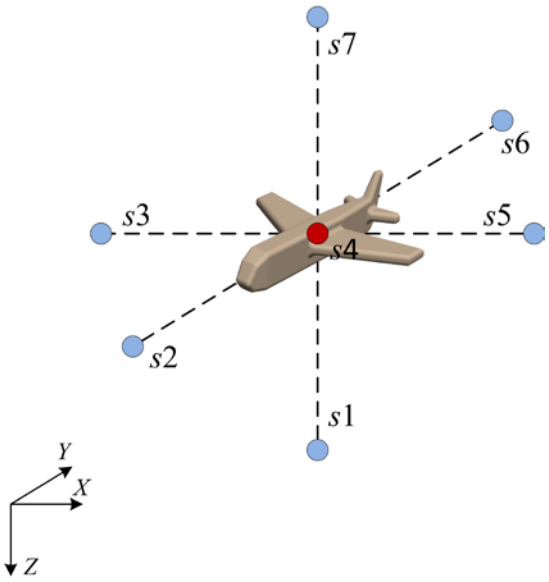

Figure 12. Example of the flying formation of UAVs for the concentration gradient measurements.

$$\Gamma = \begin{pmatrix} \Gamma_{11} & 0 & 0 \\ 0 & \ddots & 0 \\ 0 & 0 & \Gamma_{77} \end{pmatrix} \tag{2.63}$$

and which is taken to be diagonal for simplicity. A full matrix would designate an all-to-all communication between the 7 UAVs, require 7 interacting estimators. The diagonal structure of the filter gain matrix Γ ensures that there is a single centralized filter with the 6 follower UAVs in strict formation about the leader UAV (marked as s4). Therefore, the derivative of the Lyapunov functional (2.53) yields

$$\dot{\mathcal{E}} = -2\left|\mathcal{A}_{cl} e\right|^2 + \Gamma_1 \left(\varepsilon\varepsilon_X \dot{X} + \varepsilon\varepsilon_Y \dot{Y} + \varepsilon\varepsilon_Z \dot{Z}\right)\Big|_{s1} + \ldots + \Gamma_7 \left(\varepsilon\varepsilon_X \dot{X} + \varepsilon\varepsilon_Y \dot{Y} + \varepsilon\varepsilon_Z \dot{Z}\right)\Big|_{s7} \tag{2.64}$$

where the error, the error gradients, and the Cartesian velocities are calculated at each sensor location denoted by $s1, \ldots s7$.

Consider a flying formation, where all the vehicles maintain a constant distance from the leader UAV (denoted by $s4$), shown in Figure 12. In this case

$$\begin{aligned} \dot{X}_{si} &= \dot{X}_{sj} \\ \dot{Y}_{si} &= \dot{Y}_{sj} \\ \dot{Z}_{si} &= \dot{Z}_{sj} \end{aligned}, \qquad i = 1, \ldots 7, \quad j = 1, \ldots 7, \quad i \neq j \tag{2.65}$$

Therefore, denoting the Cartesian velocity components of the "leader" UAV by $\dot{X}$, $\dot{Y}$, and $\dot{Z}$, Eq. (2.64) is rewritten as

$$\begin{aligned}\dot{\mathcal{E}} = -2\left|\mathcal{A}_{cl}e\right|^2 + \dot{X}\left(\Gamma_1\varepsilon\varepsilon_X\Big|_{s1} + \ldots + \Gamma_7\varepsilon\varepsilon_X\Big|_{s7}\right) + \\ \dot{Y}\left(\Gamma_1\varepsilon\varepsilon_Y\Big|_{s1} + \ldots + \Gamma_7\varepsilon\varepsilon_Y\Big|_{s7}\right) + \dot{Z}\left(\Gamma_1\varepsilon\varepsilon_Z\Big|_{s1} + \ldots + \Gamma_7\varepsilon\varepsilon_Z\Big|_{s7}\right)\end{aligned} \tag{2.66}$$

and thus the desired Cartesian velocities that the UAVs must have are calculated as follows

$$\begin{aligned}\dot{X}^d &= -k_X\left(\Gamma_1\varepsilon\varepsilon_X\Big|_{s1} + \ldots + \Gamma_7\varepsilon\varepsilon_X\Big|_{s7}\right) \\ \dot{Y}^d &= -k_Y\left(\Gamma_1\varepsilon\varepsilon_Y\Big|_{s1} + \ldots + \Gamma_7\varepsilon\varepsilon_Y\Big|_{s7}\right) \\ \dot{Z}^d &= -k_Z\left(\Gamma_1\varepsilon\varepsilon_Z\Big|_{s1} + \ldots + \Gamma_7\varepsilon\varepsilon_Z\Big|_{s7}\right)\end{aligned} \tag{2.67}$$

The error gradient at the leader sensor location can be calculated with a central difference approach using the measurements of the followers

$$\begin{aligned}\varepsilon_X\Big|_{s4} &= \frac{\left(\langle c\rangle\Big|_{s5} - \langle c\rangle\Big|_{s3}\right)}{2dl} - \frac{\left(\langle \hat{c}\rangle\Big|_{s5} - \langle \hat{c}\rangle\Big|_{s3}\right)}{2dl} \\ \varepsilon_Y\Big|_{s4} &= \frac{\left(\langle c\rangle\Big|_{s6} - \langle c\rangle\Big|_{s2}\right)}{2dl} - \frac{\left(\langle \hat{c}\rangle\Big|_{s6} - \langle \hat{c}\rangle\Big|_{s2}\right)}{2dl} \\ \varepsilon_Z\Big|_{s4} &= \frac{\left(\langle c\rangle\Big|_{s7} - \langle c\rangle\Big|_{s1}\right)}{2dl} - \frac{\left(\langle \hat{c}\rangle\Big|_{s7} - \langle \hat{c}\rangle\Big|_{s1}\right)}{2dl}\end{aligned} \tag{2.68}$$

where dl is the distance between the leader UAV and a follower, assumed to be equal in all the directions X, Y, and Z. The error gradients at locations $s1 - s3$ and $s5 - s7$ are approximated either with the forward difference approach or with the backward difference approach using the neighbor readings.

Chapter 3 Numerical Model

In this chapter, the numerical implementation of each of the steps in the approach is discussed. First, the chapter provides the outline of the whole implementation procedure. Second, the numerical solution of the advection-diffusion equation is presented; followed by the algorithm for the computational grid adaptation. At the end of the chapter, the details for the visualization of the UAV flight are given.

3.1 Overall Estimation-CFD Implementation Procedure

The mathematical model described in Chapter 2 has been implemented numerically in the 3D domain as shown in Figure 13, with winds and eddy diffusivities representative of the ambient atmosphere at the region of interest.

The UAV starts patrolling the domain of interest following a constant-climb orbit path with predefined desired ground speed V_g^d, course angle χ^d and flight path angle γ^d as inputs to the dynamic model (2.42). The concentration sensors onboard the UAV record concentration (simulated) data according to its spatial location $\Theta_s(t)$. The state estimator (2.18) is activated when concentration measurements above the sensitivity threshold of the sensors are recorded. The concentration plume is estimated, and the UAV receives new estimator performance-based

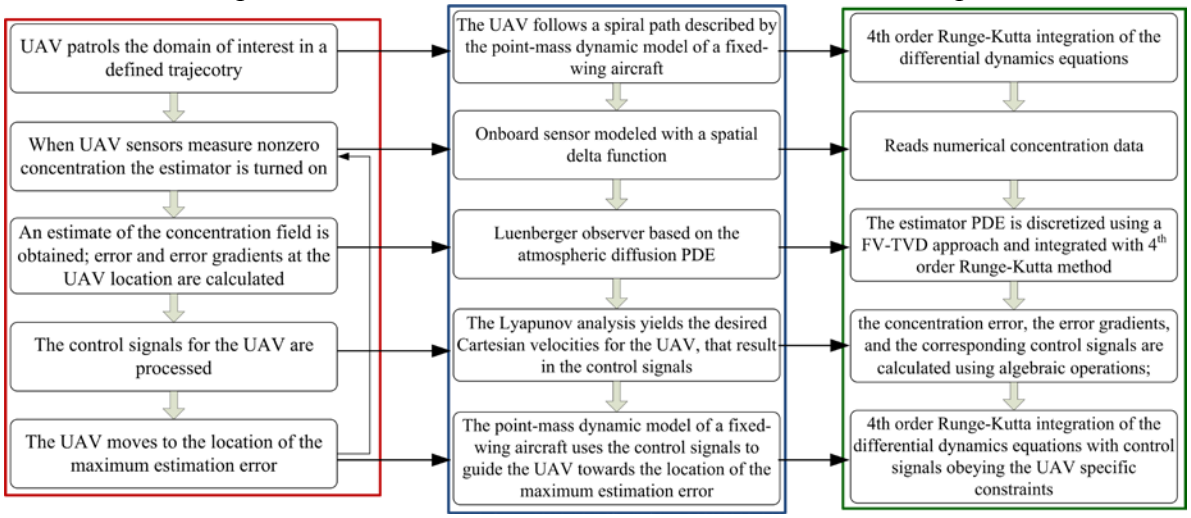

Figure 13. Real-time gaseous plume estimation approach and implementation.

control signals (2.58) that guide the vehicle towards the areas of larger estimation error. The transition from the approach to the mathematical modeling and finally to the implementation procedure is shown in Figure 13.

3.2 Numerical Solution of the Advection-Diffusion Equation

The process model advection-diffusion equation (2.13) is solved numerically in order to provide numerical data in the absence of real data using a Finite Volume Method (FVM) [64], [66] supplemented with the Total Variation Diminishing (TVD) scheme. The estimator equation (2.18) is solved numerically following the identical FVM-TVD procedure. We outline below the steps in 3D following previous 2D implementation of [24], [25].

The domain under consideration Ω is discretized with $N = N_X \times N_Y \times N_Z$ rectangular finite volumes. Integrating Eq. (2.13) over the finite volume Ω_{ijk} with surface area $\mathbf{A} = A\hat{\mathbf{n}}$ shown in Figure 14 yields

$$\frac{\partial}{\partial t}\iiint_{\Omega_{ijk}} \langle c \rangle \mathrm{d}\Omega + \oint_A \mathbf{F}\cdot\mathrm{d}\mathbf{A} = \iiint_{\Omega_{ijk}} \mathcal{S}\mathrm{d}\Omega \tag{3.1}$$

The vector of fluxes $\mathbf{F}$ represents the total flux through the surface of the volume and is expressed as a sum of advective and diffusive fluxes:

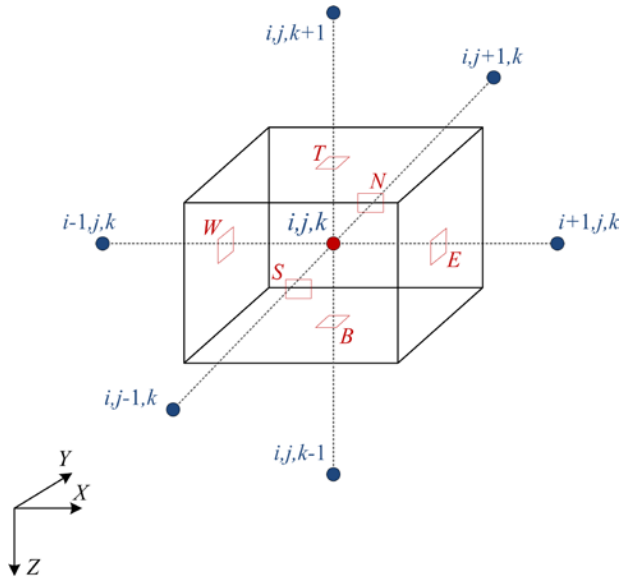

Figure 14. A finite volume at grid point (i,j,k).

$$\mathbf{F} = \left(f_X^A + f_X^D\right)\hat{\mathbf{X}} + \left(f_Y^A + f_Y^D\right)\hat{\mathbf{Y}} + \left(f_Z^A + f_Z^D\right)\hat{\mathbf{Z}} \tag{3.2}$$

Based on Eq. (2.13), the advective and diffusive fluxes in X, Y, and Z directions are calculated as follows

$$\begin{aligned} &f_X^A = \langle c\rangle U, \quad f_Y^A = \langle c\rangle V, \quad f_Z^A = \langle c\rangle W \\ &f_X^D = -K_{XX}\frac{\partial\langle c\rangle}{\partial X}, \quad f_Y^D = -K_{YY}\frac{\partial\langle c\rangle}{\partial Y}, \quad f_Z^D = -K_{ZZ}\frac{\partial\langle c\rangle}{\partial Z} \end{aligned} \tag{3.3}$$

Eq. (3.1) is replaced by its discrete form, where the volume integrals are expressed as the averaged values over the cell and where the surface integral is replaced by a sum over all the bounding faces A_l, $l = 1,...,6$ of the considered volume Ω_{ijk}

$$\frac{\partial\langle c\rangle_{ijk}}{\partial t} = -\frac{1}{\Omega_{ijk}}\sum_{l=1}^{6}\left(\mathbf{F}_{ijk}\cdot\mathbf{n}\right)A_l + \mathcal{S}_{ijk} \tag{3.4}$$

Due to the rectilinear (Cartesian) grid, the calculation of the dot product in (3.4) simplifies to

$$\frac{\partial\langle c\rangle_{ijk}}{\partial t} = \frac{-1}{\Omega_{ijk}}\left(F_{ijk}^E A_{ijk}^E - F_{ijk}^W A_{ijk}^W + F_{ijk}^N A_{ijk}^N - F_{ijk}^S A_{ijk}^S + F_{ijk}^T A_{ijk}^T - F_{ijk}^B A_{ijk}^B\right) + \mathcal{S}_{ijk} \tag{3.5}$$

Using Eq. (3.2), Eq. (3.5) can be rewritten as

$$\begin{aligned} \frac{\partial\langle c\rangle_{ijk}}{\partial t} = \frac{-1}{\Omega_{ijk}}\Bigg(&\left(f_X^A + f_X^D\right)\Big|_{ijk}^E A_{ijk}^E - \left(f_X^A + f_X^D\right)\Big|_{ijk}^W A_{ijk}^W + \\ &\left(f_Y^A + f_Y^D\right)\Big|_{ijk}^N A_{ijk}^N - \left(f_Y^A + f_Y^D\right)\Big|_{ijk}^S A_{ijk}^S + \\ &\left(f_Z^A + f_Z^D\right)\Big|_{ijk}^T A_{ijk}^T - \left(f_Z^A + f_Z^D\right)\Big|_{ijk}^B A_{ijk}^B\Bigg) + \mathcal{S}_{ijk} \end{aligned} \tag{3.6}$$

The diffusive flux is approximated with a central differencing at the cell interface [66]

$$\begin{aligned} f_X^D\Big|_{ijk}^E &= -K_X\Big|_{i,j,k}^E \frac{\langle c\rangle_{i+1,j,k} - \langle c\rangle_{i,j,k}}{X_{i+1,j,k} - X_{i,j,k}}, \quad f_X^D\Big|_{ijk}^W = -K_X\Big|_{i,j,k}^W \frac{\langle c\rangle_{i,j,k} - \langle c\rangle_{i-1,j,k}}{X_{i,j,k} - X_{i-1,j,k}} \\ f_Y^D\Big|_{ijk}^N &= -K_Y\Big|_{i,j,k}^N \frac{\langle c\rangle_{i,j+1,k} - \langle c\rangle_{i,j,k}}{Y_{i,j+1,k} - Y_{i,j,k}}, \quad f_Y^D\Big|_{ijk}^S = -K_Y\Big|_{i,j,k}^S \frac{\langle c\rangle_{i,j,k} - \langle c\rangle_{i,j-1,k}}{Y_{i,j,k} - Y_{i,j-1,k}} \\ f_Z^D\Big|_{ijk}^T &= -K_Z\Big|_{i,j,k}^T \frac{\langle c\rangle_{i,j,k+1} - \langle c\rangle_{i,j,k}}{Z_{i,j,k+1} - Z_{i,j,k}}, \quad f_Z^D\Big|_{ijk}^B = -K_Z\Big|_{i,j,k}^B \frac{\langle c\rangle_{i,j,k} - \langle c\rangle_{i,j,k-1}}{Z_{i,j,k} - Z_{i,j,k-1}} \end{aligned} \tag{3.7}$$

The advective term requires special attention in order to provide monotonicity, a condition for a numerical scheme so that no new extrema be created in case of large wind speeds near

large gradients. In previous work [23] the upwind scheme was implemented in 2D. In the 3D implementation of this dissertation the advective flux is approximated using the total variation diminishing (TVD) scheme [66], [67]. The algorithm is provided below for a simple case where $V = W = 0$ and U not zero. However, the created code assumes the possibility of nonzero wind speeds *U*, *V*, and *W*. The wind speeds are implemented either as constants or as functions of special variables according to Eq. (2.15).

$$f_X^A\Big|_{ijk}^E = \begin{cases} \langle c\rangle_{i,j,k} U_{i,j,k} + \frac{1}{2}\xi\left(r_e^+\right)\left(\langle c\rangle_{i+1,j,k} U_{i+1,j,k} - \langle c\rangle_{i,j,k} U_{i,j,k}\right), \text{ if } U\Big|_{i,j,k}^E > 0 \\ \langle c\rangle_{i+1,j,k} U_{i+1,j,k} + \frac{1}{2}\xi\left(r_e^-\right)\left(\langle c\rangle_{i,j,k} U_{i,j,k} - \langle c\rangle_{i+1,j,k} U_{i+1,j,k}\right), \text{ if } U\Big|_{i,j,k}^E < 0 \end{cases}$$
$$f_X^A\Big|_{ijk}^W = \begin{cases} \langle c\rangle_{i-1,j,k} U_{i-1,j,k} + \frac{1}{2}\xi\left(r_w^+\right)\left(\langle c\rangle_{i,j,k} U_{i,j,k} - \langle c\rangle_{i-1,j,k} U_{i-1,j,k}\right), \text{if } U\Big|_{i,j,k}^W > 0 \\ \langle c\rangle_{i,j,k} U_{i,j,k} + \frac{1}{2}\xi\left(r_w^-\right)\left(\langle c\rangle_{i-1,j,k} U_{i-1,j,k} - \langle c\rangle_{i,j,k} U_{i,j,k}\right), \text{if } U\Big|_{i,j,k}^W < 0 \end{cases} \tag{3.8}$$

The $\xi(r)$ is the limiter function of the local ratio of upstream to downstream gradient r; the "+" and "-" superscripts refer to the positive or negative wind direction respectively as :

$$r_e^+ = \left(\frac{\langle c\rangle_{i,j,k} - \langle c\rangle_{i-1,j,k}}{X_{i,j,k} - X_{i-1,j,k}} \cdot \frac{X_{i+1,j,k} - X_{i,j,k}}{\langle c\rangle_{i+1,j,k} - \langle c\rangle_{i,j,k}}\right);\ r_e^- = \left(\frac{\langle c\rangle_{i+2,j,k} - \langle c\rangle_{i+1,j,k}}{X_{i+2,j,k} - X_{i+1,j,k}} \cdot \frac{X_{i+1,j,k} - X_{i,j,k}}{\langle c\rangle_{i+1,j,k} - \langle c\rangle_{i,j,k}}\right)$$
$$r_w^+ = \left(\frac{\langle c\rangle_{i-1,j,k} - \langle c\rangle_{i-2,j,k}}{X_{i-1,j,k} - X_{i-2,j,k}} \cdot \frac{X_{i,j,k} - X_{i-1,j,k}}{\langle c\rangle_{i,j,k} - \langle c\rangle_{i-1,j,k}}\right);\ r_w^- = \left(\frac{\langle c\rangle_{i+1,j,k} - \langle c\rangle_{i,j,k}}{X_{i+1,j,k} - X_{i,j,k}} \cdot \frac{X_{i,j,k} - X_{i-1,j,k}}{\langle c\rangle_{i,j,k} - \langle c\rangle_{i-1,j,k}}\right) \tag{3.9}$$

The limiter function $\xi\left(r\right)$ is used in the TVD scheme in order to prevent discontinuities in the obtained solution. When $\xi\left(r\right) = 1$, the scheme for advection term reduces to the average of the cell centered fluxes; when $\xi\left(r\right) = 0$, the scheme reduces to the first order upwind "donor cell" scheme. For the proposed estimation algorithm, the limiter function is chosen as the Min-Mod [68]

$$\xi\left(r\right) = \begin{cases} \min\left(r,1\right) & \text{if } r > 0 \\ 0 & \text{if } r \le 0 \end{cases} \tag{3.10}$$

Assuming, $U > 0$, and substituting Eq. (3.7) and Eq. (3.8) into Eq. (3.6) yields

$$\begin{aligned}\frac{\partial\langle c\rangle_{ijk}}{\partial t}=\frac{1}{\Omega_{i,j,k}}\Bigg\{&\Bigg(\langle c\rangle_{i,j,k}U_{i,j,k}+\frac{1}{2}\xi\left(r_e^+\right)\left(\langle c\rangle_{i+1,j,k}U_{i+1,j,k}-\langle c\rangle_{i,j,k}U_{i,j,k}\right)-\\&-K_{XX}\Big|_{i,j,k}^{E}\frac{\langle c\rangle_{i+1,j,k}-\langle c\rangle_{i,j,k}}{X_{i+1,j,k}-X_{i,j,k}}\Bigg)A_{i,j,k}^{E}-\\&\Bigg(\langle c\rangle_{i-1,j,k}U_{i-1,j,k}+\frac{1}{2}\xi\left(r_w^+\right)\left(\langle c\rangle_{i,j,k}U_{i,j,k}-\langle c\rangle_{i-1,j,k}U_{i-1,j,k}\right)-\\&-K_{XX}\Big|_{i,j,k}^{W}\frac{\langle c\rangle_{i,j,k}-\langle c\rangle_{i-1,j,k}}{X_{i,j,k}-X_{i-1,j,k}}\Bigg)A_{i,j,k}^{W}-\\&K_{YY}\Big|_{i,j,k}^{N}\frac{\langle c\rangle_{i,j+1,k}-\langle c\rangle_{i,j,k}}{Y_{i,j+1,k}-Y_{i,j,k}}A_{i,j,k}^{N}+K_{YY}\Big|_{i,j,k}^{S}\frac{\langle c\rangle_{i,j,k}-\langle c\rangle_{i,j-1,k}}{Y_{i,j,k}-Y_{i,j-1,k}}A_{i,j,k}^{S}-\\&K_{ZZ}\Big|_{i,j,k}^{T}\frac{\langle c\rangle_{i,j,k+1}-\langle c\rangle_{i,j,k}}{Z_{i,j,k+1}-Z_{i,j,k}}A_{i,j,k}^{T}+K_{ZZ}\Big|_{i,j,k}^{B}\frac{\langle c\rangle_{i,j,k}-\langle c\rangle_{i,j,k-1}}{Z_{i,j,k}-Z_{i,j,k-1}}A_{i,j,k}^{B}\Bigg\}+\mathcal{S}_{i,j,k}\end{aligned}\tag{3.11}$$

The limiter function $\xi\left(r\right)$ depends on the value of concentration $\langle c\rangle$ and, therefore, varies with time. Consequently, the terms, containing multiplication by $\xi\left(r\right)$ can be considered as an additional source term, which is referred to as the TVD deferred correction source term and denoted by $\mathcal{S}^{DC}$. Thus, Eq. (3.11) can be rearranged to yield

$$\begin{aligned}\frac{\partial\langle c\rangle_{i,j,k}}{\partial t}=\frac{-1}{\Omega_{ijk}}\Big[&a_1\langle c\rangle_{i+1,j,k}+a_2\langle c\rangle_{i-1,j,k}+a_3\langle c\rangle_{i,j+1,k}+a_4\langle c\rangle_{i,j-1,k}+\\&a_5\langle c\rangle_{i,j,k+1}+a_6\langle c\rangle_{i,j,k-1}+a_0\langle c\rangle_{i,j,k}\Big]+\mathcal{S}_{i,j,k}^{DC}+\mathcal{S}_{i,j,k}\end{aligned}\tag{3.12}$$

where the coefficients $a_i,\ i=1,\ldots,6$ are calculated based on Eq. (3.11) as follows:

$$\begin{aligned}a_1&=-\frac{K_{XX}\Big|_{i,j,k}^{E}}{X_{i+1,j,k}-X_{i,j,k}}A_{i,j,k}^{E},\quad a_2=\left(-U_{i-1,j,k}-\frac{K_{XX}\Big|_{i,j,k}^{W}}{X_{i,j,k}-X_{i-1,j,k}}\right)A_{i,j,k}^{W}\\a_3&=-\frac{K_{YY}\Big|_{i,j,k}^{N}}{Y_{i,j+1,k}-Y_{i,j,k}}A_{i,j,k}^{N},\quad a_4=-\frac{K_{YY}\Big|_{i,j,k}^{S}}{Y_{i,j,k}-Y_{i,j-1,k}}A_{i,j,k}^{S}\\a_5&=-\frac{K_{ZZ}\Big|_{i,j,k}^{T}}{Z_{i,j,k+1}-Z_{i,j,k}}A_{i,j,k}^{T},\quad a_6=-\frac{K_{ZZ}\Big|_{i,j,k}^{B}}{Z_{i,j,k}-Z_{i,j,k-1}}A_{i,j,k}^{B}\end{aligned},\tag{3.13}$$

and the coefficient a_0 is defined as

$$a_0=-a_1-a_2-a_3-a_4-a_5-a_6+\left(U_{i,j,k}A_{i,j,k}^{E}-U_{i-1,j,k}A_{i,j,k}^{W}\right)\tag{3.14}$$

The deferred correction term $\mathcal{S}_{ijk}^{DC}$ results from Eq. (3.11)

$$\begin{aligned}\mathcal{S}_{ijk}^{DC} = -\frac{1}{\Omega_{ijk}}\Bigg\{&\frac{1}{2}\xi\left(r_e^+\right)\left(\langle c\rangle_{i+1,j,k}U_{i+1,j,k} - \langle c\rangle_{i,j,k}U_{i,j,k}\right)A_{i,j,k}^E - \\ &\frac{1}{2}\xi\left(r_w^+\right)\left(\langle c\rangle_{i,j,k}U_{i,j,k} - \langle c\rangle_{i-1,j,k}U_{i-1,j,k}\right)A_{i,j,k}^W\Bigg\}\end{aligned} \tag{3.15}$$

Substituting Eq. (3.7) and Eq. (3.8) into Eq. (3.6) assuming that $U<0$ yields

$$\begin{aligned}\frac{\partial\langle c\rangle_{ijk}}{\partial t} = \frac{1}{\Omega_{i,j,k}}\Bigg\{&\Bigg(\langle c\rangle_{i+1,j,k}U_{i+1,j,k} + \frac{1}{2}\xi\left(r_e^-\right)\left(\langle c\rangle_{i,j,k}U_{i,j,k} - \langle c\rangle_{i+1,j,k}U_{i+1,j,k}\right) - \\ &-K_{XX}\Big|_{i,j,k}^{E}\frac{\langle c\rangle_{i+1,j,k} - \langle c\rangle_{i,j,k}}{X_{i+1,j,k} - X_{i,j,k}}\Bigg)A_{i,j,k}^E - \\ &\Bigg(\langle c\rangle_{i,j,k}U_{i,j,k} + \frac{1}{2}\xi\left(r_w^-\right)\left(\langle c\rangle_{i-1,j,k}U_{i-1,j,k} - \langle c\rangle_{i,j,k}U_{i,j,k}\right) - \\ &-K_{XX}\Big|_{i,j,k}^{W}\frac{\langle c\rangle_{i,j,k} - \langle c\rangle_{i-1,j,k}}{X_{i,j,k} - X_{i-1,j,k}}\Bigg)A_{i,j,k}^W - \\ &K_{YY}\Big|_{i,j,k}^{N}\frac{\langle c\rangle_{i,j+1,k} - \langle c\rangle_{i,j,k}}{Y_{i,j+1,k} - Y_{i,j,k}}A_{i,j,k}^N + K_{YY}\Big|_{i,j,k}^{S}\frac{\langle c\rangle_{i,j,k} - \langle c\rangle_{i,j-1,k}}{Y_{i,j,k} - Y_{i,j-1,k}}A_{i,j,k}^S - \\ &K_{ZZ}\Big|_{i,j,k}^{T}\frac{\langle c\rangle_{i,j,k+1} - \langle c\rangle_{i,j,k}}{Z_{i,j,k+1} - Z_{i,j,k}}A_{i,j,k}^T + K_{ZZ}\Big|_{i,j,k}^{B}\frac{\langle c\rangle_{i,j,k} - \langle c\rangle_{i,j,k-1}}{Z_{i,j,k} - Z_{i,j,k-1}}A_{i,j,k}^B\Bigg\} + \mathcal{S}_{i,j,k}\end{aligned} \tag{3.16}$$

Rearranging Eq. (3.16) to the form of Eq. (3.12) results in the following coefficients $a_i,\ i=1,\ldots,6$ and a_0:

$$\begin{aligned}a_1 &= \left(U_{i+1,j,k} - \frac{K_{XX}\Big|_{i,j,k}^{E}}{X_{i+1,j,k} - X_{i,j,k}}\right)A_{i,j,k}^E, \quad a_2 = -\frac{K_{XX}\Big|_{i,j,k}^{W}}{X_{i,j,k} - X_{i-1,j,k}}A_{i,j,k}^W \\ a_3 &= -\frac{K_{YY}\Big|_{i,j,k}^{N}}{Y_{i,j+1,k} - Y_{i,j,k}}A_{i,j,k}^N, \quad a_4 = -\frac{K_{YY}\Big|_{i,j,k}^{S}}{Y_{i,j,k} - Y_{i,j-1,k}}A_{i,j,k}^S \\ a_5 &= -\frac{K_{ZZ}\Big|_{i,j,k}^{T}}{Z_{i,j,k+1} - Z_{i,j,k}}A_{i,j,k}^T, \quad a_6 = -\frac{K_{ZZ}\Big|_{i,j,k}^{B}}{Z_{i,j,k} - Z_{i,j,k-1}}A_{i,j,k}^B\end{aligned} \tag{3.17}$$

$$a_0 = -a_1 - a_2 - a_3 - a_4 - a_5 - a_6 + \left(U_{i+1,j,k}A_{i,j,k}^E - U_{i,j,k}A_{i,j,k}^W\right) \tag{3.18}$$

The deferred correction term $\mathcal{S}_{ijk}^{DC}$ is defined as

$$\mathcal{S}_{i,j,k}^{DC} = -\frac{1}{\Omega_{ijk}}\left\{\frac{1}{2}\xi\left(r_e^-\right)\left(\langle c\rangle_{i,j,k}U_{i,j,k} - \langle c\rangle_{i+1,j,k}U_{i+1,j,k}\right)A_{i,j,k}^E - \frac{1}{2}\xi\left(r_w^-\right)\left(\langle c\rangle_{i-1,j,k}U_{i-1,j,k} - \langle c\rangle_{i,j,k}U_{i,j,k}\right)A_{i,j,k}^W\right\} \tag{3.19}$$

Combining Eq. (3.13) and Eq. (3.17), the coefficients a_1 and a_2 are written in the general case as

$$\begin{aligned} a_1 &= \left(\min\left(U_{i+1,j,k},0\right) - \frac{K_{XX}\Big|_{i,j,k}^E}{X_{i+1,j,k} - X_{i,j,k}}\right)A_{i,j,k}^E \\ a_2 &= \left(-\max\left(U_{i-1,j,k},0\right) - \frac{K_{XX}\Big|_{i,j,k}^W}{X_{i,j,k} - X_{i-1,j,k}}\right)A_{i,j,k}^W \end{aligned} \tag{3.20}$$

Combining Eq. (3.14) and (3.18), the coefficient a_0 is written as

$$\begin{aligned} a_0 &= -a_1 - a_2 - a_3 - a_4 - a_5 - a_6 + \\ &\left(\max\left(U_{i,j,k},0\right) + \min\left(U_{i+1,j,k},0\right)\right)A_{i,j,k}^E - \left(\max\left(U_{i-1,j,k},0\right) + \min\left(U_{i,j,k},0\right)\right)A_{i,j,k}^W \end{aligned} \tag{3.21}$$

Finally, combining Eq. (3.15) and Eq. (3.19) yields the general expression for the deferred correction term $\mathcal{S}_{ijk}^{DC}$

$$\mathcal{S}_{ijk}^{DC} = -\frac{1}{\Omega_{ijk}}\left\{\left(\frac{1}{2}\left(\alpha_e\xi\left(r_e^+\right) - \left(1-\alpha_e\right)\xi\left(r_e^-\right)\right)\left(\langle c\rangle_{i+1,j,k}U_{i+1,j,k} - \langle c\rangle_{i,j,k}U_{i,j,k}\right)A_{i,j,k}^E\right) - \left(\frac{1}{2}\left(\alpha_w\xi\left(r_w^+\right) - \left(1-\alpha_w\right)\xi\left(r_w^-\right)\right)\left(\langle c\rangle_{i,j,k}U_{i,j,k} - \langle c\rangle_{i-1,j,k}U_{i-1,j,k}\right)A_{i,j,k}^W\right)\right\} \tag{3.22}$$

where,

$$\begin{aligned} &\alpha_e = 1 \text{ for } U_{i+1,j,k} > 0 \text{ and } \alpha_w = 1 \text{ for } U_{i-1,j,k} > 0 \\ &\alpha_e = 0 \text{ for } U_{i+1,j,k} < 0 \text{ and } \alpha_w = 0 \text{ for } U_{i-1,j,k} < 0 \end{aligned} \tag{3.23}$$

The advection-diffusion equation (2.13) (or the process model) is supplemented with Neumann boundary conditions, which implies that the flux at each physical boundary is equal to some constant value. Consider the East physical boundary $i = N_X$ of the domain under consideration. The Neumann boundary condition is written in the discretized form as follows

$$\frac{\langle c\rangle_{N_X+1,j,k} - \langle c\rangle_{N_X,j,k}}{X_{N_X+1,j,k} - X_{N_X,j,k}} = E_{b_{j,k}} \tag{3.24}$$

where $E_{b_{j,k}}$ are given values for all $j = 1,\ldots,N_Y$ and $k = 1,\ldots,N_Z$.

Expressing $\langle c \rangle_{N_X+1,j,k}$ from Eq. (3.24) and substituting it into Eq. (3.11) results in an additional component in the source term

$$\mathcal{S}_{j,k}^{BC} = \frac{K_{XX}\Big|_{N_X,j,k}^{E} E_{b_{j,k}} A_{N_X,j,k}^{E}}{\Omega_{N_X,j,k}} \tag{3.25}$$

Substituting $\langle c \rangle_{N_X+1,j,k}$ from Eq. (3.24) into Eq. (3.16) results in an additional component in the source term

$$\mathcal{S}_{j,k}^{BC} = \left\{ E_{b_{j,k}} \left(K_{XX}\Big|_{N_X,j,k}^{E} - \left(X_{N_X+1,j,k} - X_{N_X,j,k} \right) U_{N_X+1,j,k} \right) \right\} \frac{A_{N_X,j,k}^{E}}{\Omega_{N_X,j,k}} \tag{3.26}$$

Therefore combining Eq. (3.25) and Eq. (3.26) yields the expression for an additional component in the source term taking into account all possible wind directions

$$\mathcal{S}_{j,k}^{BC} = \left\{ E_{b_{j,k}} \left(K_{XX}\Big|_{N_X,j,k}^{E} - \left(X_{N_X+1,j,k} - X_{N_X,j,k} \right) \min\left(U_{N_X+1,j,k}, 0 \right) \right) \right\} \frac{A_{N_X,j,k}^{E}}{\Omega_{N_X,j,k}} \tag{3.27}$$

The volume $\left(N_X + 1, j, k \right)$ lies beyond the scope of the domain under consideration and its coordinate $X_{N_X+1,j,k}$ can be expressed in terms of $X_{N_X,j,k}$ as shown in Figure 15. The value of wind speed $U_{N_X+1,j,k}$ can be found by linear interpolation using the values of the wind speed at $X_{N_X,j,k}$ and $X_{N_X-1,j,k}$:

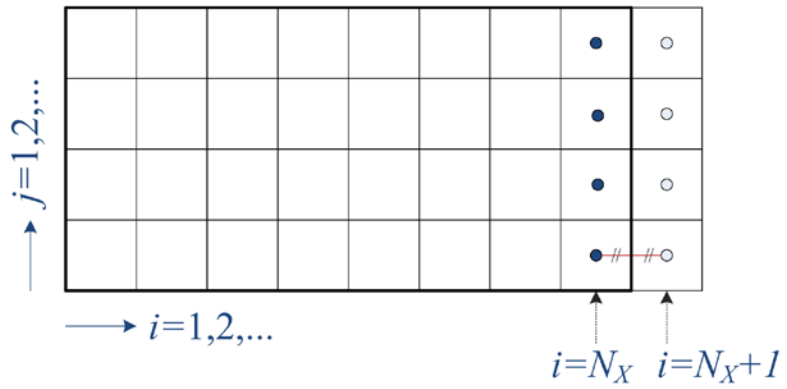

Figure 15. Finite volume discretization at the boundary.

$$U_{N_X+1,j,k} = \frac{U_{N_X,j,k} - U_{N_X-1,j,k}}{X_{N_X,j,k} - X_{N_X-1,j,k}}\left(X_{N_X+1,j,k} - X_{N_X,j,k}\right) + U_{N_X,j,k} \tag{3.28}$$

The term $\mathcal{S}_{i,j,k}$ in Eq. (3.12) is represented by a vector of $N = N_X \times N_Y \times N_Z$ entries, which are all zeros except for the single volume that corresponds to the source location $\Theta_c\left(t\right)$. Therefore based on Eq. (2.2),

$$\mathcal{S}_{ijk} = \begin{cases} 0, & \Theta_c\left(t\right) \notin \left(ijk\right) \\ \Omega_{ijk} u(t), & \Theta_c\left(t\right) \in \left(ijk\right) \end{cases} \tag{3.29}$$

The numerical solution of the estimator equation (2.18) follows the same procedure as the advection-diffusion equation with addition of the output injection term (2.19)

$$\mathcal{R}_{ijk} = \begin{cases} 0, & \Theta_s\left(t\right) \notin \left(ijk\right) \\ \Omega_{ijk}\Gamma\left(\langle c\rangle\left(t,\Theta_s\right) - \langle \hat{c}\rangle\left(t,\Theta_s\right)\right), & \Theta_s\left(t\right) \in \left(ijk\right) \end{cases} \tag{3.30}$$

The resulting set of N semidiscrete equations (3.12) are written in state space form as follows

$$\dot{\mathbf{x}}\left(t\right) = P\mathbf{x}\left(t\right) + P_{TVD}\mathbf{x}\left(t\right) + Q\left(X,Y,Z\right)u\left(t\right) \triangleq P_{RHS}\left(t\right), \tag{3.31}$$

where the source term is expressed as the product of the vector $Q\left(X,Y,Z\right)$, which represents the location information of the source, and the source release rate $u\left(t\right)$. The vector $\mathbf{x} = \langle \mathbf{c} \rangle = \left[\langle c\rangle_1, \ldots, \langle c\rangle_N\right]^T$ is the vector of states that represents the concentration for each finite volume in the computational domain Ω. The mapping for the volumes is expressed as follows

$$\begin{aligned} &n = n\left(i,j,k\right) = i + \left(j-1\right)N_X + \left(k-1\right)N_X N_Y, \\ &i = 1,\ldots,N_X, \quad j = 1,\ldots,N_Y, \quad k = 1,\ldots,N_Z, \\ &x_n = \langle c\rangle_{ijk} \end{aligned} \tag{3.32}$$

This ordering creates matrices P and P_{TVD} from Eq. (3.31) in the form

$$\begin{bmatrix} P_{11} & \cdots & P_{1N} \\ \vdots & \vdots & \vdots \\ P_{n1} & \cdots & P_{nN} \\ \vdots & \vdots & \vdots \\ P_{N1} & \cdots & P_{NN} \end{bmatrix}, \quad \begin{bmatrix} P_{TVD11} & \cdots & P_{TVD1N} \\ \vdots & \vdots & \vdots \\ P_{TVDn1} & \cdots & P_{TVDnN} \\ \vdots & \vdots & \vdots \\ P_{TVDN1} & \cdots & P_{TVDNN} \end{bmatrix} \tag{3.33}$$

The matrix P is a 7 diagonals matrix that represents the finite dimensional advection diffusion operator with entries of the coefficients a from Eq. (3.17), Eq. (3.18), Eq. (3.20), and Eq. (3.21). The matrix P_{TVD} is due to the multiplication by the limiter function.

The system of ODEs from Eq. (3.12) and Eq. (3.31) is integrated using a 4th order Runge-Kutta method [64] as

$$\begin{aligned} \mathbf{x}_{(0)} &= \mathbf{x}^{(l)} \\ \mathbf{x}_{(1)} &= \mathbf{x}_{(0)} - \frac{1}{4}\Delta t P_{RHS(0)} \\ \mathbf{x}_{(2)} &= \mathbf{x}_{(0)} - \frac{1}{3}\Delta t P_{RHS(1)} \\ \mathbf{x}_{(3)} &= \mathbf{x}_{(0)} - \frac{1}{2}\Delta t P_{RHS(2)} \\ \mathbf{x}_{(4)} &= \mathbf{x}_{(0)} - \Delta t P_{RHS(3)} \\ \mathbf{x}^{(l+1)} &= \mathbf{x}_{(4)} \end{aligned} \tag{3.34}$$

The Von Neumann method [65] is used for stability analysis of the numerical scheme. In order to do so, we consider two limiting cases for the limiter function $\xi(r)$: $\xi(r) = 0$ and $\xi(r) = 1$. At $\xi(r) = 0$, i.e. in case of the first order upwind scheme for the advective flux, assuming $\mathcal{S}_{i,j,k} = 0$, and constant eddy diffusivities and wind ($K_{XX}\big|_{i,j,k}^{E} = K_{XX}\big|_{i,j,k}^{W} = K_{XX}$, $K_{YY}\big|_{i,j,k}^{N} = K_{YY}\big|_{i,j,k}^{S} = K_{YY}$, $K_{ZZ}\big|_{i,j,k}^{T} = K_{ZZ}\big|_{i,j,k}^{B} = K_{ZZ}$, and $U_{i,j,k} = U_{i-1,j,k} = U$, $V_{i,j,k} = W_{i-1,j,k} = 0$), Eq. (3.11) is rewritten as

$$\frac{\partial \langle c \rangle_{ijk}}{\partial t} = \frac{1}{\Omega_{i,j,k}} \Big\{ -\Big(\langle c \rangle_{i,j,k} - \langle c \rangle_{i-1,j,k} \Big) U A^{E}_{i,j,k} + K_{XX} A^{E}_{i,j,k} \left(\frac{\langle c \rangle_{i+1,j,k} - \langle c \rangle_{i,j,k}}{X_{i+1,j,k} - X_{i,j,k}} - \frac{\langle c \rangle_{i,j,k} - \langle c \rangle_{i-1,j,k}}{X_{i,j,k} - X_{i-1,j,k}} \right) + K_{YY} A^{N}_{i,j,k} \left(\frac{\langle c \rangle_{i,j+1,k} - \langle c \rangle_{i,j,k}}{Y_{i,j+1,k} - Y_{i,j,k}} - \frac{\langle c \rangle_{i,j,k} - \langle c \rangle_{i,j-1,k}}{Y_{i,j,k} - Y_{i,j-1,k}} \right) + K_{ZZ} A^{T}_{i,j,k} \left(\frac{\langle c \rangle_{i,j,k+1} - \langle c \rangle_{i,j,k}}{Z_{i,j,k+1} - Z_{i,j,k}} - \frac{\langle c \rangle_{i,j,k} - \langle c \rangle_{i,j,k-1}}{Z_{i,j,k} - Z_{i,j,k-1}} \right) \Big\} \tag{3.35}$$

In the uniform grid, such that $X_{i+1,j,k} - X_{i,j,k} = X_{i,j,k} - X_{i-1,j,k} = \Delta X$, $Y_{i,j+1,k} - Y_{i,j,k} = Y_{i,j,k} - Y_{i,j-1,k} = \Delta Y$, $Z_{i,j,k+1} - Z_{i,j,k} = Z_{i,j,k} - Z_{i,j,k-1} = \Delta Z$, and $\Omega_{i,j,k} = \Delta X \Delta Y \Delta Z$, $A^{E}_{i,j,k} = \Delta Y \Delta Z$, $A^{N}_{i,j,k} = \Delta X \Delta Z$, $A^{T}_{i,j,k} = \Delta X \Delta Y$, Eq. (3.35) is written as

$$\frac{\partial \langle c \rangle_{ijk}}{\partial t} = \frac{-\Big(\langle c \rangle_{i,j,k} - \langle c \rangle_{i-1,j,k} \Big) U}{\Delta X} + K_{XX} \frac{\langle c \rangle_{i+1,j,k} - 2\langle c \rangle_{i,j,k} + \langle c \rangle_{i-1,j,k}}{\Delta X^2} + K_{YY} \frac{\langle c \rangle_{i,j+1,k} - 2\langle c \rangle_{i,j,k} + \langle c \rangle_{i,j-1,k}}{\Delta Y^2} + K_{ZZ} \frac{\langle c \rangle_{i,j,k+1} - 2\langle c \rangle_{i,j,k} + \langle c \rangle_{i,j,k-1}}{\Delta Z^2} \tag{3.36}$$

We also represent the time derivative with the first-order differencing

$$\frac{\partial \langle c \rangle_{ijk}}{\partial t} = \frac{\langle c \rangle^{l+1}_{ijk} - \langle c \rangle^{l}_{ijk}}{\Delta t} \tag{3.37}$$

By defining as the CFL number $\sigma = \frac{U \Delta t}{\Delta X}$, $\beta_X = \frac{K_{XX} \Delta t}{\Delta X^2}$, $\beta_Y = \frac{K_{YY} \Delta t}{\Delta Y^2}$, $\beta_Z = \frac{K_{ZZ} \Delta t}{\Delta Z^2}$, and using Eq. (3.37), Eq. (3.36) is rewritten as

$$\langle c \rangle^{l+1}_{i,j,k} = \langle c \rangle^{l}_{i,j,k} - \sigma \Big(\langle c \rangle^{l}_{i,j,k} - \langle c \rangle^{l}_{i-1,j,k} \Big) + \beta_X \Big(\langle c \rangle^{l}_{i+1,j,k} - 2\langle c \rangle^{l}_{i,j,k} + \langle c \rangle^{l}_{i-1,j,k} \Big) + \beta_Y \Big(\langle c \rangle^{l}_{i,j+1,k} - 2\langle c \rangle^{l}_{i,j,k} + \langle c \rangle^{l}_{i,j-1,k} \Big) + \beta_Z \Big(\langle c \rangle^{l}_{i,j,k+1} - 2\langle c \rangle^{l}_{i,j,k} + \langle c \rangle^{l}_{i,j,k-1} \Big) \tag{3.38}$$

Substituting into the numerical scheme (3.38) a Fourier mode in the form $\langle c \rangle^{l}_{i,j,k} = V^{l} e^{Ii\varphi} e^{Ij\psi} e^{Ik\theta}$, where $\varphi = k_X \Delta X$, $\psi = k_Y \Delta Y$, $\theta = k_Z \Delta Z$, with k_X, k_Y, and k_Z being the wave numbers defined as $k_X = M_X \pi / L_X$, $k_Y = M_Y \pi / L_Y$, and $k_Z = M_Z \pi / L_Z$,

where M_X, M_Y, and M_Z are numbered grid points in the X, Y, and Z directions accordingly, yields

$$\begin{aligned} V^{l+1}e^{Ii\varphi}e^{Ij\psi}e^{Ik\theta} &= V^l e^{Ii\varphi}e^{Ij\psi}e^{Ik\theta} - \sigma\left(V^l e^{Ii\varphi}e^{Ij\psi}e^{Ik\theta} - V^l e^{I(i-1)\varphi}e^{Ij\psi}e^{Ik\theta}\right) \\ &+\beta_X\left(V^l e^{I(i+1)\varphi}e^{Ij\psi}e^{Ik\theta} - 2V^l e^{Ii\varphi}e^{Ij\psi}e^{Ik\theta} + V^l e^{I(i-1)\varphi}e^{Ij\psi}e^{Ik\theta}\right) \\ &+\beta_Y\left(V^l e^{Ii\varphi}e^{I(j+1)\psi}e^{Ik\theta} - 2V^l e^{Ii\varphi}e^{Ij\psi}e^{Ik\theta} + V^l e^{Ii\varphi}e^{I(j-1)\psi}e^{Ik\theta}\right) \\ &+\beta_Z\left(V^l e^{Ii\varphi}e^{Ij\psi}e^{I(k+1)\theta} - 2V^l e^{Ii\varphi}e^{Ij\psi}e^{Ik\theta} + V^l e^{Ii\varphi}e^{Ij\psi}e^{I(k-1)\theta}\right) \end{aligned} \tag{3.39}$$

Simplifying all the terms in Eq. (3.39) by the factor $e^{Ii\varphi}e^{Ij\psi}e^{Ik\theta}$ and determining the amplification factor as $G \triangleq \dfrac{V^{l+1}}{V^l}$ yields

$$\begin{aligned} G &= 1-\sigma\left(1-e^{-I\varphi}\right)+\beta_X\left(e^{I\varphi}+e^{-I\varphi}\right)+\beta_Y\left(e^{I\psi}+e^{-I\psi}\right)+\beta_Z\left(e^{I\theta}+e^{-I\theta}\right)- \\ &\quad -2\left(\beta_X+\beta_Y+\beta_Z\right)= \\ &1-\sigma\left(1-\cos\varphi+I\sin\varphi\right)+2\beta_X\cos\varphi+2\beta_Y\cos\psi+2\beta_Z\cos\theta- \\ &\quad -2\left(\beta_X+\beta_Y+\beta_Z\right) \end{aligned} \tag{3.40}$$

For $\varphi=\psi=\theta=\pi$,

$$G = 1-2\sigma-4\left(\beta_X+\beta_Y+\beta_Z\right) \tag{3.41}$$

and the stability condition

$$\left|G\right| \le 1 \tag{3.42}$$

becomes

$$\Delta t \le \frac{1}{\dfrac{U}{\Delta X}+2\left(\dfrac{K_{XX}}{\Delta X^2}+\dfrac{K_{YY}}{\Delta Y^2}+\dfrac{K_{ZZ}}{\Delta Z^2}\right)} \tag{3.43}$$

For $\varphi=\psi=\theta=0$, $G=1$, and the stability condition is always satisfied.

At $\xi\left(r\right)=1$, i.e. in case of the central difference scheme for the advective flux, assuming $\mathcal{S}_{i,j,k}=0$, and constant eddy diffusivities and wind ($K_{XX}\Big|_{i,j,k}^{E}=K_{XX}\Big|_{i,j,k}^{W}=K_{XX}$,

$K_{YY}\Big|_{i,j,k}^{N} = K_{YY}\Big|_{i,j,k}^{S} = K_{YY}$, $K_{ZZ}\Big|_{i,j,k}^{T} = K_{ZZ}\Big|_{i,j,k}^{B} = K_{ZZ}$, and $U_{i,j,k} = U_{i-1,j,k} = U$, $V_{i,j,k} = W_{i-1,j,k} = 0$), Eq. (3.11) is written as follows

$$\begin{aligned}\frac{\partial \langle c\rangle_{ijk}}{\partial t} = \frac{1}{\Omega_{i,j,k}}\Bigg\{ & -\frac{\left(\langle c\rangle_{i+1,j,k} - \langle c\rangle_{i-1,j,k}\right)}{X_{x+1} - X_{i-1}} U A^{E}_{i,j,k} \\ & + K_{XX} A^{E}_{i,j,k}\left(\frac{\langle c\rangle_{i+1,j,k} - \langle c\rangle_{i,j,k}}{X_{i+1,j,k} - X_{i,j,k}} - \frac{\langle c\rangle_{i,j,k} - \langle c\rangle_{i-1,j,k}}{X_{i,j,k} - X_{i-1,j,k}}\right) \\ & + K_{YY} A^{N}_{i,j,k}\left(\frac{\langle c\rangle_{i,j+1,k} - \langle c\rangle_{i,j,k}}{Y_{i,j+1,k} - Y_{i,j,k}} - \frac{\langle c\rangle_{i,j,k} - \langle c\rangle_{i,j-1,k}}{Y_{i,j,k} - Y_{i,j-1,k}}\right) \\ & + K_{ZZ} A^{T}_{i,j,k}\left(\frac{\langle c\rangle_{i,j,k+1} - \langle c\rangle_{i,j,k}}{Z_{i,j,k+1} - Z_{i,j,k}} - \frac{\langle c\rangle_{i,j,k} - \langle c\rangle_{i,j,k-1}}{Z_{i,j,k} - Z_{i,j,k-1}}\right)\Bigg\}\end{aligned} \tag{3.44}$$

On the uniform grid it is written as

$$\begin{aligned}\frac{\partial \langle c\rangle_{ijk}}{\partial t} = & \frac{-\left(\langle c\rangle_{i+1,j,k} - \langle c\rangle_{i-1,j,k}\right)U}{2\Delta X} + K_{XX}\frac{\langle c\rangle_{i+1,j,k} - 2\langle c\rangle_{i,j,k} + \langle c\rangle_{i-1,j,k}}{\Delta X^2} \\ & + K_{YY}\frac{\langle c\rangle_{i,j+1,k} - 2\langle c\rangle_{i,j,k} + \langle c\rangle_{i,j-1,k}}{\Delta Y^2} + K_{ZZ}\frac{\langle c\rangle_{i,j,k+1} - 2\langle c\rangle_{i,j,k} + \langle c\rangle_{i,j,k-1}}{\Delta Z^2}\end{aligned} \tag{3.45}$$

Following now the same steps as before in Eq. (3.37), Eq. (3.38), Eq. (3.39) yields the amplification factor

$$\begin{aligned}G = & 1 - \frac{\sigma}{2}\left(e^{I\varphi} - e^{-I\varphi}\right) + \beta_X\left(e^{I\varphi} + e^{-I\varphi}\right) + \beta_Y\left(e^{I\psi} + e^{-I\psi}\right) + \beta_Z\left(e^{I\theta} + e^{-I\theta}\right) - \\ & - 2\left(\beta_X + \beta_Y + \beta_Z\right) = \\ & 1 - \sigma I\sin\varphi + 2\beta_X\cos\varphi + 2\beta_Y\cos\psi + 2\beta_Z\cos\theta - 2\left(\beta_X + \beta_Y + \beta_Z\right)\end{aligned} \tag{3.46}$$

For stability,

$$\left|G\right| \le 1 \tag{3.47}$$

Following [65] that stability condition becomes

$$\begin{aligned}\sigma^2 &\le 2\beta_x \\ \beta_x + \beta_y + \beta_z &\le \frac{1}{2}\end{aligned} \tag{3.48}$$

which provides the conditions on the timestep,

$$\Delta t \leq \frac{2K_{XX}}{U^2}$$
$$\Delta t \leq \frac{1}{2\left(\frac{K_{XX}}{\Delta X^2}+\frac{K_{YY}}{\Delta Y^2}+\frac{K_{ZZ}}{\Delta Z^2}\right)} \tag{3.49}$$

The application of the TVD numerical scheme is verified with a solution for the "pure" advection problem Eq.(2.13) with $V = W = 0$, $K_{XX} = K_{YY} = K_{ZZ} = 0$, and with an instantaneous line source. The analytical solution for this case is given by the step function and the comparison with the numerical TVD solution with the upwind scheme is shown in Figure 16.

3.3 Computational Grid Adaptation

The simulated (concentration) sensor data are generated by solving the advection-diffusion equation (2.13) on a very fine, uniform grid using as inputs the source parameters (release rate and position) and atmospheric parameters. Such a fine uniform grid would not be applicable for the desired real-time implementation of the estimator (2.18). In previous work [19], [24], [25] the grid was adapted by a priori generating several adapted grids. Each predefined grid contained an area of a refined uniform grid that covered 25% of the area of interest, whereas the rest of the domain was covered with a coarse uniform grid. In this dissertation in order to reduce the computational cost for the estimator simulation, thus

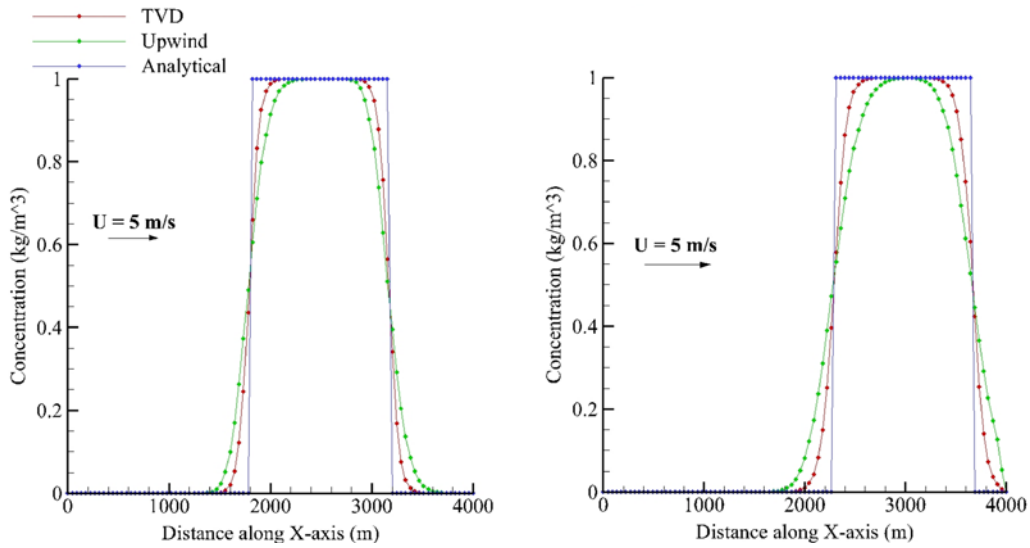

Figure 16. Verification of the numerical scheme.

obtaining real-time data, the computational grid is adapted dynamically throughout the process [69]. The adaptation algorithm uses the current UAV location as a center of a refined grid with the grid size dl in all directions. Away from the sensor, the grid nodes are following a parabolic distribution. The resulting three-dimensional grid is shown in Figure 17. As soon as the UAV crosses the distance of the minimum grid size dl a new grid is generated and the numerical solution obtained at the previous time step is interpolated to the new grid accordingly using trilinear interpolation method [70]. The total number of nodes for the adapted grid remains the same during this process.

For verification of the proposed grid adaptation algorithm, the numerical solution is compared with the steady-state analytical solution of the advection-diffusion equation for a stationary point source located at $\left(X_c, Y_c, Z_c\right)$ with a constant release rate q kg/s;

The steady state solution i.e. $\frac{\partial c}{\partial t} = 0$ results in the well-known Gaussian plume formula which for a stationary source is given as [48], [49]

$$\langle c \rangle (X, Y, \mathrm{Z}) = \frac{q}{4\pi \left(K_{XX} K_{YY} K_{ZZ}\right)^{1/2}} \times \frac{\exp\left\{-\frac{U}{2K_{XX}^{1/2}}\left[\left(\frac{\left(X-X_c\right)^2}{K_{XX}} + \frac{\left(Y-Y_c\right)^2}{K_{YY}} + \frac{\left(Z-Z_c\right)^2}{K_{ZZ}}\right)^{1/2} - \frac{\left(X-X_c\right)}{K_{XX}^{1/2}}\right]\right\}}{\left(\frac{\left(X-X_c\right)^2}{K_{XX}} + \frac{\left(Y-Y_c\right)^2}{K_{YY}} + \frac{\left(Z-Z_c\right)^2}{K_{ZZ}}\right)^{1/2}} \tag{3.50}$$

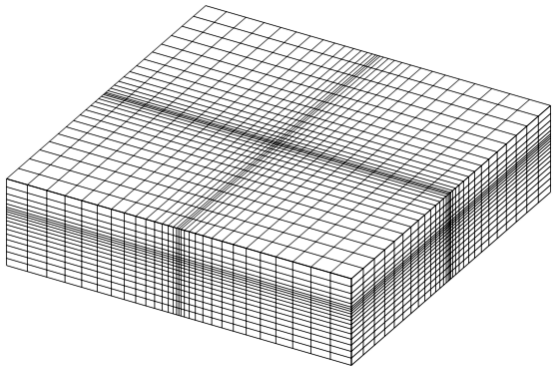

Figure 17. Adapted nonuniform computational grid.

The steady-state numerical solution is achieved at time $t \gg \frac{X}{U}$, provided that the system is advection dominated. Numerical and analytical solutions are compared in Figure 18: to the left is the concentration profile obtained on the uniform grid and to the right is the concentration profile obtained on the nonuniform adapted grid. The domain under consideration Ω has dimensions $4\ \text{km} \times 4\ \text{km} \times 1\ \text{km}$. The number of control volumes in the uniform grid is $N = 160 \times 160 \times 40$. The number of control volumes in the adapted grid is $N = 40 \times 40 \times 10$ with the smallest grid size $h_{\min} = 12.5\ \text{m}$ and the effective grid size (average between the maximum and minimum grid sizes) $h_{eff} = 100\ \text{m}$. The results are shown at time $t = 10$ min.

The accuracy of the numerical method is based on the spatial error norm [71], [72] given by

$$\text{E} = \frac{\left(\sum_{n=1}^{N} \left| \langle c \rangle_n^{numerical} - \langle c \rangle_n^{Gaussian} \right|^2 \right)^{\frac{1}{2}}}{\left\| \langle \mathbf{c} \rangle^{Gaussian} \right\|_{L^2(\Omega)}} \tag{3.51}$$

The log-log plot in Figure 19 shows the relative error (3.51) as a function of characteristic mesh size. Five grid levels are considered for the uniform grid (shown in blue in Figure 19), with $h = 200,\ 100,\ 50,\ 25,\ \text{and}\ 12.5$ m. The effective grid size for nonuniform grid (shown in red in Figure 19) ranges from 25 m up to 200 m, with the smallest grid size $h_{\min} = 12.5\ \text{m}$. The analysis shows higher accuracy of the non-uniform adapted grid at larger characteristic

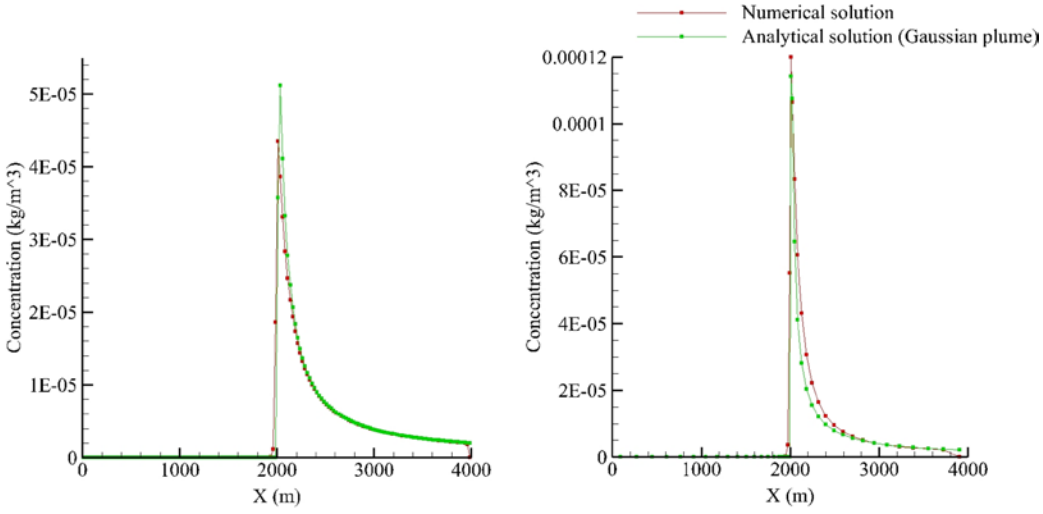

Figure 18. Grid adaptation verification: numerical solution vs. analytical formula.

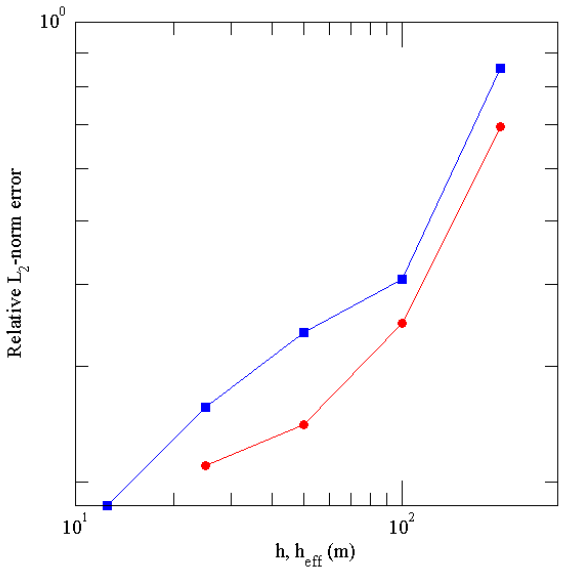

Figure 19. Relative error as a function of characteristic mesh size.

mesh sizes. The larger is the characteristic mesh size, the smaller is the number of control volumes N to be used. Smaller N results in the faster implementation of the numerical scheme. Therefore, the use of the grid adaptation is beneficial and maintains the required accuracy of the estimation provided that the number of control volumes is limited due to the necessity to implement on-line computations.

3.4 Numerical Simulation of UAV Dynamics and Guidance

The UAV state vector follows Eq. **Error! Reference source not found.** and is

$$\mathbf{p}(t) = \begin{bmatrix} X & Y & Z & V_g & \gamma & \chi \end{bmatrix}^T \tag{3.52}$$

The commanded input vector follows Eq. (2.58) and is

$$\mathbf{u} = \begin{bmatrix} \phi & C_L & T \end{bmatrix}^T \tag{3.53}$$

In order to integrate in time numerically the state vector, given the vector of commands, it is necessary to calculate all the values used in the dynamic model (2.42). Given the values for the ground speed V_g, course angle χ and flight path angle γ at the current time step, the airspeed magnitude V_a can be expressed from Eq. (2.33). The heading angle ψ is then calculated using Eq. (2.34) and Eq. (2.35). Finally, the system of ODEs (2.42), that can be written in the vector form as

$$\dot{\mathbf{p}} = f\left(t\right), \tag{3.54}$$

supplemented with Eq. (2.43) and Eq. (2.44) is integrated using 4th order Runge-Kutta method to yield the new state vector:

$$p_{k+1} = p_k + \frac{\Delta t}{6}\left(k_1 + 2k_2 + 2k_3 + k_4\right) \tag{3.55}$$

where

$$\begin{aligned} k_1 &= f\left(t_k\right) \\ k_2 &= f\left(t_k + \frac{\Delta t}{2}\right) \\ k_3 &= f\left(t_k + \frac{\Delta t}{2}\right) \\ k_4 &= f\left(t_k + \Delta t\right) \end{aligned} \tag{3.56}$$

For the flight visualization, the Euler angles θ and ψ should be calculated in addition to bank angle ϕ, which is a given control input. To calculate the heading angle ψ, the same steps are implemented as before, i.e. the airspeed magnitude V_a and the air-mass-referenced flight path angle γ_a are recalculated using Eq. (2.33) and Eq. (2.34) accordingly to be used in Eq. (2.35) The pitch angle θ results from Eq. (2.30), where the angle of attack α is calculated based on the control input C_L and Eq. (2.45).

Chapter 4 Results

4.1 Simulation Parameters

The approach presented is applied to gas releases in the atmosphere under conditions specified in Table 2 for a stationary source and a moving aerial source.

The UAV is modeled using physical parameters for the Aerosonde® UAV shown in Table 3 [45] and summarized below.

The domain under consideration has dimensions $\Omega = 4\text{km} \times 4\text{km} \times 1\text{km}$. The advection-diffusion equation (2.13) is discretized with $N = 200 \times 200 \times 50$ finite volumes. The number of finite volumes for the discretization of the estimator (2.18) is $N = 80 \times 80 \times 20$ with the minimum grid size $dl = 20\ \text{m}$. The sensor is assumed to provide noiseless measurements with the time response of 1.5-2 seconds and concentration range $\left[10^{-10}, 1\right]$ kg/m^3.

Table 2. Atmospheric parameters

Parameter	Value	Parameter	Value
Density ρ	1.2922 kg/m^3	Eddy diffusivity K_{XX}	20 m^2/s
Wind speed U	[7,9] m/s	Eddy diffusivity K_{YY}	20 m^2/s
Wind speed V	0 m/s	Eddy diffusivity K_{ZZ}	10 m^2/s
Wind speed W	0 m/s		

Table 3 UAV Specifications.

Parameter	Value	Parameter	Value
Mass M	13.5 kg	Oswald efficiency factor e	0.9
Planform area S	0.55 m^2	Parasitic drag coefficient C_{D_p}	0.0437
Wingspan b	2.8956 m	Lift coefficient in stall C_L^{st}	1.632
Cruise speed	25-30 m/s	Maximum thrust $T_{\max}$	50 N
Maximum speed	33 m/s	Maximum bank $\phi_{\max}$	30^o

4.2 Aerosonde® UAV

The Aerosonde UAV shown in Figure 20 has a wingspan of 2.9 m and weight of 13-15 kg. It is powered by 24cc fuel injected, premium unleaded gasoline. The cruise speed ranges from 20 to 40 m/s. The maximum flight duration is about 30 hours with the distance approximately 3,000 km. The maximum altitude ranges from 0.1 to 6 km depending on payload. The payload is up to 2 kg. The Aerosonde UAV is navigated by GPS and communicates via UHF radio or LEO satellite. One distinguishing feature of the Aerosonde UAV is the rear propeller, which allows for atmospheric measurements before air is disturbed by propeller.

The advantages of the Aerosonde UAV for our application are the following: it was designed specifically with scientific research applications in mind: data is high in quality as a result and all parameters related to the UAV are under control by the user; the relatively slow speed of the Aerosonde (20 to 40 m/s) allows instruments onboard to collect data at a great sampling rate; it is able to fly very close to the surface thus collecting very high resolution data.

Among the disadvantages the most crucial are the following: the total payload when fully fueled is only 2 kg, limiting the weight of instruments the Aerosonde can carry; the Aerosonde does not have the capability to detect other UAVs, aircrafts, or other obstructions in order to avoid them.

Figure 20. Aerosonde® UAV [45]. Copyright 2002, John Maurer jmaurer@hawaii.edu

The Aerosonde® UAV finds many applications such as validation of satellite-derived products: e.g. passive microwave sea ice concentrations and sea surface temperatures; support of in situ data collection efforts; imaging of sea ice in polar regions where conditions are hazardous; studying conditions leading to icing of an aircraft body during ~0°C temperatures and high humidity; development of technologies to prevent these conditions on aircraft carrying and being flown by humans (icing can potentially cause an airplane to stop functioning while in flight); atmospheric profiling and flux studies; mapping sea surface temperature at high resolutions using an infrared thermometer. In addition, micro-SAR can see through clouds and in the dark, thus being a good tool for mapping sea ice in polar regions at very a high resolution (~1-2 meters). The laser altimeter is used for producing highly detailed digital elevation models, which can be applied, for example, to study the mass balance of Greenland. Meteorological data can be collected for weather prediction and weather studies. Heavy storms can be flown into for these purposes as well, even into hurricanes.

4.3 Single Sensor

4.3.1 Stationary Source

A stationary gas source is placed inside the domain at a point with coordinates $\Theta_c(t) = \Theta_c = (1.2\text{km}, 2\,\text{km}, 0.5\,\text{km})$ releasing material continuously with $u = 1\ \text{kg/s}$. The

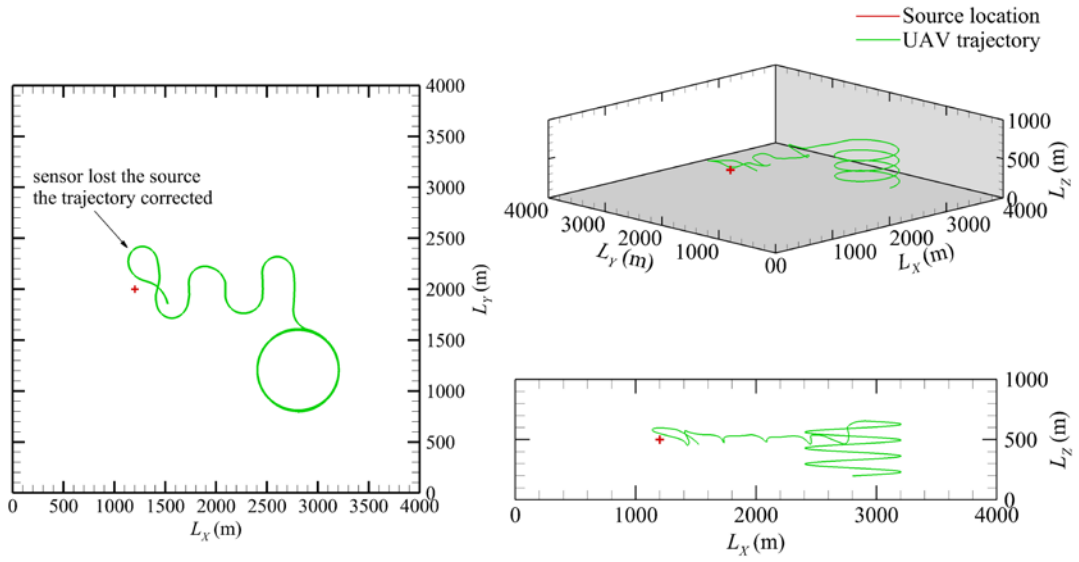

Figure 21. UAV trajectory for stationary source.

UAV, having no information about the source location and strength, starts patrolling the domain at a point with coordinates $\Theta_s(0) = (2.8\text{km}, 0.8\,\text{km}, 0.2\,\text{km})$, following a constant-climb orbit path with flight path angle $\gamma = 3^o$ and orbit radius equal to 0.4 km. After approximately 280 seconds of simulation, the sensor detects a nonzero concentration, which results in the activation of the estimation algorithm and thus switches the control of the UAV. Since a nonzero concentration is detected, the UAV receives the control signals resulted from the desired ground speed components (Eq. (2.58)), which guide the UAV towards areas of larger estimation error. In the case of continuous gas release with constant release rate, this area contains the source location. Figure 21 illustrates the resulting UAV path in horizontal plane, vertical plane, and in three-dimensional view. Because of the physical constraints imposed on the UAV motion and the presence of a strong wind from west to east, the UAV may leave the source`s proximity and detect zero concentration. If the sensor reads zero measurements after the estimator activation, the UAV is driven towards the point of maximum estimated concentration provided by Eq. (2.18). Figure 5 shows the resulting trajectory adjustment due to this condition in the source`s proximity.

The performance of the estimator is examined by calculating the RMS error of the estimated concentration vector. Although the source localization is not the primary goal of the present work, the fact that the guidance scheme moves the UAV towards the location of the

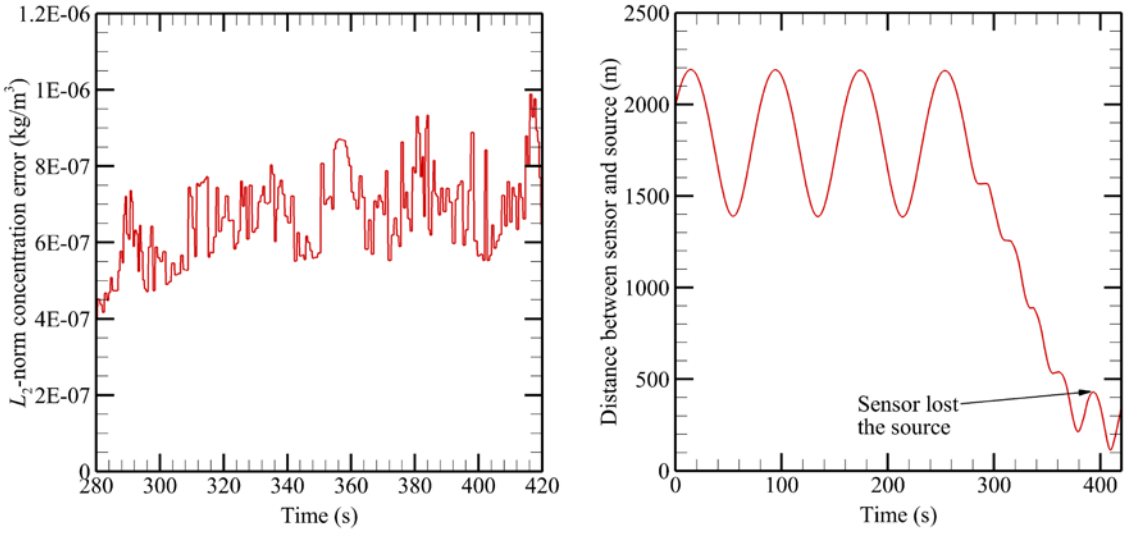

Figure 22. Estimator performance analysis for a stationary source. (Left) the RMS error vs. time; (right) distance between UAV and source.

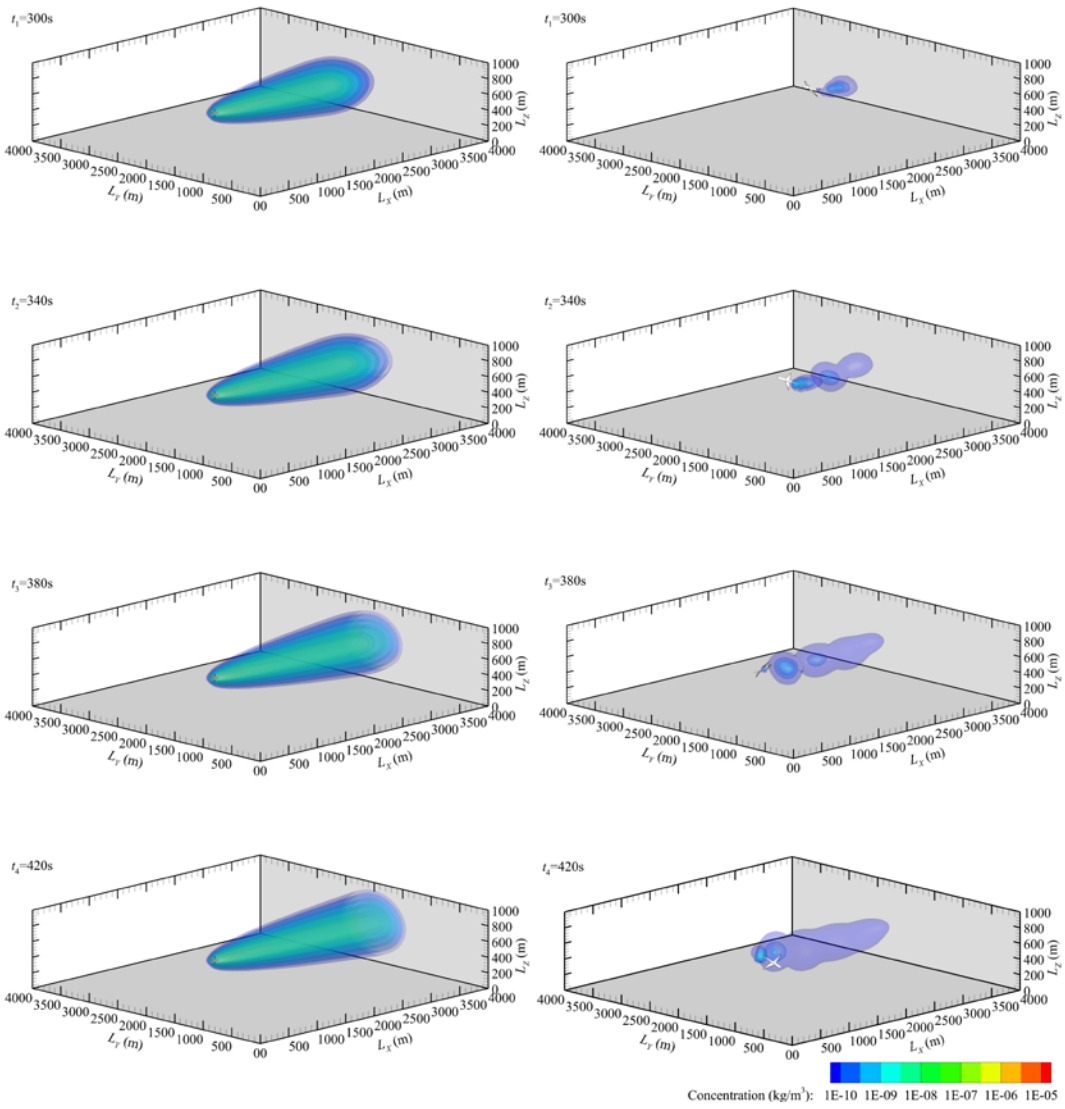

Figure 23. Comparison between estimated plume concentration (left) and simulated concentration (right) for a stationary aerial source at various times.

continuously-releasing source proves that the control signals indeed guide the sensor towards the area of larger estimation error. Therefore, every time the UAV sensor takes a measurement, the estimator provides a more accurate reconstruction of the gaseous plume. The RMS concentration error is shown in Figure 22 (left) as a function of time and the evolution of distance between the source and the UAV is shown in Figure 22 (right). Oscillations in the RMS error are due to the time that the UAV takes to reach the next desired location and the sensor time response. Spikes at the end of both plots in Figure 22 are due to the UAV looping in the source`s proximity.

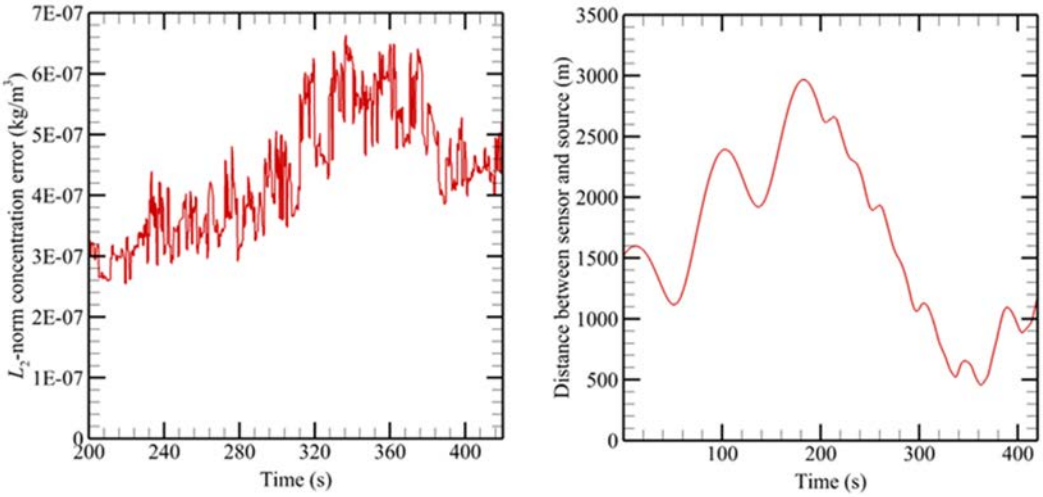

Figure 25. Estimator performance for a moving; (Left) RMS error vs. time; (Right) distance between the UAV and the source.

The estimated concentration of the gaseous plume is compared with the simulated data and presented in Figure 23 for different time instances. It is seen that by the end of the simulation time the shape of the estimated plume becomes closer to the shape of the "real" plume.

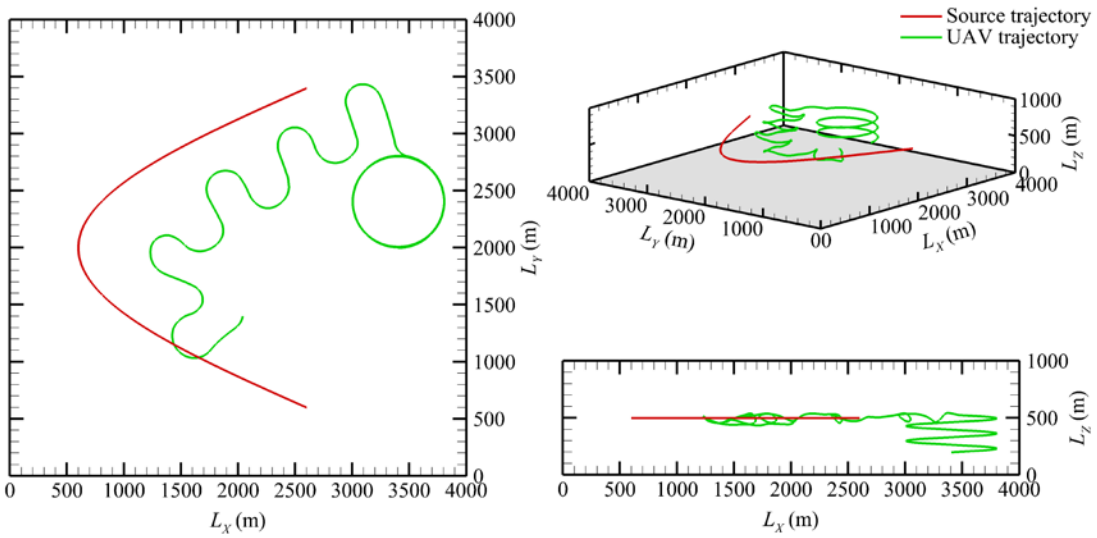

Figure 24. UAV trajectory for a source moving along an arc trajectory.

4.3.2 Source Moving along an Arc Trajectory

In this application, the gas source is moving along an arc trajectory maintaining a constant altitude with the rate of release $u = 1\ \mathrm{kg/s}$. The UAV starts patrolling the domain at a point with coordinates $\Theta_s\left(0\right) = \left(3.2\mathrm{km}, 2.0\,\mathrm{km}, 0.2\,\mathrm{km}\right)$ following the constant-climb orbit path with the flight path angle $\gamma = 3^{o}$ and the orbit radius equal to 0.4 km. The activation of the

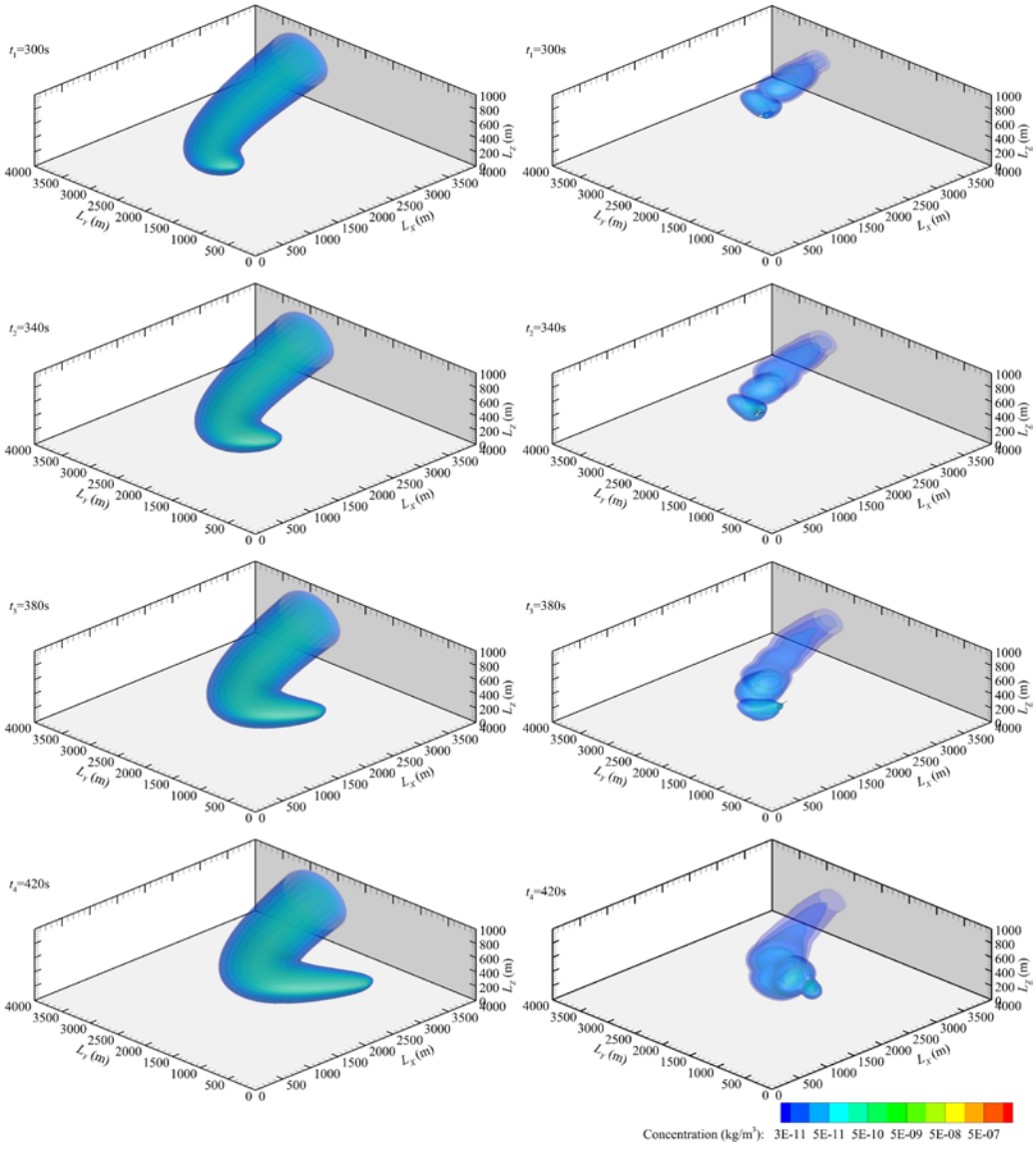

Figure 26. Comparison between estimated plume concentration (left) and simulated concentration (right) for a source moving along an arc trajectory.

estimator occurs after 190 seconds of simulation, when the sensor detects a nonzero concentration. The total simulation time is 420 seconds.

Figure 24 shows the resulting UAV trajectory. It is seen that the UAV is able to reproduce approximately the source`s trajectory. However, it stays at some distance to the east of the source, which is explained by the wind direction. The evolution of the RMS concentration error and the distance between the UAV and the source are shown in Figure 25. In this case, the UAV follows the source and after detecting a concentration with its sensor, the distance between the UAV and the source decreases until the end of the simulation process.

Figure 26 compares the estimated concentration of the gaseous plume to the simulated data (plant) at different time instances. Once again, it is observed that by the end of the simulation time the shape of the estimated plume becomes closer to the shape of the "real" plume.

4.3.3 Source Moving across the Domain with Altering Altitude

In this application, the gas source is moving across the domain, with its altitude changing as a sine function. The rate of release $u = 1\ \mathrm{kg/s}$. Unlike previously considered examples (where the wind speed was taken to be 7 m/s), the wind speed for this case is 9 m/s. The UAV starts patrolling the domain at a point with coordinates $\Theta_s\left(0\right) = \left(2.4\mathrm{km}, 2.8\,\mathrm{km}, 0.2\,\mathrm{km}\right)$

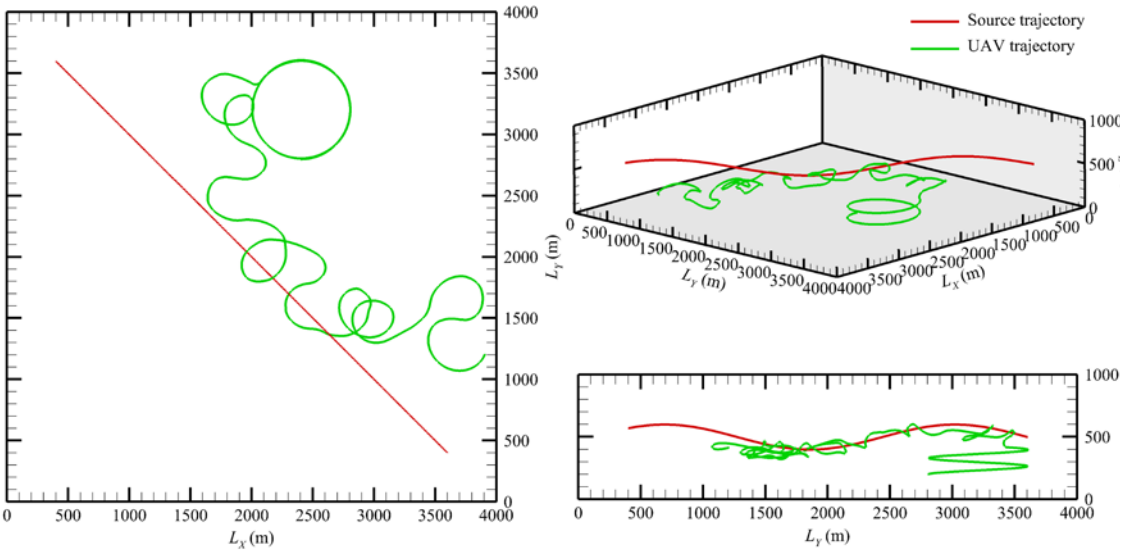

Figure 27. UAV trajectory for a source moving across the domain.

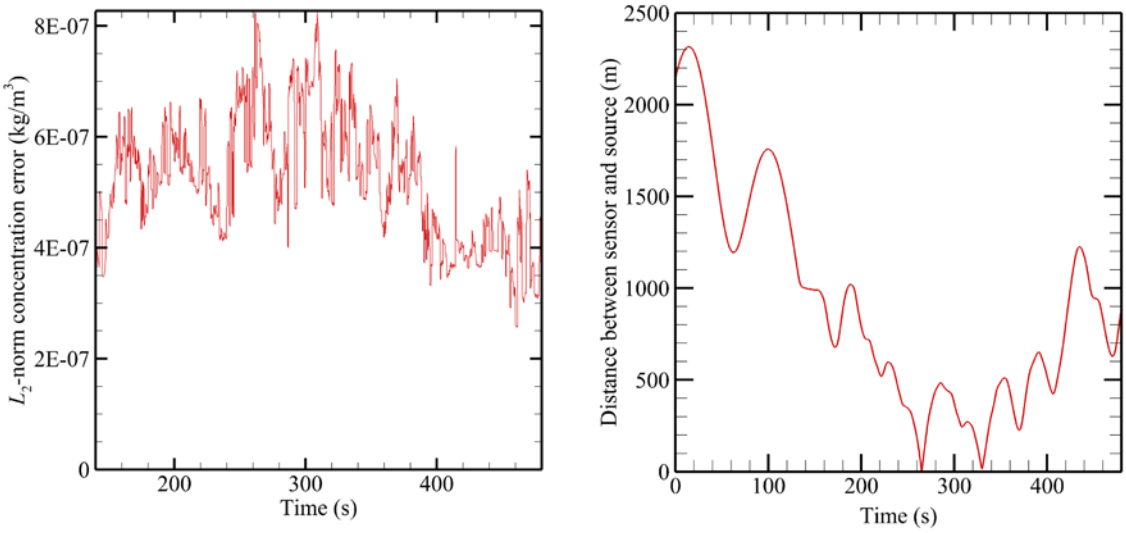

Figure 28. Estimator performance analysis for a source moving across the domain. (Left) the RMS error vs. time; (right) distance between UAV and source.

following the constant-climb orbit path with the flight path angle $\gamma = 3^{\circ}$ and the orbit radius equal to 0.4 km. It takes approximately 140 seconds for the sensor to detect a concentration above the threshold. The total simulation time in this case is 480 seconds.

Figure 27 shows the resulting UAV trajectory. The UAV is able to follow the source. However, at the end of the simulation time it tends to move upwind (recall that the wind speed is 9 m/s, whereas the Aerosonde® UAV cruise speed is about 30 m/s). The estimator performance analysis is presented in Figure 28. As time increases, the RMS error decreases, which is indicative of convergence of the proposed approach. For a couple of moments during the simulation time, the distance between the sensor and the source comes to zero. This requires additional algorithms for collision avoidance.

Figure 29 presents visualization of the "real" and estimated plumes for several time moments.

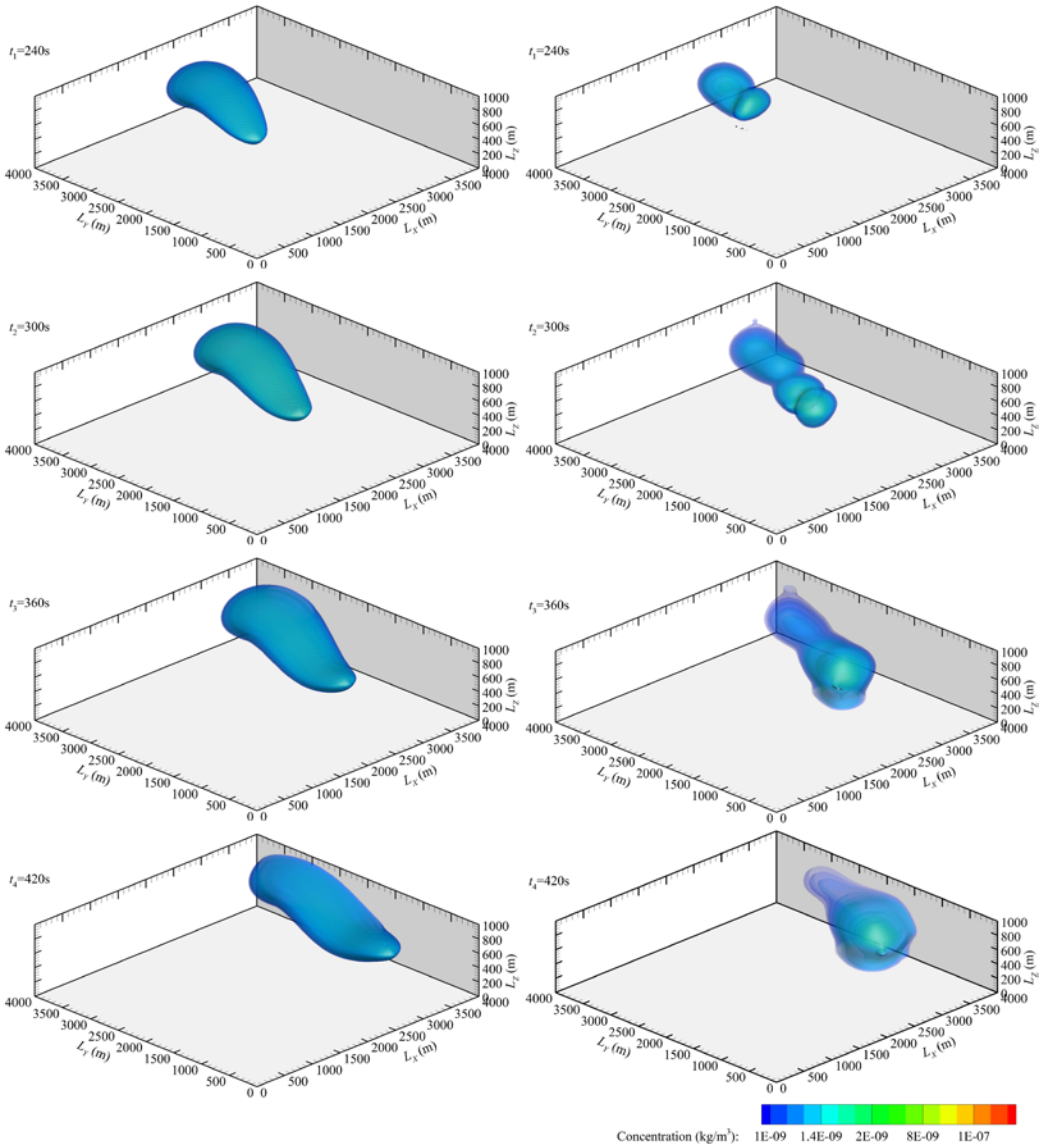

Figure 29. Comparison between estimated plume concentration (left) and simulated concentration (right) for a source moving across the domain.

4.3.4 Ground-Based Source

In this application the real-time prediction of gas contaminant concentration from a ground intruder using UAV is examined. In this case the computational domain considered has dimensions different from the other tested scenarios and equal to $3000\mathrm{m} \times 3000\mathrm{m} \times 600\mathrm{m}$. The wind speed is calculated according to Eq. (2.15) with $Z_r = 5\mathrm{m}$ and $m = 0.15$; $V = W = 0$. The estimator is approximated with $N = 30 \times 30 \times 40$ volumes, so that the

computational grid is adapted only in the X and Y directions and remains uniform in the Z direction. The minimum grid size in the adapted grid is $dl = 15$ m. The sensor is assumed to provide noiseless measurements with 1 second time response.

In the examined scenario, the intruder is moving across the domain from the North-West to the South-East corner, releasing gas with a rate of 1 kg/s. The UAV starts patrolling the domain downwind following a circular path of 400 m radius, at an altitude of 120 m. It takes approximately 190 seconds for the plume to reach the sensor. After that, the UAV receives the control signals to follow the desired Cartesian velocities (2.55). The UAV can fly as low as 10 m. If at any moment after the activation of the estimator, the sensor has a zero reading, it means that the UAV moved upwind and lost the plume. In this case, the guidance scheme is adjusted so that the sensor follows the maximum estimated concentration, thus returning to an area of nonzero concentration measurements. Figure 32 shows the resulting UAV trajectory. As it is seen, the UAV is moving towards the intruder with oscillations caused by the wind direction, the sensor time response, and the time required for the UAV to complete a maneuver. The loops in the trajectory are due to the fact that the sensor leaves the plume moving upwind and it takes several time iterations to return it back to the source's proximity.

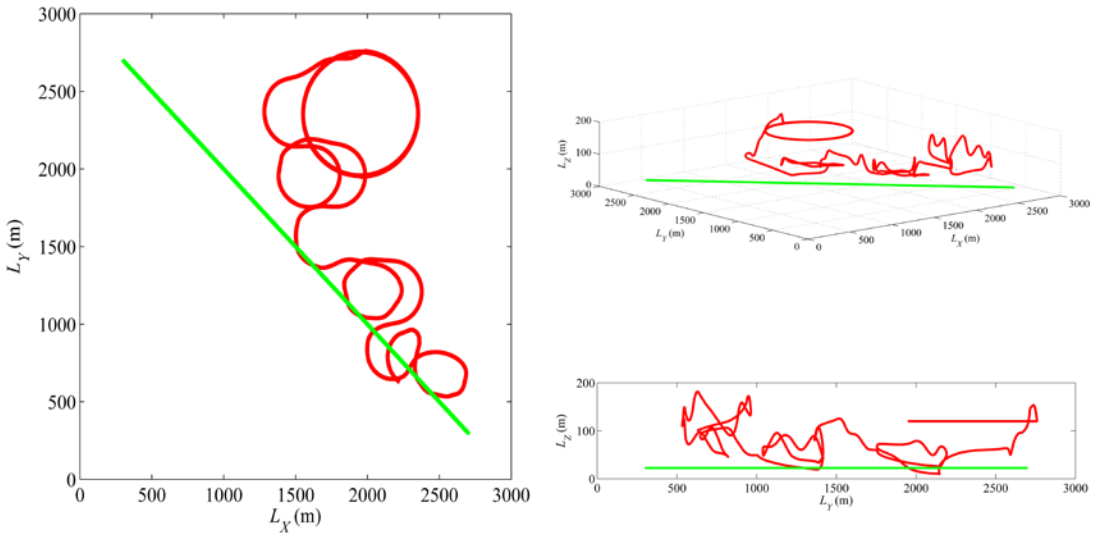

Figure 30. UAV trajectory: red line – UAV path; green line – intruder.

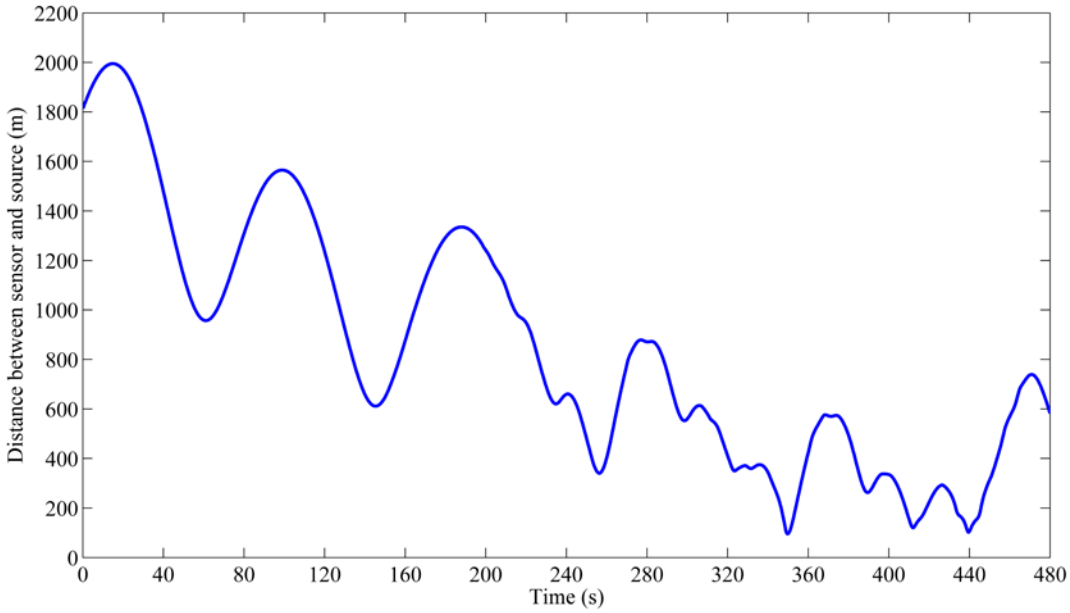

Figure 31. Distance between the sensor and the source vs. time.

The estimator performance is quantified by the behavior of the normalized RMS error, which measures the difference between the estimated and true concentration field, and the distance between the sensor and the intruder. Figure 32 shows the normalized RMS error as a function of time. As it is observed, the RMS drops rapidly after the estimator activation and

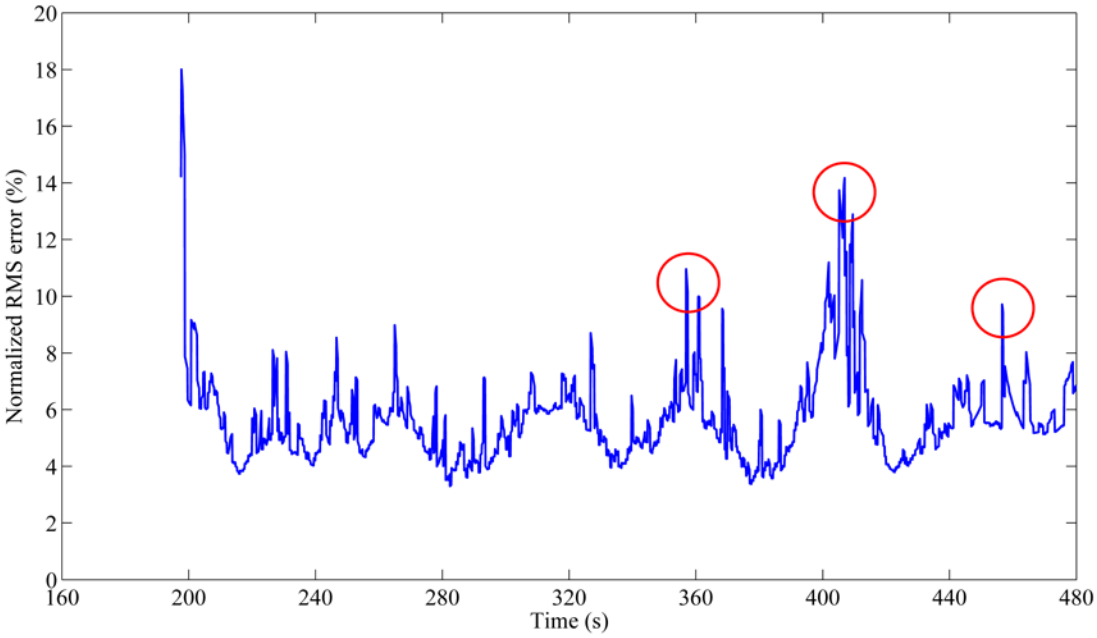

Figure 32. Normalized root-mean-square error vs. time.

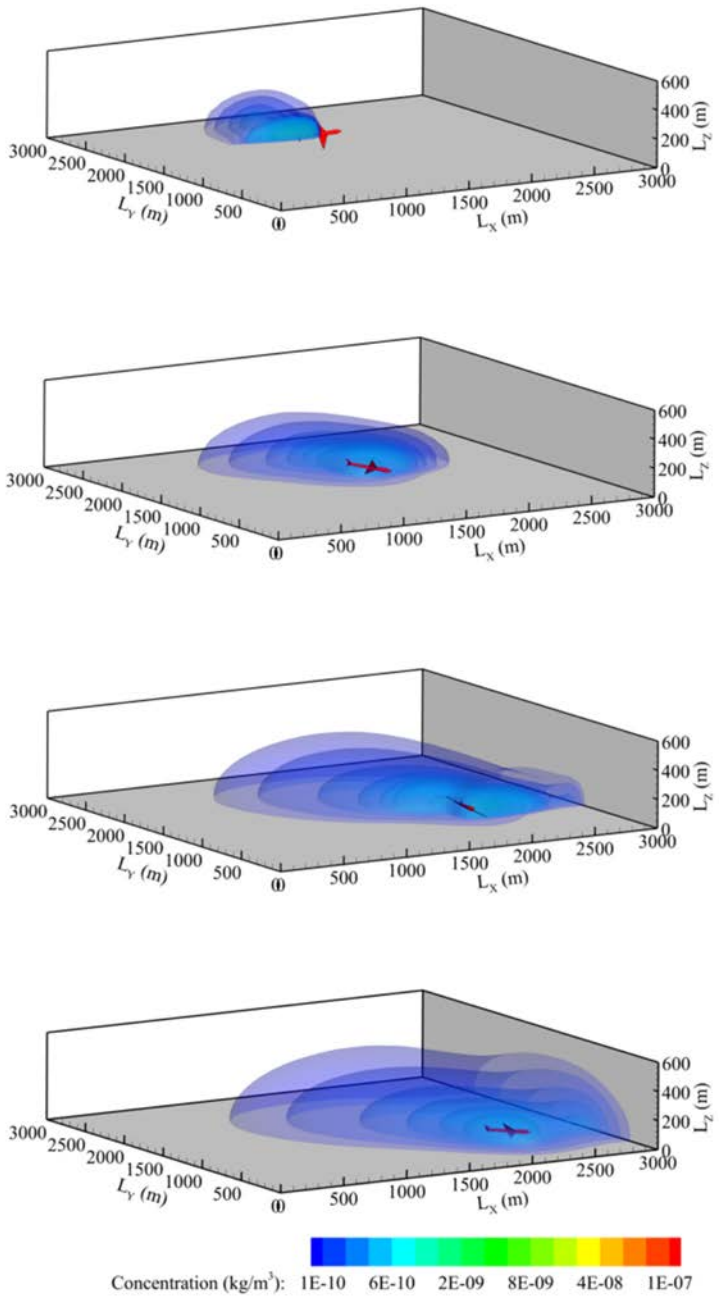

Figure 33. Evolution of the estimated plume from 240s to 480s with 80s increments.

stays on average within 10%. The oscillations are due to the fact that the source is releasing material continuously. The spikes around 360s, 400s and 460s are explained by the fact that the UAV looses the source's proximity, and it takes several seconds for it to relocate the plume. Figure 31 shows the distance between the sensor and the source as a function of time. It is seen

that the sensor approaches the gaseous source, which proves that the proposed guidance scheme indeed moves the UAV towards the larger estimation error that coincides with the source location in the case of continuous release.

Figure 33 shows the real-time estimates of gas concentration from a ground mobile source.

4.4 Multiple Sensors

For the "practical" application of the suggested estimation approach the concentration gradients are estimated using multiple sensor readings. In Section 2.4.6 we suggest to take advantage of the additional measurements and to include them into the estimator (2.18). The performance of the estimation algorithm is tested numerically for this case. The sensors are assumed to be attached to different UAVs that maintain a rigid formation during the whole simulation time. The distance dl between the leader UAV and a follower is equal in all the directions X, Y, and Z, and is dictated by the numerical resolution of the process model equation (2.13). However, in a real life situation, such parameter would be chosen based on the advection length-scale $\sigma_a = Ut$ and diffusion length-scale $\sigma_d = \sqrt{Kt}$ in order to give the meaningful gradient.

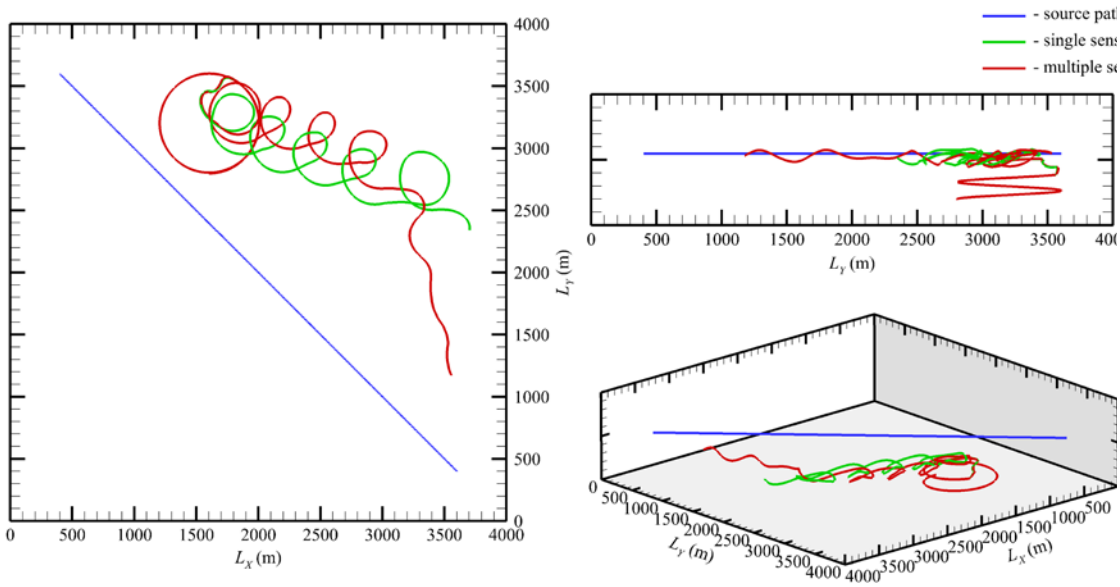

Figure 34. Comparison of the trajectory in case of the concentration estimation with a single sensor and with multiple sensors.

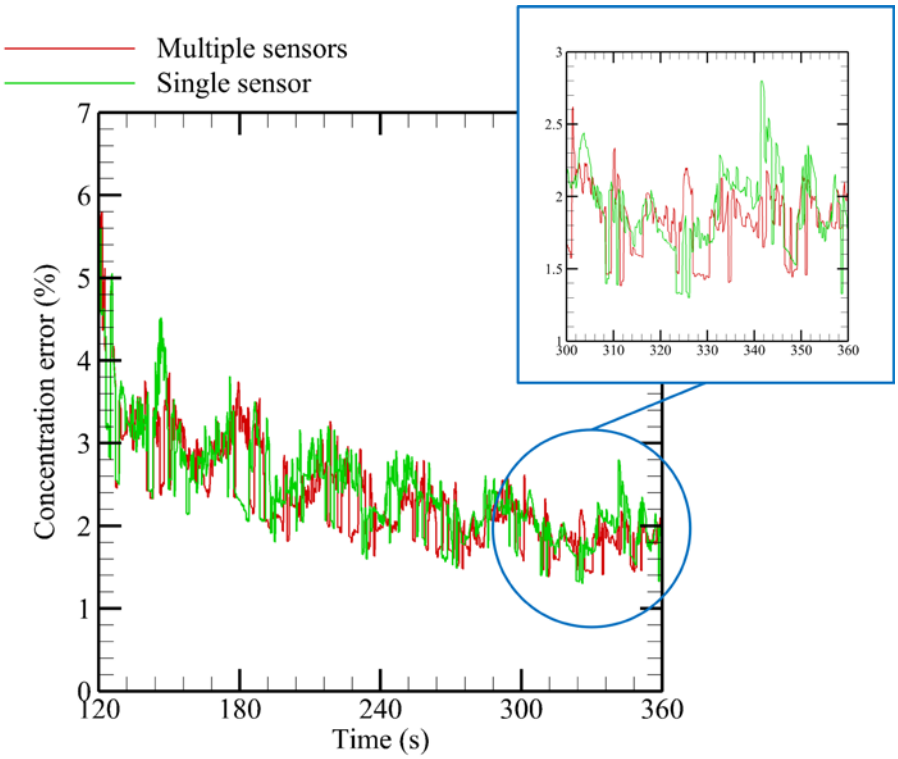

Figure 35. The normalized concentration error versus time for the case of a single sensor and the case of multiple sensors.

In the first considered case the source is moving across the domain. The wind speed is 9 m/s, the total simulation time is 360 seconds. The results are shown in comparison with the single sensor case, provided that a single sensor has full knowledge of concentration and concentration gradients at its location.

Figure 34 shows the resulting trajectory for a single sensor and the sensor formation. In the first case, the trajectory results from the guidance scheme (2.55), and in the second case it results from Eq. (2.67) with constant Γ's. It is seen that the flying formation is more successful in chasing the source by the end of the simulation time. The corresponding distance between the sensor and the source is shown in Figure 36.

The concentration error normalized by the total amount of material released is shown in Figure 35. Specifically, the last minute of the simulation is zoomed in order to clearly show the oscillations. It is seen that the oscillations are smaller in case of multiple sensors.

Another example is considered for application of the multiple sensors. In this case, the source is moving along an arc trajectory, similar to Section 4.3.2. The simulation time in this case is 420 seconds. The trajectory and the corresponding distance between the sensor and

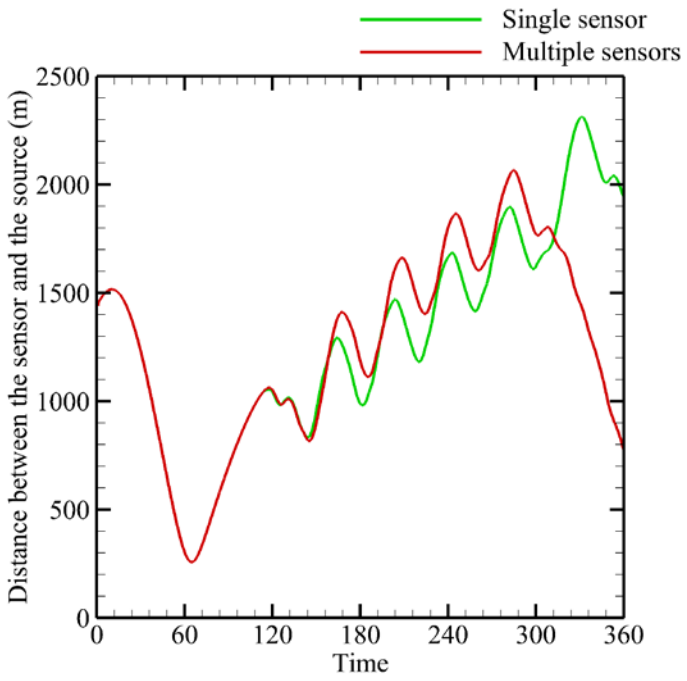

Figure 36. The distance between the sensor and source versus time for the case of a single sensor and the case of multiple sensors.

source for this case is shown in Figure 38 and Figure 37 accordingly. Similar to the previous example, the flight formation improves the estimation approach by the end of the simulation time as compared to a single sensor.

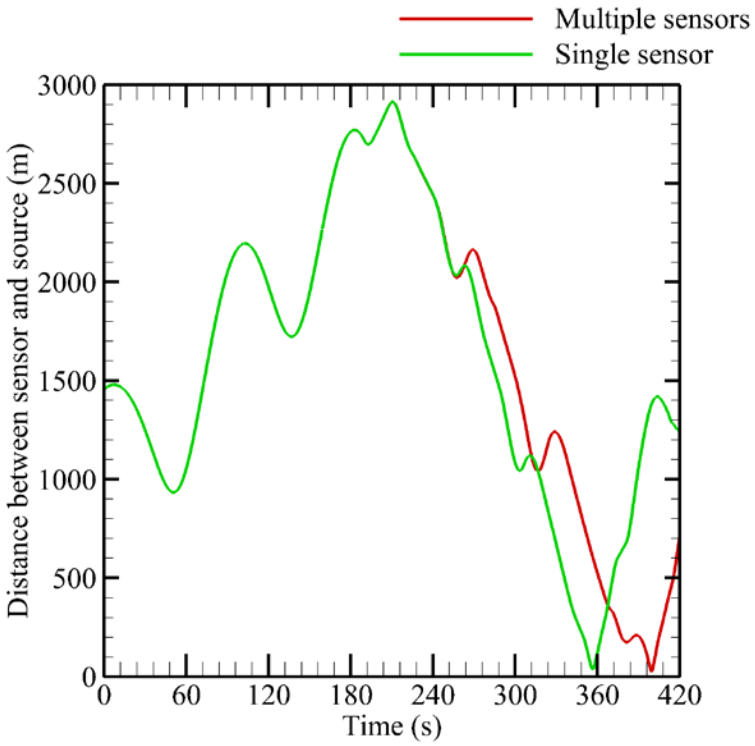

Figure 37. The distance between the sensor and source versus time for the case of a single sensor and the case of multiple sensors; the source is moving along an arc trajectory.

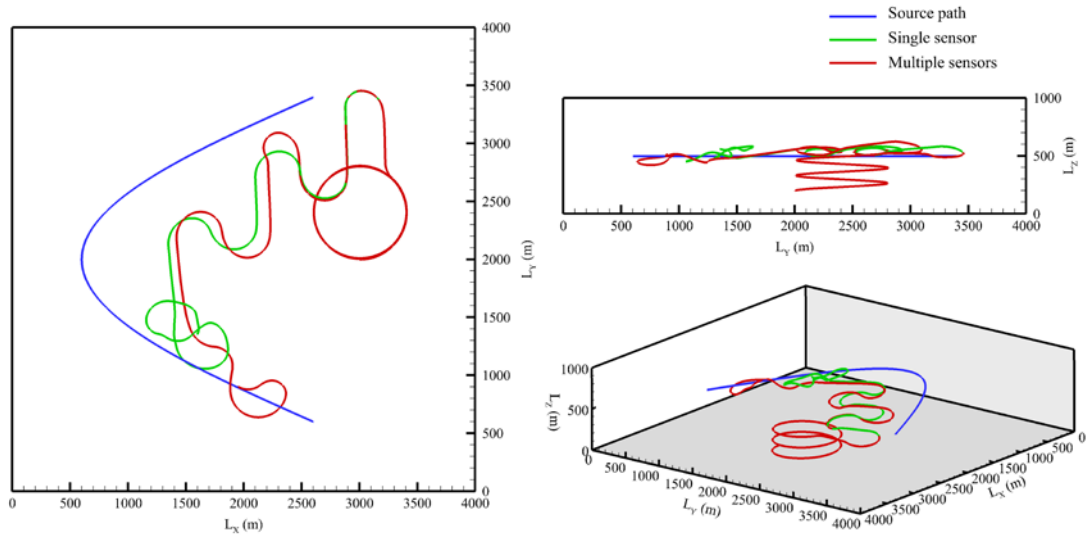

Figure 38. Comparison of the trajectory in case of the concentration estimation with a single sensor and with multiple sensors; the source is moving along an arc trajectory.

Chapter 5. Summary, Conclusions and Recommendations for Future Work

5.1 Summary

This dissertation expanded the earlier work [18], [19], [20], [21], [22], [23], [24], [25] on a coupled CFD-control approach that provides the real-time estimate of a gaseous plume in the atmosphere presented by an UAV equipped with sensors. These developments involve the mathematical model, the computational model and the applications, and have been presented also in [39], [40], [41], [42]. The mathematical model for the process of gas release was extended to a 3D unsteady advection-diffusion equation and it was implemented numerically using a finite volume method. The numerical implementation was supplemented with a total variation diminishing scheme for the advection term. The numerical code created in Fortran 90 considers different source trajectories and release types (pulsed or continuous), and different models for winds and eddy diffusivities. The sensor model was expanded to a 3D case and implemented given a specific response time and sensitivity range. A 3D dynamical model for the UAV was developed and implemented in the code. The guidance law based on the Lyapunov redesign methods was modified in such a way, that the Lyapunov function resulted in the desired direction for the vehicle. A lower-level controller in turn provided the UAV with the inputs that a pilot commonly controls: thrust, lift, and bank angle. For the purpose of numerical efficiency in the real-time tracking problem, the algorithm for the computational grid adaptation was developed. According to this algorithm, the computational grid is adapted continuously, thus keeping an area of high resolution near the sensor. The desired direction, namely Cartesian velocity components for the UAV, was expressed in terms of the concentration error gradient. The concentration error gradient was calculated using multiple concentration sensors, which were assumed to be attached to different vehicles that maintain a rigid flying formation around a leader-UAV. The measurements from additional sensors were included in a 3D estimator model via the use of the observation operator given by the 7-dimensional vector. The approach was tested as applied to different source trajectories using physical parameters of the Aerosonde® UAV. The applications included detection of a ground-

based intruder, and an aerial source. In addition, the case of a flying formation for estimation of the concentration plume as well as the source proximity was examined.

Figure 39 shows the main steps of the approach implementation. The plume is assumed to be generated by a moving aerial source with unknown strength and location, and is modeled by the unsteady advection-diffusion equation with winds and eddy diffusivities. The UAV equipped with concentration sensors patrols the domain and collects sensor readings. As soon as the sensor reads the data above a certain threshold, the estimator is activated. The estimated concentration results from the numerical solution of the advection-diffusion equation supplemented with the concentration sensor readings. The approach couples the UAV guidance with the performance of the estimator through the state (concentration) estimation error. Via the appropriate choice of the Lyapunov function for the resulting state estimation error the estimation scheme provides the desired Cartesian velocities of the UAV. A lower-level controller in turn accepts these desired velocities as reference inputs and provides the control signals to the UAV in order to follow the desired velocities. As a result, the UAV moves towards the areas with the maximum estimation error. The finite-volume discretization of the estimator incorporates a second-order total variation diminishing scheme (TVD) for the

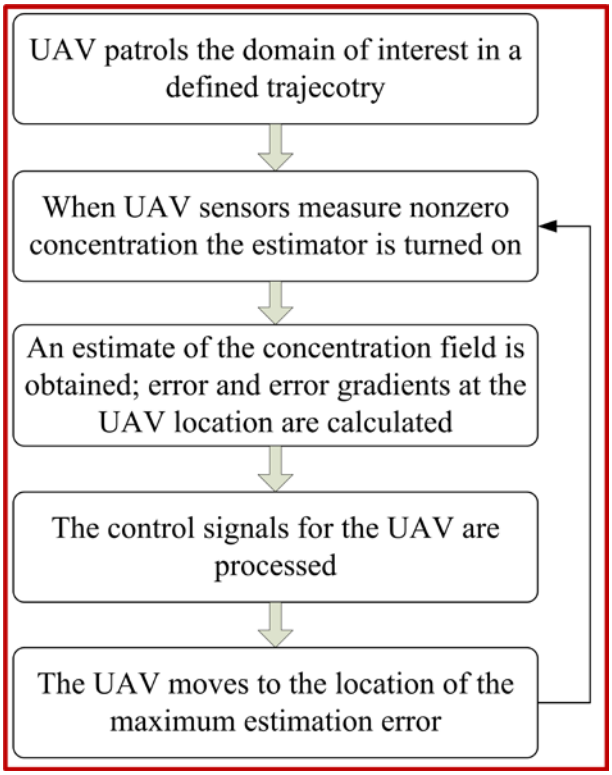

Figure 39.Flow chart of the approach.

advection term. To achieve greater computational efficiency, the computational grid for the estimator is adapted dynamically with local grid-refinement centered at the UAV location.

5.2 Conclusions

The mathematical model for the advection-diffusion equation, for the point-sensor measurements, as well as for the Luenberger observer estimator was expanded to a 3D case. The 3D dynamical model was developed for the UAV. The guidance law for the UAV was modified in order to provide the control inputs in terms of the values that a pilot commonly controls: engine thrust, lift, and bank angle. The gradient measurement issue was addressed by using multiple sensors. The estimator was modified to include multiple sensor readings. Numerically, the discretization of the advection-diffusion equation was improved by adding total variation diminishing scheme for the advection term. In addition, the equation was solved using more sophisticated computational grid adaptation approach. The computational grid was adapted continuously during the simulation time to provide higher resolution near the sensor location. The 3D UAV dynamical model was implemented numerically, and the aircraft response to the control inputs based on the estimator performance was visualized. The approach was tested using physical parameters of the Aerosonde® UAV for different source trajectories and atmospheric conditions. As part of the project, the approach was applied to a realistic scenario of a ground-based intruder. Finally, the approach was tested using additional sensor readings meant for calculation of the concentration gradient in the estimator.

5.3 Recommendations for Future Work

The following discussion presents potential directions for future work.

- The simulation studies presented in this work were implemented using realistic sensor characteristics, such as sensitivity and time response. However, an important assumption of noiseless sensor readings was made. Further improvement of the approach implies the inclusion of the sensor noise. One may view a matrix Γ in Eq. (2.63) as a version of this, if one assumes that the filter covariance operator (or matrix) is identity, and then Γ becomes the sensor noise covariance.

- The simulation results were obtained taking into account the sensor response time. As a part of the future work, the sensor time response should be included in the mathematical model.
- Another possible direction for the future work is the modification of the estimator model. One may consider using a Kalman-based estimator instead of a Luenberger observer design.
- The UAV flight visualization shows some erratic motion, which is due to the fact that the UAV receives the new control signal every time the new measurements are taken. This means that every 1.5-2 seconds the new control signals are generated. At that, the new desired direction may be opposite to the previous one, which causes the UAV to turn around as fast as possible. The implemented visualization smoothens these turns by imposing constraints on the rotation rates of the UAV. In future work, a more sophisticated filtering algorithm may be suggested for this problem.
- The distance dl between the leader UAV and a follower used to calculate the concentration gradient can be altered throughout the process to account for the changes in the wind speed. For this reason, a guidance model for a flying formation should be developed.
- Since the ultimate goal of this work is to develop the approach for the real-time gaseous plume estimation for the real world applications, such as detection of intruder or identification of the hazardous leakages, the future work should be aimed at setting up the experimental setup to test the approach proposed in this work. At first it can be implemented in enclosure using a ground-based robot with several concentration sensors attached to it. An open-air experiment that involves unmanned aerial vehicle would be the final step in this work.

Bibliography

[1] Kibler, J. F., and Suttles, J. T., "Air pollution model parameter estimation using simulated LIDAR data." *AIAA Journal*, 1977, Vol. 15, No. 10, pp. 1381-1384.

[2] Hogan, W. R., Cooper, G. F., Wagner, M. M., and Wallstrom, G. L., "An inverted Gaussian plume model for estimating the location and amount of release of airborne agents from downwind atmospheric concentrations," *Pittsburgh, PA: RODS Laboratory Technical Report*, 2005.

[3] Fox, E. B., Fisher, J. W., and Willsky, A. S., "Detection and localization of material releases with sparse sensor configurations," *IEEE Transactions on Signal Processing*, 2007, Vol. 55, No. 5, pp. 1886-1898.

[4] Zhao, T., and Nehorai, A., "Distributed sequential Bayesian estimation of a diffusive source in wireless sensor networks," *IEEE Transactions on Signal Processing*, 2007, Vol 55, No. 4, pp. 1511-1524.

[5] Porat, B., and Nehorai, A., "Localizing vapor-emitting sources by moving sensors," *IEEE Transactions on Signal Processing*, 1996, Vol. 44, No. 4, pp. 1018-1021.

[6] Tzanos, P., and Zefran, M., "Locating a circular biochemical source: Modeling and control," *IEEE International Conference on Robotics and Automation*, 2007.

[7] Fukazawa, Y., and Ishida, H., "Estimating gas-source location in outdoor environment using mobile robot equipped with gas sensors and anemometer," *IEEE Sensors*, 2009.

[8] Lilienthal, A. J., Reggente, M., Trincavelli, M., Blanco, J., and Gonzalez, J., "A statistical approach to gas distribution modelling with mobile robots-the kernel dm+ v algorithm," *IROS 2009*, *IEEE/RSJ International Conference on Intelligent Robots and Systems*, 2009, pp. 570-576.

[9] Hernandez, B. V., Schaffernicht, E., Pomareda, V., Lilienthal, A. J., Marco, S., and Trincavelli, M., "Combining Non Selective Gas Sensors on a Mobile Robot for

Identification and Mapping of Multiple Chemical Compounds," *IEEE Sensors*, 2014, Vol. 14, No. 9, pp. 17331-17352.

[10] Pisano, W. J., and Lawrence, D. A., "Data Dependant Motion Planning for UAV Plume Localization," *Proceedings of the AIAA Guidance, Navigation and Control Conference*, 20-23 August 2007, South Carolina.

[11] Kuroki, Y., Young, G. S., and Haupt, S. E., "UAV navigation by an expert system for contaminant mapping with a genetic algorithm." *Expert Systems with Applications*, 2010, Vol. 37, No. 6, pp. 4687-4697.

[12] Bays, M. J., and Kochersberger K. B., "Tracking of a Plume Source using a priori Models and Nonlinear Filtering," *Proceedings of the AIAA Infotech@ Aerospace*, 20-22 April 2010, Atlanta, Georgia.

[13] Towler, J., Krawiec, B., and Kochersberger, K., "Radiation Mapping in Post-Disaster Environments Using an Autonomous Helicopter," *Remote Sensing*, 2012, Vol. 4, No. 7, pp. 1995-2015.

[14] Neumann, P. P., Hernandez, B. V., Lilienthal, A. J., Bartholmai, M., and Schiller, J. H., "Gas source localization with a micro-drone using bio-inspired and particle filter-based algorithms," *Advanced Robotics*, 2013, Vol. 27, No. 9, pp. 725-738.

[15] Neumann, P. P., Schnürmacher, M., Bennetts, V. H., Lilienthal, A. J., Bartholmai, M., and Schiller, J. H., "A Probabilistic Gas Patch Path Prediction Approach for Airborne Gas Source Localization in Non-Uniform Wind Fields," *Sensor Letters*, 2014, Vol. 12, No. 6-7, pp. 1113-1118.

[16] Apker, T. B., and Potter, M. A., "An artificial physics approach to plume detection with fixed wing UAVs," *Proceedings of the AIAA Guidance, Navigation and Control Conference*, 2011.

[17] Šmídl, V., and Hofman, R., "Tracking of atmospheric release of pollution using unmanned aerial vehicles," *Atmospheric Environment*, 67, 2013, pp. 425-436.

[18] Demetriou, M. A., and Gatsonis, N. A., "Scheduling of static sensor networks and management of mobile sensor networks for the detection and containment of moving sources in spatially distributed processes," *Proceedings of the 17th Mediterranean Conference on Control and Automation, IEEE*, 2009, pp. 187-192.

[19] Demetriou, M. A., Gatsonis, N. A., and Court, J. R., "Model-based detection of a moving gaseous source in a 2D spatial domain using a sensor-based grid adaptation approach," *Proceedings of the American Control Conference, IEEE*, 2011 pp. 2374-2380.

[20] Demetriou, M., Gatsonis, N., and Court, J. R., "Numerical investigation of the spatial estimation error in sensor guidance used for the localization of a gaseous source in a 2D domain," *Proceedings of the 19th Mediterranean Conference on Control and Automation, IEEE*, 2011, pp. 1386-1391.

[21] Demetriou, M., Gatsonis, N., and Court, J. R., "Lyapunov based guidance of a mobile sensing agent for state estimation of a gaseous source in a 3D spatial domain," *Proceedings of the 50th European Control Conference in Decision and Control, IEEE*, 2011, pp. 1986-1992.

[22] Court, J. R., Demetriou, M. A., and Gatsonis, N. A., "Spatial gradient measurement through length scale estimation for the tracking of a gaseous source," *Proceedings of the American Control Conference, IEEE*, 2012, pp. 2984-2989.

[23] Demetriou, M., Gatsonis, N., and Court, J. R., "Numerical studies of concentration estimation and source tracking of a gaseous source using multiple mobile distributed sensors," *Proceedings of the 20th Mediterranean Conference on Control and Automation, IEEE*, 2012, pp. 1055-1060.

[24] Court, J. R., (2012). Estimation of the Concentration from a Moving Gaseous Source in the Atmosphere Using a Guided Sensing Aerial Vehicle (Doctoral dissertation), retrieved from Electronic Theses and Dissertations, WPI.

[25] Demetriou, M. A., Gatsonis, N. A., and Court, J. R., "Coupled Controls-Computational Fluids Approach for the Estimation of the Concentration from a Moving Gaseous Source in a 2-D Domain with a Lyapunov-Guided Sensing Aerial Vehicle," *IEEE Transactions on Control Systems Technology*, Vol. 22, No. 3, pp. 853-867, 2014.

[26] Butkovskii, A. G., Darinskii, Y. V., and Pustyl'nikov, L. M., "Control of distributed systems by displacement of the source," Automatika i Telemekhanika (5), 11, 1974.

[27] Butkovskii, A. G., "Theory of mobile control," *Automation and Remote Control*, 40(6), pp. 804-813, 1979.

[28] Butkovskii, A. G., Ibragimov, S. I., and Chubarov, E. P., "Control of distributed systems by changing the shape of the source," *Automation and Remote Control*, 40(12), pp. 1719-1728, 1979.

[29] Butkovskii, A. G.; Pustyl′nikov, L. M. *Теория подвижного управления системами с распределенными параметрами* (Russian) [*Theory of moving control of systems with distributed parameters*], Теоретические Основы Технической Кибернетики. [Series in Theoretical Foundations of Engineering Cybernetics], Nauka, Moscow, 1980. 384 pages

[30] Butkovskii, A. G., Pustylnikova, E., "Theory of mobile control of distributed parameter-systems,". *Automation and Remote Control*, 41(6), pp. 741-747, 1980.

[31] Rafajłowicz, E., "Optimum choice of moving sensor trajectories for distributed-parameter system identification," *International Journal of Control*, 43(5), pp. 1441-1451, 1986.

[32] Uciński, D., "Sensor network scheduling for identification of spatially distributed processes," *International Journal of Applied Mathematics and Computer Science*, 22(1), pp. 25-40, 2012.

[33] Uciński, D., "An optimal scanning sensor activation policy for parameter estimation of distributed systems," *Model Based Parameter Estimation*, pp. 89-124, *Springer Berlin Heidelberg*, 2013.

[34] Uciński, D., Korbicz, J., "Optimal sensor allocation for parameter estimation in distributed systems," *Journal of Inverse and Ill-Posed Problems*, 9(3), pp. 301-318, 2001.

[35] Ucinski, D., *Optimal measurement methods for distributed parameter system identification*. CRC Press, 2004.

[36] Demetriou, M.A.; Ucinski, D., "State estimation of spatially distributed processes using mobile sensing agents," *Proceedings of the 2011 American Control Conference*, June 29-July 1 2011, pp. 1770 – 1776.

[37] Burns, J.A.; Cliff, E.M.; and Rautenberg, C., "A distributed parameter control approach to optimal filtering and smoothing with mobile sensor networks,"

Proceedings of the 17th Mediterranean Conference on Control and Automation, Thessaloniki, Greece, pp. 181 – 186, 24-26 June 2009.

[38] Burns, J. A. Rautenberg, C. N., "The infinite-dimensional optimal filtering problem with mobile and stationary sensor networks," *Numerical Functional Analysis and Optimization*, 36(2), pp. 181–224, 2015.

[39] Egorova, T., Gatsonis, N. A., Demetriou, M. A., "Estimation of Gas Concentration from a Moving Source with an Unmanned Aerial Vehicle", *submitted to Journal of Guidance, Control, and Dynamics.*

[40] Gatsonis, N. A., Demetriou, M. A., and Egorova, T., "A controls-CFD approach for estimation of concentration from a moving aerial source: Comparisons between switched and dynamically adapted grids in 2D," *Proceedings of the 21th Mediterranean Conference on Control and Automation, IEEE*, 2013, pp. 1029-1034.

[41] Gatsonis, N. A., Demetriou, M. A., Egorova, T., "Real-time Prediction of Gas Contaminant Concentration from a Ground Intruder using a UAV," *Proceedings of the IEEE Conference on Technologies for Homeland Security*, April 2015.

[42] Egorova, T., Demetriou, M. A., Gatsonis, N. A., "Estimation of a gaseous release into the atmosphere using an unmanned aerial vehicle," *Proceedings of the European Control Conference*, IEEE, July 2015.

[43] Watts, A. C., Ambrosia, V. G., and Hinkley, E. A., "Unmanned aircraft systems in remote sensing and scientific research: Classification and considerations of use," *Remote Sensing*, Vol. 4, No. 6, pp. 1671-1692, 2012.

[44] Austin, R., *Unmanned aircraft systems: UAVS design, development and deployment.* Vol. 54, John Wiley & Sons, 2011.

[45] Maslankik, J. "Polar remote sensing using an unpiloted aerial vehicle (UAV)," *Seminar, ATOC7500*, November. 2002.

[46] Rodi, W., *Turbulent buoyant jets and plumes*. Vol. 3. New York: Pergamon press, 1982.

[47] Davies, P. A., and Valente Neves, M. J. *Recent research advances in the fluid mechanics of turbulent jets and plumes*. Vol. 255, Springer, 1994.

[48] Seinfeld, J. H., and Pandis, S. N., *Atmospheric Chemistry and Physics: from Air Pollution to Climate Change*, John Wiley & Sons, Hoboken, NJ, 2012.

[49] Arya, S. P., *Air Pollution Meteorology and Dispersion*, Oxford University Press, New York, 1999.

[50] Stockie, J. M., "The mathematics of atmospheric dispersion modeling. *Siam Review*, Vol. 53(2), pp. 349-372, 2011.

[51] Somlyai, L., Turóczi, A., and Molnár, A., "Atmospheric analyser for mobile robots," 2012 IEEE 13th International Symposium on Computational Intelligence and Informatics (CINTI), pp. 181-185. IEEE, 2012.

[52] Liu, X., Cheng, S., Liu, H., Hu, S., Zhang, D., and Ning, H., "A survey on gas sensing technology," *Sensors*, Vol. 12(7), pp. 9635-9665, 2012.

[53] Beard, J., et al. "Mobile phone based drifting lagrangian flow sensors," 2012 IEEE 3rd International Conference on Networked Embedded Systems for Every Application (NESEA), IEEE, 2012.

[54] Bennett, A., *Lagrangian Fluid Dynamics*, Cambridge University Press, New York, 2006.

[55] Fiorelli, E., et al. "Multi-AUV control and adaptive sampling in Monterey Bay." *IEEE Journal of Oceanic Engineering*, Vol. 31(4), pp. 935-948, 2006.

[56] Beard, R. W., and McLain, T. W., *Small unmanned aircraft: Theory and practice*. Princeton University Press, 2012.

[57] Phillips, W. F., *Mechanics of flight*. John Wiley & Sons, 2004.

[58] Napolitano, M. R., *Aircraft Dynamics*. Wiley, 2011.

[59] Anderson, J. D. *Introduction to flight*. Vol. 199. Boston: McGraw-Hill, 2005.

[60] Zhao, Y., and Tsiotras, P., "Time-optimal path following for fixed-wing aircraft," *Journal of Guidance, Control, and Dynamics*, Vol. 36(1), pp. 83-95, AIAA, 2012

[61] Menon, P. K., Vaddi, S. S., and Sengupta, P., "Robust landing guidance law for impaired aircraft," *Journal of Guidance, Control, and Dynamics*, Vol. 35(6), pp. 1865-1877, AIAA, 2012.

[62] Williams, P. "Three-dimensional aircraft terrain-following via real-time optimal control," *Journal of Guidance, Control, and Dynamics*, Vol. 30(4), pp. 1201-1206, 2007.

[63] Demetriou, M. A., "Guidance of Mobile Actuator-plus-Sensor Networks for Improved Control and Estimation of Distributed Parameter Systems," *IEEE Transactions on Automatic Control*, vol. 55(7), pp. 1570-1584, IEEE, 2010.

[64] Hirsh, C., *Numerical Computation of Internal and External Flows: the Fundamentals of Computational Fluid Dynamics*, Butterworth-Heinemann, Burlington, MA, 2007.

[65] Hirsh, C., *Numerical Computation of Internal and External Flows. Volume 1: Fundamentals of Numerical Discretization*, Vrije Universiteit Brussel, Brussels, Belgium.

[66] Versteeg, H. K., and Malalasekera, W., *An Introduction to Computational Fluid Dynamics: the Finite Volume Method*, Pearson Education, Harlow, UK, 2007.

[67] Thuburn, J., "TVD Schemes, Positive Schemes, and the Universal Limiter," *Monthly weather review*, 1997, Vol. 125, No. 8, American Meteorological Society (AMS).

[68] Kurganov, A., and Tadmor, E., "New High-resolution Central Schemes for Nonlinear Conservation Laws and Convection-Diffusion Equations," *Journal of Computational Physics*, 2000, Vol. 160, No. 1, Elsevier, pp. 241-282.

[69] Thompson, J. F., Warsi, Z. U., and Mastin, C. W., *Numerical Grid Generation: Foundations and Applications*, North-Holland, Amsterdam, 1985.

[70] Keyes, D. A., Ecer, N., Satofuka, P. F., and Periaux, J., *Parallel Computational Fluid Dynamics' 99: Towards Teraflops, Optimization and Novel Formulations*, Elsevier, Amsterdam, Netherlands, 2000.

[71] Manzini, G., and Russo, A., "A Finite Volume Method for Advection-Diffusion Problems in Convection-Dominated Regimes," *Computer Methods in Applied Mechanics and Engineering*, 2008, Vol. 197, No. 13, Elsevier, pp. 1242-1261.

[72] Roy, J., "Grid Convergence Error Analysis for Mixed-Order Numerical Schemes," *AIAA Journal*, 2003, Vol. 41, No. 4, pp. 595-604.